Novel Designs of Metamaterials and Structures with Negative Poisson' Ratio and Negative Linear Compressibility

A thesis submitted in fulfilment of the requirements for the degree of Doctor of Philosophy

Arash Ghaedizadeh

B.Sc., M.Sc.

School of Engineering

College of Science Engineering and Health

RMIT University

March 2017

Declaration

I certify that except where due acknowledgement has been made, the work is that of the author alone; the work has not been submitted previously, in whole or in part, to qualify for any other academic award; the content of the thesis/project is the result of work which has been carried out since the official commencement date of the approved research program; any editorial work, paid or unpaid, carried out by a third party is acknowledged; and, ethics procedures and guidelines have been followed.

Arash Ghaediazadeh

March 2017

Acknowledgments

I would like to express my deepest appreciation to all those who have provided me with the possibility to complete this thesis. My special and sincere gratitude goes to my supervisor, Distinguished Professor Yi Min (Mike) Xie for his valuable suggestions, comments and contribution throughout this entire research process. I would also like to express my warm appreciation to my second supervisor, Dr. Jianhu Shen, for his encouragement, comments, contribution, and advice.

Additionally, I would like to acknowledge the support of the Australian Government's Cooperative Research Centres (CRC) Programme. This research was supported by the Wound Management Innovation CRC (project no. CRC2-16) and the Australian Research Council (project no. DP160101400).

This thesis is dedicated to:

My Mother with a strong and gentle soul who taught me to believe in hard work and that so much could be done with little.

The Memory of my Grandmother for being my first teacher.

My Father for earning an honest living for us and for supporting and encouraging me to believe in myself.

My Love, Bahar who has been my source of inspiration since we have been together.

Table of Contents

Abstract:

Materials and structures with auxetic and negative linear compressibility are of great potential to be used in many applications because of their uncommon mechanical deformation features. However, their design and manufacture are less studied as compared to their mechanical properties. The aim of this research is to explore several new approaches to the design and fabrication of cellular materials and structures with these two uncommon features.

Poisson's ratio and compressibility represent fundamental metrics to measure a material's distortion under directional loading and hydrostatic pressure. In contrast to the stiffness and strength of materials, which exhibit several orders of difference, Poisson's ratio varies in a very narrow range, i.e., from -1 to 0.5 for isotropic materials. For cellular materials, different values of Poisson's ratio are obtained by designing the shape and topology of their microstructures. When Poisson's ratio is negative, the corresponding material is called an auxetic material. When the performance of an auxetic material is dominated by its geometric features and deformation mechanisms of its microstructure and its Poisson's ratio is rare in nature, it is called an auxetic metamaterial. A similar concept applies to materials and structures with negative compressibility. To investigate the design and fabrication of these metamaterials, the research starts with identifying the geometric bounds for buckling-induced auxetic metamaterials as an extension to previous work. Then, a new design approach is developed for metallic auxetic metamaterials triggered by new findings relating to loss of buckling-induced auxetic behaviour for metallic based microstructures. Subsequently, two new methodologies are developed to design and fabricate negative linear compressibility composite (NLC) structures. All significant findings and the effectiveness of design and fabrication approaches are validated by experiments. Following an introduction in Chapter 1, the current literature on auxetic and NLC metamaterials is reviewed in Chapter 2.

In Chapter 3, development of auxetic metamaterial based on functionalization of base materials and topologies is described. In the first stage of this development, the geometric limits for buckling-induced auxetic metamaterials have been identified at both infinitesimal and finite strain. The previous investigation on buckling-induced auxetic metamaterial revealed that there is a geometric

limit for its microstructure to exhibit auxetic behaviour in infinitesimal deformation. However, the limit for auxetic metamaterials undergoing large deformation significantly was different from that under small deformation and has not been reported yet. Thus the geometric limit was investigated in an elastic and infinitesimal deformation range using linear buckling analysis. At finite deformation range, experimentally validated finite element models were used to identify the geometric limits for auxetic metamaterials. Depending on the controlling parameters of the topology, the bounds were represented by a line strip for one control parameter, an area for two control parameters and spatial domain surrounded by a 3D surface for three parameters. It was found that there was a significant difference in the geometric bounds at different deformation level. This difference was critical to design auxetic metamaterials for different applications and to control their auxetic performance. In the second stage of the development, the special features of metallic auxetic metamaterials were identified and investigated as the new class of auxetics. In contrast to the elastomer-based metamaterials, metallic ones possess new features as a result of the nonlinear deformation of their metallic microstructures under large deformation. The loss of auxetic behaviour in metallic metamaterials led us to carry out a numerical and experimental study to investigate the mechanism of the observed phenomenon. During this exploration, it was found that scaling the buckling modes and changing the plasticity of metallic base material can be used to tune the performance of auxetic metallic metamaterials undergoing large plastic deformation. The effectiveness of the developed tuning method was proved through both experiments and finite element simulations. By employing this tuning method, a 2D auxetic metamaterial was developed from a regular square lattice. By altering the initial geometry of microstructure with the desired buckling with a pattern scale factor (PSF) mode, the metallic metamaterial exhibited auxetic behaviour with tuneable mechanical properties. A systematic parametric study using the validated finite element models was conducted to reveal the novel features of metallic auxetic metamaterials undergoing large plastic deformation. An analytical model was derived to capture the variation of NPR with respect to strain, PSF, and plasticity of the base material. The results of this part of study provide a useful guideline for the design of 2D metallic auxetic metamaterials for various applications.

In Chapter 4, two new methodologies were developed to designing new NLC composite structures. Conventionally, materials and structures contract in all directions under a positive surrounded uniform pressure. However, some materials and structures exhibit an unusual behaviour under the application of pressure, resulting in an increase in dimension along one direction. This deformation feature is referred as the NLC. To reduce the manufacturing cost using 3D printing, a composite approach was proposed to manufacture these structures. Several new cellular composite structures with NLC composite structures were used as examples to demonstrate the effectiveness of the design approach. The test samples were manufactured using the traditional composite method with low cost. These investigations have clearly demonstrated the feasibility and effectiveness of designing and manufacturing of mechanical metamaterials using the presented approaches and laid the foundation for the expansion of their potential applications. The results of this research work were applied in filling materials for negative pressure wound therapy system. For some specific medical applications in wound management, the pore size of filling material was required to in the range of 200-500 micrometers. This pore size will facilitate the transmission liquids. By using our approach, the size of voids of new designed composite structures was determined by the cell size of the base material which was available and easy to manufacture such as conventional black foams in this study, while the NLC behaviour was dominated by the reinforcement component. The developed composite structures are under further assessment aiming to deploy the next generation of superior negative pressure wound therapy system for open abdomen wound closure. Finally, the conclusions of this thesis were summarized in chapter 5.

Publications list

The contents of this thesis have been presented through the following publications.

Journal papers

1- **Ghaedizadeh, A**., Shen, J., Ren, X. & Xie, Y.M. 2016. Tuning the performance of metallic auxetic metamaterials by using buckling and plasticity. *Materials*, *9*, 54. (JIF (2015): 2.728)

2- **Ghaedizadeh, A**., Shen, J., Ren, X. & Xie, Y.M. 2017. Designing composites with negative linear compressibility. *Materials and Design*. In press. (JIF (2015): 3.995)

3- Ren X., Shen J., **Ghaedizadeh A**., Tian H. & Xie Y.M. 2015. Experiments and parametric studies on 3D metallic auxetic metamaterials with tuneable mechanical properties. *Smart Material and Structures,* 24,095016. (JIF (2015): 2.769)

4- Ren X., Shen J., **Ghaedizadeh A**., Tian H. & Xie Y.M. 2016. Simple auxetic tubular structure with tuneable mechanical properties. *Smart Material and Structures*, 25, 065012. (JIF (2015): 2.769)

5- Xie Y.M., Yang X., Shen J., Yan X., **Ghaedizadeh A**., Rong J., Huang X. & Zhou S. 2014. Designing orthotropic materials for negative or zero compressibility. *International Journal of Solids and Structures,* 51, 4038-4051. (JIF (5 years): 2.56)

6- **Ghaedizadeh, A**., Shen, J., Ren, X. & Xie Y.M. 2016. Geometric bounds for buckling-induced auxetic metamaterials undergoing large deformation. *Applied Mechanics and Materials,* 846, 547-552.

7- Ren X., Shen J., **Ghaedizadeh A**., Tian H. & Xie Y.M. 2016. Numerical simulations of 3D metallic auxetic metamaterials in both compression and tension. *Applied Mechanics and Materials,* 846, 567-570.

Refereed conference papers

1- Ghaedizadeh, A., Shen, J., Ren, X. & Xie, Y.M. "Design and fabrication of materials and structures with negative Poisson's ratio and negative linear compressibility". *SPIE International Symposium on Smart Structures. March 25th to 29th 2017*, Portland, Oregon, USA. Forthcoming.

2- Xie Y.M.; Yang X.; Shen J.; Yan X.; Ghaedizadeh A.; Rong J.; Huang X. & Zhou S. "Designing orthotropic materials for negative or zero compressibility". 11th World Congress on Computational Mechanics (WCCM XI). July 20th to 25th 2014, Barcelona, Spain.

Patent

1- Shen, J., Ghaedizadeh, A. & Xie, Y.M. (Filing date 12 October 2015). Wound filler for negative pressure wound therapy provisional patent application. No. 2015904144.

Chapter 1

Introduction

Background

The main aim of structural engineering is to design, develop and evaluate the strength and rigidity of systems that can satisfy the design criteria for different applications. Designing high-performance novel materials and composites is one of the most important concerns of structural engineering. Such products are ideal for wide applications ranging from energy-absorbing devices to advanced medical imaging and therapeutics. Many engineering disciplines are involved in optimisation or applying creativity to manipulation of materials. Their main aim is applying mathematical and scientific ideas to achieve desired products and satisfy the design performance objectives. This objective can be achieved by designing the best topology for an engineering system to exhibit tuneable exceptional uncommon properties when the system is subjected to disturbances of external factors such as changes in temperature or applied strain. When these properties are superior to these found in nature, the artificial material is termed as a metamaterial. The word of “meta” originated from a Greek word, and the literal meaning of this word is “beyond” [1].

The term of “metamaterial” was made first time by Rodger Walser, and it was originally defined as “Macroscopic composites having a synthetic, three-dimensional, periodic cellular architecture designed to produce an optimised combination, not available in nature of two or more responses to specific excitation”[2]. Also, another definition was given by these references [3-7] as “the principle of metamaterials refers to the design of composites and materials which gain their uncommon and unique properties from geometrical configurations rather than chemical composition.” These definitions present the certain features of metamaterials but not all. Ti Jun Cui [8] gave a different definition as “ metamaterials is a macroscopic composite of periodic or non-periodic structure, whose function is due to both the cellular architecture and chemical compositions.”

Metamaterials are having a major impact in different fields such as mechanical, thermal, electrical and optical. It should be noted that in the fields of mechanics and photonics, metamaterials have led to a changing several conventionally accepted bounds on material behaviours such as Poisson’ ratio (PR) and bulk modulus for mechanical metamaterials and permittivity and permeability for optical metamaterials.

The artificial optical metamaterials have attracted the greatest deal of attention among other types of metamaterials due to their unusual properties such as negative refraction, optical lensing below and invisibility cloaking. Optical metamaterials permit to control the magnetic and electric of light through tuning the positive or negative value of two important factors of permittivity and permeability. The best example for this class of material is the left-handed material (LHM), that firstly was reported in the seminal research by Veselagom [9]. LHM has two important properties which are negative permittivity and permeability simultaneously. These important properties cause propagating of electromagnetic waves with the wave vector opposite to the Poynting vector[10]. LHM leads to some important phenomena, such as negative refraction, reversed doppler shift [9] and a perfect lens [11], etc.

Electromagnetic and Optical metamaterials have been studied intensively, and it has been a most interesting topic for researchers active in the field of metamaterials studies. However, mechanical metamaterials are less studied. This is despite the fact that mechanical materials have the useful

applications in engineering due to their unprecedented physical properties [12]. The behaviour of mechanical metamaterials was normally explained in terms of the intricate interplay between their microstructures and their deformation mechanisms. The dependence of properties of mechanical metamaterials on cellular configuration leads to the excellent capability to tunning of metamaterials. This feature gives the possibility of designing the properties of a material from smallest building block (microstructure) which is much smaller than the wavelength of the acoustic or optical waves they are interacting with [12]. Then by patterning the new design building block the possibility of giving a particular shape or form to new designed properties is almost endless. Therefore new mechanical materials and structures with great properties that are not available in nature can be produced, and it is the biggest advantage of mechanical metamaterial [12]. Accordingly, the interest of worldwide researchers has been concentrated on mechanical metamaterials and continues to grow.

The complexity of geometry of microstructure of mechanical metamaterials is infinite, but all these simple or complex periodic designs lead to materials with uncommon homogeneous properties. In other words, the most important design aim of mechanical metamaterials is the realization of properties that cannot be observed in traditional materials. In the meantime, it is possible to reconfigure the initial design of microstructure through changing the size, shape and void area of the microstructure to provide a tuneable performance which is coupled with the geometrical configuration of the microstructure. This possibility leads to providing an effective control method to tune the mechanical properties of the mechanical metamaterial during the designing process. The tuneable performance is a special feature for mechanical metamaterials and potentially could be implemented in the particular novel engineering applications across a wide range of length scales with specific uncommon properties.

These uncommon properties are categorised into negative response parameters [3-37], multistability [32, 38, 39] or programmability [40]. One important example for the metamaterials with negative response parameters is mechanical materials and structures with uncommon behaviours such as NPR [3, 5, 7, 13, 20, 21, 23-27, 29, 33-37], negative stiffness[41], negative compressibility[14, 15, 22, 28, 32, 42, 43], negative specific heat and negative thermal expansion[30, 44, 45].

The focus of this study is on metamaterials and structures with NPR and negative compressibility. About the class of materials and structures with NPR property, it should be noted that the majorities of materials have a positive PR that is about 0.5 for rubber and 0.3 for glass and steel [29]. The majorities of materials have a positive PR that is about 0.5 for rubber and 0.3 for glass and steel [29]. In contrast to the stiffness and strength of materials, PR varies in a very narrow range. The thermodynamic requirement in the theory of elasticity for a conservative system demonstrates that for homogeneous isotropic materials, the theoretical bound of PR is from -1 to 0.5. Therefore, the existence of materials with NPR has long been accepted, and they are known as "auxetic" materials [46].

The deformation feature of auxetic materials can be described as an anomalous behaviour that indicates that materials expand (contract) in a transverse direction when uni-axially stretched (compressed) [5, 18, 27, 29]. Over the past decades, continuous efforts were put in towards the development of auxetic metamaterials because of their unconventional behaviour under uniaxial loading. Their unique properties opened a window towards a wide range of applications such as the design of novel fasteners [47], biomedical applications [48], energy-absorbing devices [49], acoustic dampers [50], membrane filters with variable permeability [51], and the design of composites [52].

About materials and structures with negative compressibility it should be noted that compressibility is a measurement to evaluate the deformation feature of a solid or fluid under the applied pressure. Conventionally, materials and structures contract in all directions under a positive surrounded uniform pressure. This behaviour is defined as the positive compressibility (PC) along three main axes. However, some materials and structures exhibit an unusual behaviour under the application of pressure, resulting in an increase in dimension along one or two directions. This deformation feature is referred to as the negative linear compressibility (NLC) or negative area compressibility (NAC). The negative volume compressibility (NVC) behaviour is forbidden in classical thermodynamics [14] but it is possible in a pressure–induced phase transition [53]. Baughman et al. [14] explained a variety of potential applications of the NLC phenomenon such as the development of optical

telecommunication systems, artificial muscles [54], infiltrated porous structures and a new generation of pressure sensitive sensors and actuators [14, 15, 55].

1.2. Problem description and objectives

As discussed earlier, the performance development of mechanical metamaterials through designing new configurations for microstructures will lead to materials and structures with uncommon behaviours such as NPR, negative compressibility. The increasing rate of demand for new materials and structures with functional features leads to more efforts in order to development of more designs with better performance for different applications. In the case of periodic cellular metamaterials and structure, this objective can be achieved by employment of novelty in creative ways to design new microstructures.

This study has extended the application of creativity and experience to design two different classes of metamaterials and structures with NPR behaviour and NLC phenomenon respectively.

The auxetic metamaterial is a typical class of metamaterials and is designed rationally based on experience[56]. The earliest significant work on synthetic NPR cellular materials was led by Gibson and Ashby who presented a macroscopic auxetic cellular structures with 2D re-entrant honeycombs cells [57]. Then an artificially designed auxetic foam with a re-entrant cell was reported in the seminal research of Lakes in 1987 [29]. Following that, the interest of researchers was concentrated on periodic 2D auxetic materials through modifying the geometry of microstructures. These consist of composites with star-shaped inclusions [36], a structure formed from lozenge grids [62], a formed structure from square grids [63], a square lattice of circular holes [5], and many other 2D topological patterns. Much of the subsequent work on auxetic materials was focused on periodic 2D geometries. It was found that key features of NPR materials included chirality in microstructures and rotation of rigid units [64]. For 3D cellular materials with periodic microstructures, analytical studies were conducted on auxetic materials consisting of networks of beams[65] multi-pods [66] and rigid units [67]. Due to the limitation of fabrication techniques, very few designs of such 3D auxetic materials have been realised.

Basically, using the elastic instability will take advantage of the nonlinearly to raise the applications of buckling induced metamaterials with specific properties such as auxetic behaviour, negative compressibility and tuneable acoustic and optical reflectivity [58]. Previous results on deformation pattern of buckling-induced auxetic metamaterials under compression showed that the NPR behaviour originated from the localisation of buckling mode which triggered a global change in the deformation pattern [4]. The buckling in walls of unit building cell led to an alternate rotation of rigid parts and suddenly produced a square of ellipses with horizontal and vertical parallel axes [59]. The relation between the architecture of microstructure and the nonlinear stress-strain behaviour of cellular metamaterials has been an open research area for many researchers [3, 7, 58, 59]. Also, it has been concluded that the size, arrangement and the shape of void parts had a significant effect on stability and global response of buckling-induced cellular metamaterials [5, 7, 59]. There was a geometric limit for the microstructure of auxetic metamaterials in the elastic and infinitesimal deformation range. Recently the effect of void shapes on nonlinear response of a planner metamaterial was investigated by Bertoldi et al. [59]. More recently a geometrical controllable parameter was defined for a simple 3D auxetic metamaterial to control the volume fraction by Shen et al. [7] and through the bulking analysis, a line strip for this controllable parameter was defined to exhibit auxetic behaviour in infinitesimal deformation.

The aim of the first part of this study was to develop a new method to find a geometric bound for buckling-induced auxetic metamaterials undergoing large deformation. The geometric limit was investigated in an infinitesimal deformation through buckling analysis and in large deformation range through post-buckling analysis with an explicit algorithm. From a practical view, an effective strain range of NPR behaviour was adopted using an energy efficiency method. This new criterion for auxetic behaviour changed the geometric bounds of auxetic metamaterials.

It is worth noting that, most of 2D and 3D auxetic metamaterials invented are relatively soft and deform in the elastic range of the base material and the deformation is reversible and repeatable. However, the weak stiffness and strength and the low softening temperature of these elastomeric metamaterials prevented them from many applications such as automotive, aerospace, civil

infrastructure, defense-related materials and structures requiring high stress and high temperature. In contrast to elastomers, metals have higher stiffness, strength, density and melting point. Copper, gold, platinum, silver, and brass are especially ductile and might be suitable for fabricating novel auxetic metamaterials. According to a recent review of auxetic materials and structures [6], those applications have a large potential market. Therefore there is an urgent need to find ways to design and fabricate metallic auxetic metamaterials.

The next part of this study focused on the development of an approach to design auxetic metallic metamaterials. Only a few researchers studied the NPR performance of metallic auxetic metamaterials undergoing large plastic deformation. Therefore the knowledge on the deformation features and auxetic performance of metallic metamaterials is very limited. The first work in this area was done by Friis et al. [60], who proposed a polymeric and metallic foam with auxetic behaviour. Recently, a 2D metallic auxetic periodic structure with low porosity was reported by Taylor et al. [61]. Another research in this area was carried out by Dirrenberger et al. [62] on the auxetic behaviour of the metamaterial undergoing plastic deformation. Moreover, the effect of plasticity on auxetic behaviour was assessed using an anisotropic compressible plasticity framework as a macroscopic model by Andersson et al. [63].

Inspired by previous works on buckling-induced auxetic elastic and elastoplastic metamaterials, we expanded the similar design approach to metallic structures. However, the buckling-induced geometrical design lost its auxetic behaviour under large plastic deformation when the base material was changed to metals. Therefore, the specific aim of this research is to develop a general approach to designing and tuning the metallic metamaterials with auxetic performance undergoing large plastic deformation. The auxetic performance of metamaterials on any length of scale is dependent on the geometrical features and deformation mechanisms of their microstructures. Hence, the general approach of the metamaterial starts at the microstructure level by employing an existing deformation mechanism that leads to auxetic behaviour [5, 7]. In this approach, the geometry of microstructure of a regular structure is modified then it is altered by the desired buckling modes.

As mentioned before the auxetic behaviour is described only in terms of their geometry and deformation mechanism. It is found that there is a direct relation between relevant microstructural features and NPR behaviour of materials. Therefore, most of the researches in the auxetic area explored new geometrical configuration which led to auxetic behaviour [64]. The auxetic systems *(reviewed before)* exhibited auxetic behaviour at different length scalesfrom macro- to micro- and even down to nanostructures. These systems consist of different particular geometric configurations, and they deform through different deformation mechanisms.

Various mechanism and analytical models were developed to predict auxetic behaviour. Most of these analytical models were two-dimensional, and they were developed to describe the auxetic behaviour of a cross section of materials. The earliest analytical model was a 2D re-entrant hexagonal honeycomb model which deform through rotating of hexagonal at hinge joints or flexing at verge and it was used to describe the auxetic behaviour in foams [29, 65] and nanostructured networked polymers [46]. During the last decade several new 2D analytical models were developed by Grima et al. to describe the auxetic behaviour in foams [66], hypothetical nanostructured networked polymers [67], zeolites [68] and silicates [69]. The performance of these analytical models was defined through rotation of different polygon shapes. The first and most simple analytical model from this category is auxetic behaviour from rotating squares [24] which was defined based on an arrangement involving rigid squares connected together at their vertices by hinges. The other similar analytical models from this category are: auxetic behaviour from rotating rectangular rigid units [21], Auxetic behaviour from rotating triangles[70] and auxetic properties of rotating rhombi and parallelograms [25].

The defined models based on rotating of rigid polygons are extremely useful to characterise the mechanism behind the auxetic behaviour however the behaviour of real materials are much more complex than the idealised mechanisms guided by these geometrical models. For example, the PR's value predicted from an analytical model of rotating rigid squares [24] was equal to -1 which was independent of the applied strain and the direction of loading. Compared with values from experiments of similar design, it was overestimated and the PR's value was dependent on the applied strain and the direction of loading. Several attempts were carried out to further development of the

analytical models and to offer new deformation mechanisms which are more similar to the real behaviour of the auxetic materials. It was found that the auxetic behaviour was dependent on two factors simultaneously. The first factor was the amount of rotation of polygons and the second factor was the extention of deformation of polygons [71, 72]. For this purpose three developed analytical models were proposed by Grima et al. [73-75] as 'auxetic behaviour from rotating semi-rigid units'[73], 'auxetic behaviour from stretching connected squares'[75] and 'auxetic behaviour from rotating stretching squares'[74] to describe the predicted auxetic behaviour of materials under applied strain. The most important improvement was that these two new analytical models were the extension of 'rotating rigid squares 'analytical model so that the rigid square units could deform apart from rotating relative to each other. This improvement led to improved accuracy in prediction of auxetic behaviours of materials.

It should be noted that all of these analytical models only predicted the auxeticity of relatively soft materials and structures in the elastic range of the base material in which the deformation was reversible and repeatable. However, when the deformation entered the plastic range for metallic structures and materials, several new features may emerge, which may not exist in the elastic deformation range such as permanent deformation and strain hardening.

In order to investigate the possibility of deriving an analytical model for predicting the behaviour of auxetic metallic materials, several assumptions were added to measure the plastic deformation of square units and plastic moments at hinge joints. Therefore in this study, a new analytical model was explored where the 'plastic deformation mechanism of squares' and the 'rotating squares deformation mechanism' occurred simultaneously.

The last part of this study focused on designing composites with NLC. NLC behaviour was firstly observed in tellurium along a particular direction, and it was reported by Bridgman in 1922 [76]. Baughman et al. [14] explained a variety of potential applications of the NLC phenomenon such as the development of optical telecommunication systems, artificial muscles [54], infiltrated porous structures and a new generation of pressure sensitive sensors and actuators [14, 15, 55]. The NLC behaviour was discovered at the molecular level such as LaNbO4 [77], Ag3[Co(CN)6] [19], KMn3

[Ag(CN)2]3 [15, 78] and a large giant NLC in the molecular framework of Zn[Au(CN)2]2 [15]. At micro and macro level, the NLC behaviour arose from the operation of hinged joints or bending at nodes of frameworks. It included the materials with the structures of wine-rack, honeycomb, hexagonal, rhombic and other related geometries that deformed like the wine-rack mechanism [22, 23, 65]. There has been extensive work on materials and structures design using the composite techniques, covering various uncommon properties such as auxetic [79-84], negative stiffness [31, 85] and negative thermal expansion inclusions[44, 45]. The basic idea of the composite technique is to improve the properties of materials and structures through adding a second phase to them in the form of fibre element or particulates. In this study, we developed the simple design approaches to manufacturing a new series of structures with NLC property based on the application of composite techniques. The new design approaches were proposed to design two types of NLC composite structures, namely, composites with a continuous hinged network and composite structures with discrete truss elements based on the specially ordered patterns. The NLC property of the composite structures was investigated experimentally using a small but sufficient number of bulk specimens. For some specific medical applications such as wound management, specific products with NLC behaviour are required for a wound filler structure. The open abdomen (OA) may bring some serious challenges for surgeons and nurses for treating severe patients. Currently, there are many methods and products to facilitate OA management. However, the commercial acceptance and wound preservation are not applicable. Also, they may cause penetration or breaks of the skin. The newly emerged commercial method is the negative pressure wound therapy (NPWT) system, which has been designed for temporary closure of the wound and re-entering the abdomen. The other design requirements are providing a separate surface between wound and external region, sucking out infective fluid and material from the wound when applying sufficient pressure, reducing the swelling size and removing exudates. The main aim in the last part of this study was to improve the NPWT by using newly designed foams which can be used inside the cavity and directly close the wound under negative pressure without using any mechanical device. The deformation pattern of newly designed

composites under vacuum pressure leads to achieve temporary closure of the abdomen when the primary closure of the wound is not possible.

In summary, the objectives of this research project are:

- Development of a method to find the geometric bounds for buckling-induced auxetic metamaterials undergoing large deformation.
- Development of a general approach to design auxetic metallic metamaterials which exhibits auxetic behaviour with almost constant negative values of PR over a large strain range.
- Development of a systematic parametric study using the validated finite element models to reveal the novel features of metallic auxetic metamaterials undergoing large plastic deformation.
- Development of an analytical model for predicting the behaviour of auxetic metallic materials.
- Development of design approaches to design two types of NLC composite structures, namely, composites with a continuous hinged network and composite structures with discrete truss elements based on the specially ordered patterns.
- Application of NLC composites as a filling material for the negative pressure wound therapy system to achieve temporary closure of the abdomen when the primary closure of the wound is not possible.

1.3. Significance

The significance of this research is that the results of this study bring together in one accessible volume, several design approaches that are useful for designing a new class of metamaterials and structures with the two different uncommon behaviours of NLC and NPR.

The research project made a significant step forward from the existing works on buckling-induced elastic auxetic metamaterials by proposing a general approach to design of metallic auxetic metamaterials undergoing large plastic deformation. For metallic structures and materials undergoing large deformation, the elastic deformation only occurred initially in a very small strain range, i.e.

0.1%-0.5% for the solid metal as could be easily estimated by the ratio of the yield stress over Young's modulus. For metallic auxetic metamaterials, the effective strain range for having auxetic behaviour could be several orders larger than the elastic strain range. When the deformation entered the plastic range for metallic structures and materials, several new features emerged, which did not exist in the elastic deformation range. These included localisation of plastic strain, permanent deformation, strain hardening, loading path dependence, and effect of anisotropic plastic flow. These features offered myriad opportunities for designing novel metamaterials. The research project filled a gap in this area. More importantly, a new category of 2D metallic auxetic metamaterials over a large strain range was obtained. The new metallic metamaterial exhibited auxetic behaviour with almost constant negative values of PR over a large strain range. This feature was very useful for practical applications in macroscopic metamaterials as well as in nanoscale structures. A set of parametric studies using validated finite element (FE) simulation has been done to show the possibility of providing an effective control method to tune the mechanical properties of the 2D metallic auxetic metamaterial during the designing process.Also, the results of this research project extended the application of the composite technique to design a new series of campsites with NLC behaviour for some application with specific requirements. It should be noted that for some specific medical applications such as wound management, specific products with NLC behaviour are required for a wound filler structure. To transmit the liquids during curing, the void size of the filler structure should be in a specific range, i.e. 200-500 micrometers. Due to the manufacturing capacity, it was very difficult to produce a large quantity of NLC materials in meters with such small dimension in its microstructures. A combination of the foam-type material as the filler component and the reinforcement network with NLC behaviour provided a practical solution. In such case, the size of voids of new composite structures was determined by the cell size of the filler material. The reinforcement component played a dominant role in the NLC behaviour of the composite structure.

1.4. Organization of the thesis

This study dealt with the topology design of microstructures for materials and composites with properties of NPR and NLC. In the second chapter, a literature review on various topology designs of

materials and structure with these two uncommon behaviours is presented. Most relevant material designing methods are also briefly introduced. A brief summary of recent researches on the applications of NPWT system is also provided in Chapter 2 for specific medical applications such as wound management. Chapter 3 reports the results of new geometric bounds, design approaches and analytical models for auxetic metallic metamaterials undergoing large deformation. Chapter 4 focuses on the design of NLC composite structures with continuous and discontinuous embedded networks using modified composite technique as an innovative way to reduce manufacture cost. The application of NLC composites with appropriate stiffness and deformation feature for NPWT system is also described as a new invention named “smart foam” in Chapter 4. Chapter 5 summarizes most important results and conclusions from the present research project.

Chapter 2

Literature review

This thesis was dedicated to the extension of the design concept of metamaterials and structures with NPR and NLC properties based on functionalization of base materials and topologies. The first section of this chapter dealt with a critical review of the structural topology designs that have so far been applied to produce the microstructures of auxetic cellular materials and structures (CMS) with desired functional property of NPR. A description of the analytical models was summarized as a basis to predict the auxeticity properties of the cellular materials. Section two of this chapter provided a brief review of the development of designing the metallic auxetic metamaterials. In the next section, the development of designing approaches for some structures and materials with NLC behaviour was presented which was followed by a brief introduction to the applications of NPWT system for wound management. It should be noted that the auxetic materials and structures were classified to naturally occurring and artificial ones [47, 48]. Also artificial auxetics were classified to auxetic soft cellular

materials and structures (SCMS), metallic auxetics, composite auxetics and multi-material auxetics. The first scope of this research was limited to two classes of auxetic SCMS and metallic auxetics.

2.1. Auxetic materials and structures

Many cellular structures and materials were designed to have exceptional properties. When these properties were superior to these found in nature, the artificial cellular material was termed as a metamaterial. The class of CMS included a wide range of various materials and structures with different geometric configurations such foams, honeycombs, structures with different geometries of interconnected unit building cell such as fibres, hollow spheres, or rods [86]. The microstructure of CMS consisted of two different separate parts including a continuous solid part which was called matrix [87], and the next part was continuous or discontinuous gaseous part. CMS were classified into different classifications according to their various features in different kinds of literature. As noted before, the mechanical properties of CMS could be adjusted by the compositions or topology of the microstructure. In other words the properties of CMS were affected by "imperfections" of the critical features of microstructures. These features were determinative for designing the topology of a microstructure such as the size and size distribution of the microstructure, the connection link between the cells due to voids and windows, the total porosity (void volume fraction) and the density of the material [88]. Also, they could be considered as ‘‘environmentally friendly products’’ because lass amount of raw materials was used to produce them. The concept of porosity caused that the CMS become lighter than bulk materials and this very simple feature led to costs savings. The term of void volume fraction was often used to define the amount of solid material or void part with respect the 100% dense solid and it was ranged from 0.9 down to 0.02 [88]. In general, designing CMS was an alternative to product a classification of new unique properties (that solids did not have them) such as low thermal transport properties, high energy absorption capability, easy-tuneable acoustic absorption properties and NPR, etc.

An overview on mechanical metamaterials with auxetic behaviour was presented by Christensen et al. [89] in the Milton–Ashby map that was presented in Figure 2-1 (bulk modulus (B), shear modulus (G) vs. mass density (r)). The black ellipses presented the area (space) that was occupied by

usual solids, and the red space presented the area that was occupied by auxetic CMS. A way to extend the range of auxetic metamaterials with different properties or to fill the vacant parts between occupied spaces, is designing light–weight metamaterials. This aim can be achieved through introducing void parts with different shapes and volume fraction percentages in solid materials or designing auxetic CMS.

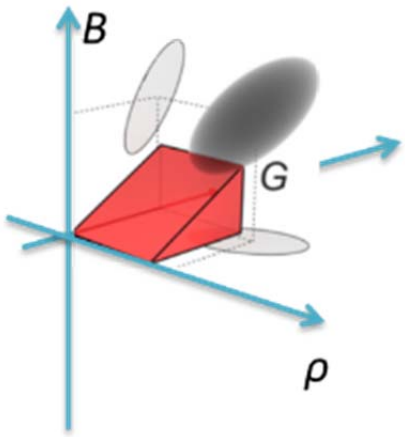

Figure 2-1: Milton–Ashby map for auxetic materials [89].

As mentioned before the auxeticity was observed in three different scales of micro, macro and nano scales of 2D and 3D CMS. The auxetic CMS were classified into three different classes according to the geometrical configuration of microstructure as following: 1) re-entrant class; 2) chiral class; and 3) rotating units class [90].

2.1.1 Re-entrant class

The earliest work in the class of re-entrant CMS was done in 1982 by Gibson et al. [57] through investigation the mechanical properties of a 2D cellular honeycomb. Several beams models were used to predict the bending, elastic buckling and the plastic collapse of unit cell walls. This work was extended by Master and Evans [91, 92]. The honeycomb core materials with regular hexagonal cell shape microstructure have a great range of application. However, the highly in-plane positive PR of the honeycomb structure with hexagonal cell shape led to bending (out-of-plane deformation) and produce an anticlastic or saddle-shaped curvature. This mechanical deformation was changed by altering the geometric configuration of microstructure as shown in Figure 2-2 which led to the

negative value of PR. When the new structure with altered microstructure was stretched in the horizontal direction, the cell size of the honeycomb structure was enlarged in the vertical direction.

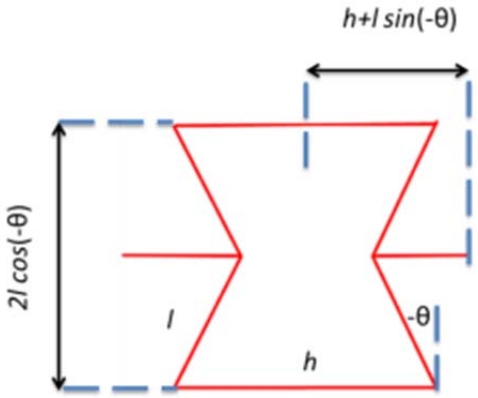

Figure 2-2 Re-entrant microstructure of conventional hexagonal auxetic structure of Evans [91].

An analytical investigation was conducted by Smith et al. [93] to find the following formula which gives the PR's value and modulus of elasticity in the direction of loading:

$$\vartheta_{1,2} = \frac{\sin\theta(^{h}/_{l}+\sin\theta)}{cos^{2}\theta} \quad (2\text{-}1)$$

$$E_1 = K\frac{(h/l+sin\,\theta)}{b\,cos^{3}\theta} \quad (2\text{-}2)$$

$$K = E_s b\left(\frac{t}{l}\right)^3 \quad (2\text{-}3)$$

Where ***h*** presents the half of the length of horizontal rib, ***l*** presents the length of disposed ribs, ***b*** is the depth of ribs into the plane of paper, ***t*** is the thickness of ribs, ***θ*** is the angle between disposed ribs and perpendicular line and $\boldsymbol{E_s}$ is Young's modulus of base material [95].

For the first time, the topology optimisation was used by U.D. Larsen et al. [94, 95] to design compliant mechanisms and material microstructure with NPR behaviour. This procedure lets the user characterise the elastic properties of materials or the mechanical or geometrical advantages of compliant mechanisms and returns the optimal structures [95].

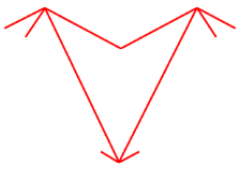

Figure 2-3 Re-entrant triangular microstructure from numerical topology optimisation [95].

The triangular geometry of microstructure was shown in Figure 2-3 and it is noted that the NPR behaviour was depended mainly on the geometry of microstructure such as length of the ribs and angle between the ribs for this specific geometry [90].

Several 2D periodic structures presented by Grima et al. [26] which were called “connected stars” and contained star-shaped microstructure of different rotational symmetry which was patterned to form 2D Re-entrant structures as shown in Figure 2-4. Under stretching, the star-shaped microstructure was opened up and flattened and this simple mechanism led to auxetic behaviour. Therefore the auxetic behaviour depended mainly on the rational stiffness of joints of the star-shaped microstructure or in other words the hinging spring constants of the adjacent connections. According to the geometry of star-shaped microstructures, under stretching the microstructure of order 4 and 6 could be opened up and have the greater auxetic behaviour compared to order 3.

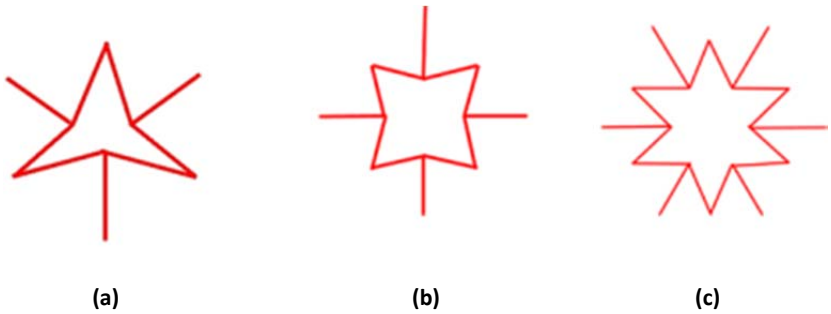

Figure 2-4 Re-entrant auxetic 2D star-shaped cellular microstructure; (a) Rotational symmetry of order 3; (b) Rotational symmetry of order 4; (c) Rotational symmetry of order 6 [26].

Recently, several 3D re-entrant auxetic CMS were presented which the mechanism of auxeticity was similar to 2D re-entrant structures [96-98]. The first 3D re-entrant auxetic metamaterial with pyramid-shaped microstructure was presented by Zheng-Dong Ma [96] which was a 3D version of 2D re-entrant structure with triangular microstructure [95] as shown in Figure 2-5a. Also, the microstructure of two new 3D re-entrant auxetic metamaterials were formed through rotating the microstructure of 2D conventional hexagonal auxetic structure by Evans [91]. Shokri rad et al. [98] rotated the 2D microstructure 90° about X axis and Hengsbach et al.[97] rotated the 2D microstructure 90° about the Y axis to form different buck auxetic materials as shown in Figures 2-5b and 2-5c.

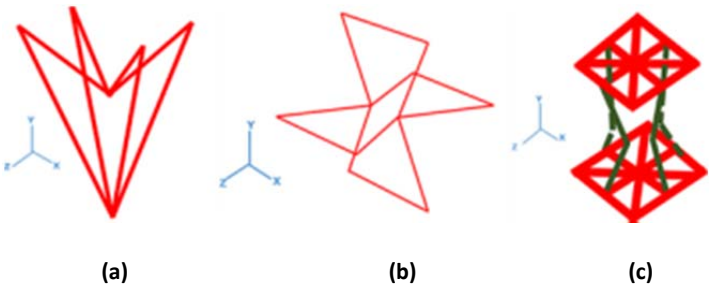

Figure 2-5 Re-entrant auxetic 3D cellular metamaterials; (a) three-dimensional auxetic structures with pyramid shaped microstructure; (b) three-dimensional auxetic structures with oration of 2D triangular microstructure about X axis (c) three-dimensional auxetic structures with oration of 2D triangular microstructure about Y axis.

2.1.2 Chiral Class

The second class of auxetic soft CMS was called with the term of 'Chiral' which indicated asymmetric in such a way that the structure and its mirror image were not superimposable. The chiral network structures consisted of some ligaments which were connected to rigid annular units. Under applied strain, the rotation of rigid annular units led to winding or unwinding of the ligaments on rigid units and exhibiting auxetic behaviour [99].

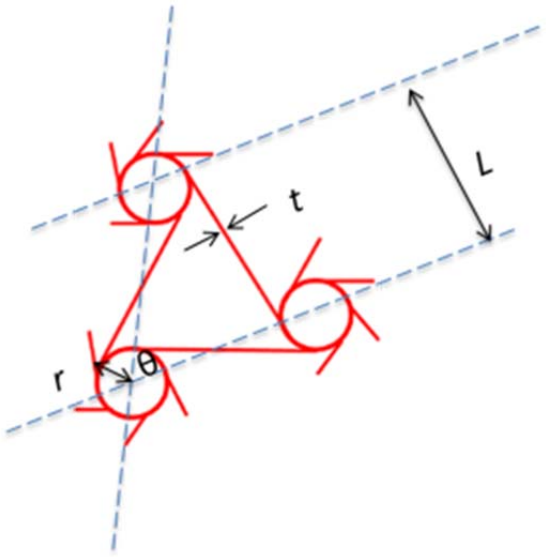

Figure 2-6 Geometrical configuration of auxetic chiral microstructure [71].

In this class, firstly a 2D chiral honeycomb was presented by Prall et al. [73] as shown in Figure 2-6 where six ligaments were attached tangentially to each rigid ring. Under applied strain, the auxetic chiral microstructure exhibited a plateau value of PR of -1 with capable of retaining the auxetic behaviour at large-strain in contrast to other known auxetic materials with a strain-dependent value of

PR. Also, the analytical investigation revealed that the modulus of elasticity of this chiral network was equal in different directions and is given as follow:

$$E = E_s.\sqrt{3}\frac{t^3.L^3}{L^3.r^2} \quad (2\text{-}4)$$

Where ***Es*** is the modulus of elasticity of the base material; ***t*** is the thickness of ligaments and ***L*** is centre to centre distance between rigid rings and ***r*** is the radius of rigid rings.

Another Chiral network lattice was presented by Justin Dirrenberger et al. as shown in Figure 2-7 [100]. The radius of circular or elliptical ligaments of the microstructure is the main paramter to tune the PR value. The most important application of newly auxetic chiral network is for bio-inspired composite networks.

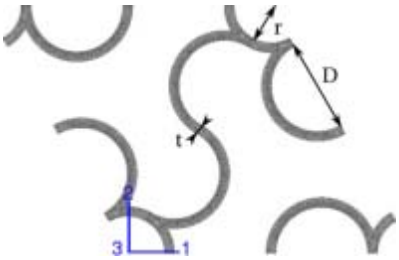

Figure 2-7 Geometrical configuration of auxetic chiral microstructure [100].

Recently, a new auxetic 3D chiral lattice structure with rigid cubical nodule and multiple deformable ribs was presented by Chan Soo Ha et al. [101] as shown in Figure 2-8. The PR of 3D chiral lattices could be tuned from positive to negative values by increasing the number of cells. This phenomenon cannot be observed in a classical elastic continuum but it can occur in a Cosserat solid.

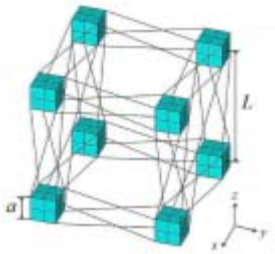

Figure 2-8 Auxetic 3D chiral lattice structure with rigid cubical nodule and multiple deformable ribs [101].

2.1.3 Rotating Polygons Class

It is worth noting that the researches in the area of 'Rotating Polygons Class' mainly focused on two following main topics: 1-development analytical models to predict the NPR behaviour of auxetic

CMS, 2- designing new 2D and 3D auxetic CMS with various microstructure configurations and base materials. Various mechanism and analytical models were developed to predict auxetic behaviour. Most of these analytical models were two-dimensional, and they were developed to describe the auxetic behaviour of a cross section of materials.

2.1.3.1 Analytical models to predict the NPR behaviour of auxetic CMS

The mechanism of the auxetic behaviour of the auxetic CMS originated from the rotation of polygons at their vertices by hinges [21, 24]. For the first time, a 2D analytical model was proposed by Grima et al. [24] to predict the auxetic behaviour of different auxetic materials such as inorganic crystalline materials [64]. This mechanism may be regarded as a 2D assembly of squares or a 3D assembly of cubes in different auxetic CMS.

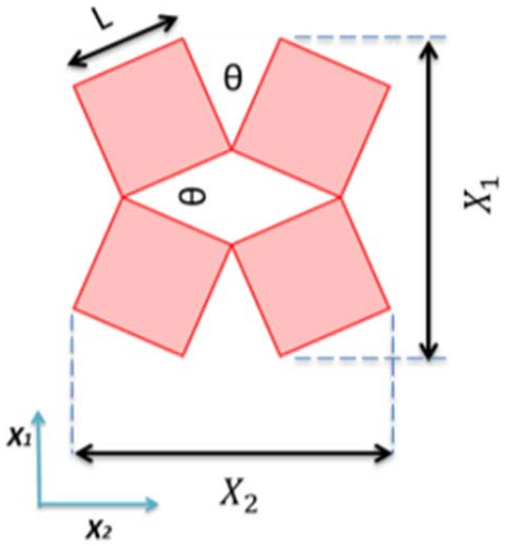

Figure 2-9 RVE of the analytical model of "rotating rigid squares."

As shown in Figure 2-9, the length of the rigid square unit was defined with the letter of ***L***, where **θ** is the acute angle between two rigid units. Therefore, at each specific level of applied strain, the value of PR is changed and it was determined as strain-dependent value. Equation 2-5 was derived to measure the dimensions of the unit cell in the X_1 and X_2 directions. It was assumed that square units were not deformable and the second assumption was that the stiffness of this arrangement only came from the rotational stiffness of the hinges K_h.

$$X_1 = X_2 = 2l[cos\ (\frac{\theta}{2}) + \sin(\frac{\theta}{2})] \quad (2\text{-}5)$$

The strain-dependent value of PR given as follow:

$$\vartheta_{ij} = -\frac{d\varepsilon_j}{d\varepsilon_i} \quad \text{Where i and j = 1, 2} \tag{2-6}$$

$$d\varepsilon_i = \frac{1}{X_i}\frac{dX_i}{d\theta}d\theta, \quad \text{i} = 1,2 \tag{2-7}$$

Where:

$$\frac{dX_i}{d\theta} = l\left[\sin\left(\frac{\theta}{2}\right) - \cos\left(\frac{\theta}{2}\right)\right], \quad \text{i} = 1,2 \tag{2-8}$$

Hence from the above Equations, it was found that PR's functions could be simplified as follows:

$$\vartheta_{12} = \vartheta_{12} = -1 \tag{2-9}$$

Also from the principle of energy approach, the Equation 2-10 was derived to represent Young's modulus of the structure ***Ei***.

$$E_1 = E_2 = K_h \frac{8}{l^2}\frac{1}{[1-\sin(\theta)]} \tag{2-10}$$

The compliance matrix of the structure was derived as follow:

$$S = \begin{pmatrix} S_{11} & S_{12} & 0 \\ S_{21} & S_{22} & 0 \\ 0 & 0 & 0 \end{pmatrix} = \begin{pmatrix} \frac{1}{E_1} & \frac{-\vartheta_{21}}{E_2} & 0 \\ \frac{-\vartheta_{12}}{E_1} & \frac{1}{E_2} & 0 \\ 0 & 0 & 0 \end{pmatrix} \tag{2-11}$$

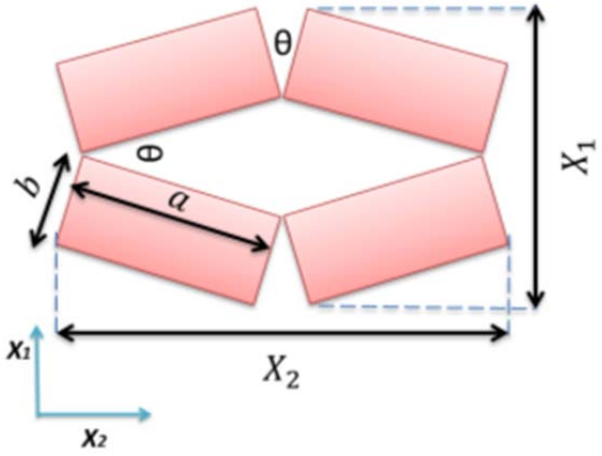

Figure2- 10 RVE of the analytical model of "rotating rigid rectangles."

The analytical model with rigid square units [24] was extended by Grima et al. [102] to propose a new analytical model which was named as "NPR from rotating rectangles." The shape of rotational units in the new extended model was a rectangle as shown in Figure 2-10. The on-axis PR was given

by Equation 2-12, Young's modulus was given by Equation 2-13 and the compliance matrix of the structure was similar to the previous model with square rigid units.

$$\vartheta_{12} = \vartheta_{12} = -1 \quad (2\text{-}12)$$

$$E_1 = E_2 = K_h \frac{8}{a^2} \frac{1}{[1-\sin(\theta)]} \quad (2\text{-}13)$$

Furthermore, another analytical model with the assumption of the rigidity of rotational units was proposed by Grima et al. [20] and the shape of rigid units was a triangle. Figure 2-11 shows the parallelogram unit cell of the analytical model of "rotating rigid triangles."

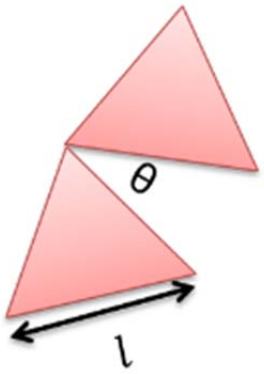

Figure 2-11 The parallelogram unit cell of the analytical model of "rotating rigid triangles."

The on-axis PR was given by Equation 2-14 which shows that the PR's value constantly equals to -1 under applied strain.

$$\vartheta_{12} = \vartheta_{12} = -1 \quad (2\text{-}14)$$

The Young's modulus is given by Equation 2-19.

$$E_1 = E_2 = K_h \frac{4\sqrt{3}}{l^2[1+\cos(\frac{\pi}{3}+\theta]} \quad (2\text{-}15)$$

The above analytical models with rigid rotational polygons were created to explain the occurrence of NPR behaviour and they gave a clear image to researchers from the responsible mechanisms for this unique property. However, these simplified analytical models demonstrated the idealised auxetic behaviour, while the behaviour of the real auxetic materials was much more complex. The existence of the rigid rotational polygons was warranting that the PR value was constantly equal to -1 which is unlike the auxetic behaviour in real systems. In other words, these simplified analytical models overestimated the NPR's value and failed to predict the dependence of

the PR's value on some other factors such rigidity of rational polygenes or rational stiffness of hinges. This problem was corrected by employing developed analytical models to incorporate simultaneous mechanical deformation mechanisms which were possible to take place when the real material exhibited auxetic behaviour under mechanically applied load.

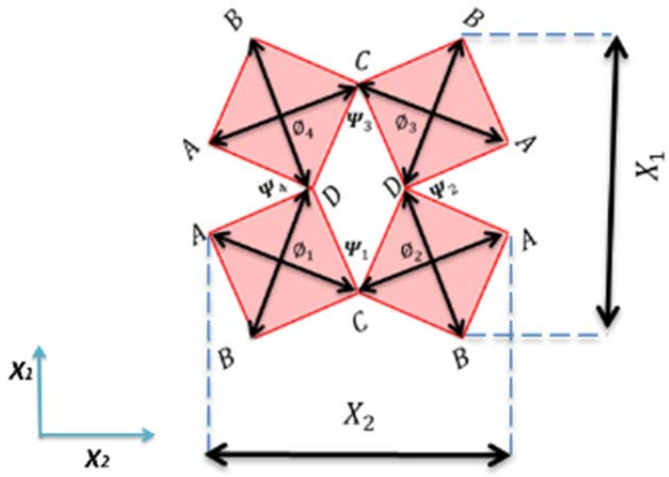

Figure 2-12 The geometry of the auxetic "rotating semi-rigid squares" structure.

For this purpose, Grima et al. [73] extended their earlier mathematical model that is describing the behaviour of 'rotating rigid squares' and proposed a new analytical model. The key improvement point of the new analytical model was that the squares were allowed to deform apart from rotating relative to each other [50]. The RVE of the new analytical model with rotating semi-rigid squares was presented in Figure 2-12. The rigid identical squares were replaced with their coupling diagonals where they were connected by a hinge at their intersection with a hinge stiffness of $k\phi$. The diagonals of identical neighboring squares were connected through a hinge with a hinge stiffness of $k\psi$ at an angle of ψ ($90 + \theta$ initially where θ is the angle between squares).

This arrangement of squares deformed through changes in the angles of ϕ and Ψ. According to Figure 2-12, there are four of ϕ and four Ψ for each unit cell as ϕ_1, ϕ_2, ϕ_3, ϕ_4 and Ψ_1, Ψ_2, Ψ_3, Ψ_4. According to geometry and symmetry considerations, it was assumed that the angles $\varphi_1 = \varphi_3$, $\varphi_2 = \varphi_4$, $\psi_1 = \psi_3$ and $\psi_2 = \psi_4$. The magnitudes of angles of $\phi_1$and ϕ_2 at different applied load depend mainly on rational stiffness of these two hinges (ϕ_1, ϕ_2,) and represented the deformation of squares. Also the

magnitudes of angles of ψ_1 and ψ_2 depended mainly on rational stiffness of these two hinges (ψ_1, ψ_2) which presented the position of neighbouring squares during the rotation.

Equation 2-16 and 2-17 are derived to measure the dimensions of the unit cell in the X_1 and X_2 directions under applied load.

$$X_1 = 2l_d[\sin(\frac{\psi_1}{2})] \quad (2\text{-}16)$$

$$X_1 = 2l_d[\sin(\frac{\psi_2}{2})] \quad (2\text{-}17)$$

The summation of internal angles of a geometric shape with n sides was equal to (n-2)π so according to Figure 2-12 the differential of angles of ψ_1, ψ_2, φ_1 and φ_4 were calculated through:

$$2\emptyset_{2+}2\emptyset_1 + 2\psi_1 + 2\psi_3 + 2\left(\frac{\pi}{2}\right) + 2\left(2\pi - \left(\frac{2\pi}{2}\right) - \psi_4\right) = 8\pi \quad (2\text{-}18)$$

$$d\psi_2 = d\psi_1 + 2d\emptyset \quad (2\text{-}19)$$

It was supposed that the direction of loading was in the X_1 direction. In order to drive a relation between $d\psi_1$ and $d\emptyset$, the moments acting on diagonals of squares were considered as shown in Figure 2-13. The Equation 2-20 presented the equilibrium Equation of active moments on **AC** diagonals as following:

$$\sum M = M_A + M_C - M_0 \quad (2\text{-}20)$$

Where the acting moments on diagonal were defined according to the rotational stiffness of hinges as following:

$$M_A = M_c = K_\psi d\psi_1 \quad (2\text{-}21)$$

$$M_o = K_\emptyset d\emptyset \quad (2\text{-}22)$$

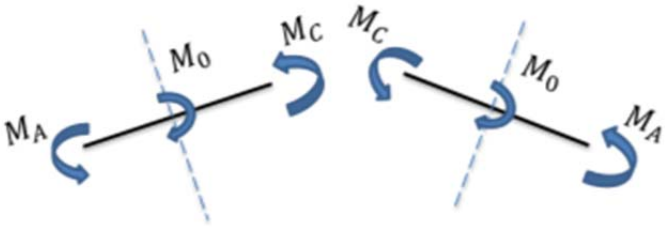

Figure 2-13 Schematic view of Moments acting on diagonal.

From the equilibrium Equation, the Equation 2-23 was derived to show the relation between $d\psi_1$ and $d\emptyset$.

$$d\emptyset = 2(\frac{k_\psi}{k_\emptyset})\left[1 + 4\left(\frac{K_\psi}{K_\emptyset}\right)\right]^{-1} d\psi_2 \quad (2\text{-}23)$$

The strain-dependent value of PR given as follow:

$$\vartheta_{ij} = -\frac{d\varepsilon_j}{d\varepsilon_i} \quad \text{Where i and j = 1, 2} \quad (2\text{-}24)$$

$$dX_1 = l_d cos\left(\frac{\psi_1}{2}\right) d\psi_1 \quad (2\text{-}25)$$

$$dX_2 = l_d cos\left(\frac{\psi_2}{2}\right) d\psi_2 \quad (2\text{-}26)$$

$$\vartheta_{21} = \vartheta_{12} = -\frac{dX_1}{d_{X_2}} * \frac{X_2}{X_1} = -\cot\left(\frac{\psi_1}{2}\right) \tan\left(\frac{\psi_2}{2}\right)\left[1 + 4\left(\frac{k_\psi}{k_\emptyset}\right)\right]^{-1} \quad (2\text{-}27)$$

From the derived formula it was found that before applying a load (when the strain was equal to zero), the PR's value was not dependent on the initial geometry of microstructure ($\psi_1 = \psi_2 = 0$) and it was the function of two types of rotational stiffness of k_ϕ, and $k_{\boldsymbol{\Psi}}$.

$$\vartheta_{21} = \vartheta_{12} = -\left[1 + 4\left(\frac{k_\psi}{k_\emptyset}\right)\right]^{-1} \quad (2\text{-}28)$$

The simplified Equation 2-32 presented the non-dependent value for PR when the strain was equal to zero. According to this formula, the range of PR is between 0 to -1. When k_ϕ tended to ∞, the answer of analytical model was similar to idealized behaviour or "rotating of rigid squares." As shown in Figure 2-12, the unit cell contained four $\boldsymbol{\Psi}_1$, four $\boldsymbol{\Psi}_2$ and four ϕ. Under applied load, the work that was done per unit cell was given by:

$$W = 4[\tfrac{1}{2}K_\theta(d\psi_1)^2] + 4\left[\tfrac{1}{2}K_\theta(d\psi_2)^2\right] + 4\left[\tfrac{1}{2}K_\emptyset(d\emptyset)^2\right] = 4\left[\frac{k_\psi(k_\emptyset+2k_\psi)}{(k_\emptyset+4k_\psi)}\right](d\psi_2)^2 \quad (2\text{-}29)$$

The strain energy per unit volume was given by:

$$U = \tfrac{1}{2}E_2(d\varepsilon_2)^2 = \tfrac{1}{2}E_2(\frac{dX_2}{X_2})^2 = \tfrac{1}{2}E_2\left[(\frac{dX_2}{d\psi_2})d\psi_2\frac{1}{x_2}\right]^2 \quad (2\text{-}30)$$

According to the principle of energy approach and volume of the unit cell, the Equation 2-33 was derived to present Young's modulus of the structure Ei.

$$U = \frac{1}{V}W \quad (2\text{-}31)$$

$$V = X_1X_2\,z \quad (2\text{-}32)$$

$$E_1 = E_2 = \left[\frac{8k_\psi(k_\emptyset+2k_\psi)}{(k_\emptyset+4k_\psi)}\right] sec^2\frac{\psi}{2}\frac{1}{l_d^2 z} \quad (2\text{-}33)$$

where z is the thickness in the third direction.

As mentioned before, the idealised analytical model of "rotating rigid squares" was very simple to predict the complex deformation mechanism of auxetic materials. Therefore several more complex analytical models were derived which included the influence of deformation of rotational polygons. Another analytical model from this class was presented by Grima et al. [77] as the "auxetic behaviour from stretching connected squares." In this model, the rotational squares were connected together by using some piston-like elements, and the angle between neighboring squares was fixed as shown in Figure 2-14.

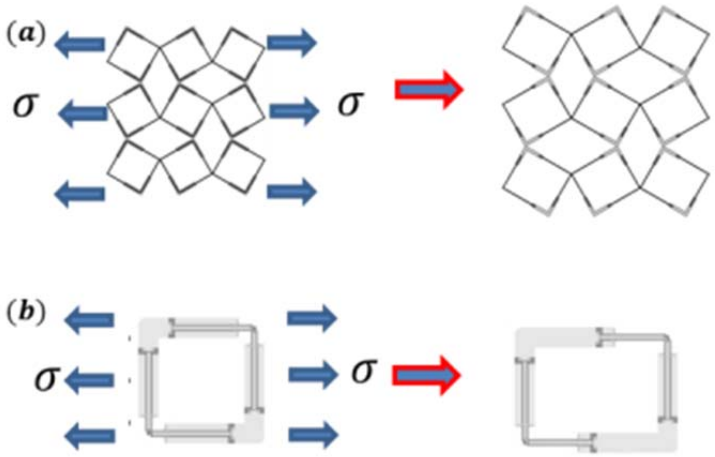

Figure 2-14 (a) The mechanism of auxetic behaviour from stretching connected squares; (b) piston-like elements with a fixed angle between neighboring squares.

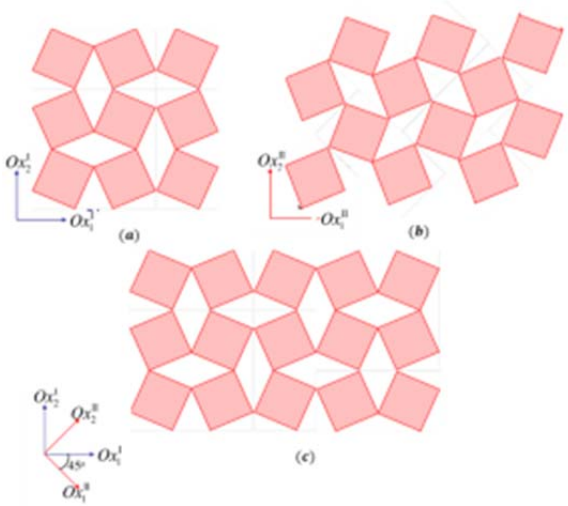

Figure 2-15 The geometry of analytical model of 'stretching connected squares'; (a) Orientation I; (b) Orientation II; (c) the geometric relation between the two orientations when the Orientation I is oriented at 45◦ with respect to Orientation II.

Therefore, the squares were allowed to deform their side lengths and changed their shapes from squares to rectangles or squares of different sizes without changing the angles in the system. The analytical model of "stretching connected squares geometry" was presented by two unit cells, referred to as Orientation 1 and Orientation 2, as shown in Figures 2-15a and 2-15b. It was shown that the Orientation 2 was oriented at 45◦ with respect to Orientation 1. In the simple analytical model of "auxetic behaviour from rotating rigid squares," the mechanical properties for both these orientations were equal, however in the case of the "stretching connected squares", the mechanical properties would be different.

Three simple Equations were derived to present the PR's value $\boldsymbol{\nu_{12}^{\zeta}}$, Young's moduli $\boldsymbol{E_1^{\zeta}}$ and shear modulus $\boldsymbol{G_{12}^{\zeta}}$ for the stretching mechanism at an angle $\boldsymbol{\zeta}$ to the Ox1-axis. Where $\boldsymbol{\theta}$ was the fixed angle between two squares, $\boldsymbol{\zeta}$ was the angle between orientation I and Orientation II, $\boldsymbol{K_s}$ was the stretching force constant which depended on base martial properties, and $\boldsymbol{Z}$ was the thickness in the third direction.

$$\nu_{12}^{\zeta} = -\frac{cos^2(2\zeta)\sin(\theta)}{1+sin^2(2\zeta)\sin(\theta)} \quad (2\text{-}34)$$

$$E_1^{\zeta} = \frac{2K_s}{z[1+sin^2(2\zeta)\sin(\theta)]} \quad (2\text{-}35)$$

$$G_{12}^{\zeta} = \frac{K_s}{z[1+cos(4\zeta)\sin(\theta)]} \quad (2\text{-}36)$$

It should be mentioned that this analytical model showed the possibility of deriving a model where the 'stretching squares' deformation mechanisms occurred exclusively (see Figure 2-14) similar to the idealised analytical model of 'rotating squares'. However, a new analytical model was required which would be more suited to the auxetic behaviour of real systems. It is worth to note that the real behaviour of systems was influenced by more than one idealised mechanism of 'rotating rigid squares' or 'stretching squares' model alone. In other words, it was found that auxetic behaviour can be retained even if it was assumed that the squares are semi-rigid, so the PR's value depended on two factors, firstly the amount of rotation of the squares and secondly the extent of deformation of the square. There are different ways in which the combined idealised mechanism can be derived. Attard et al.[13] derived a new analytical model using superposition of principles of two separate analytical

models of 'auxetic behaviour from stretching connected squares'[75] and 'auxetic behaviour from rotating rigid squares'[24]. The 'rotating–stretching analytical model' described the auxetic behaviour of real materials through hinging and stretching which are combined together. Eventually, the new analytical model was obtained for a system in which these two mentioned mechanisms acted simultaneously.

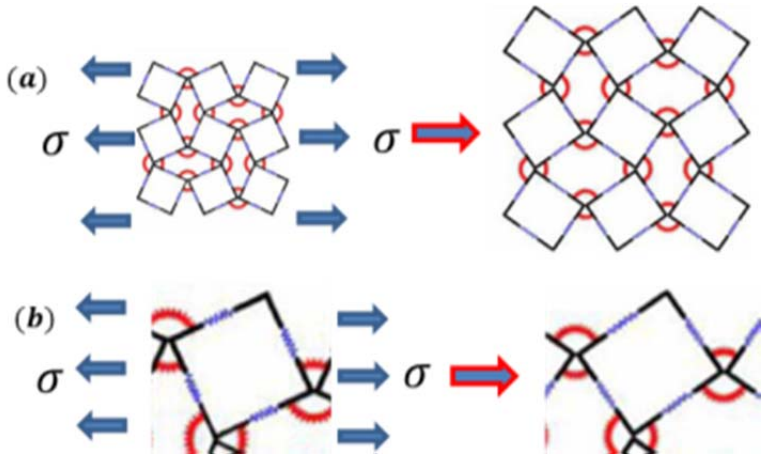

Figure2- 16 a) the mechanism of auxetic behaviour from rotating–stretching connected squares; (b) a connected squares element deforming through concurrent stretching and rotation of the squares relative to each other.

Three simple Equations were derived to present PR's value $\mathbf{v_{ij}^{SR}}$, Young's moduli $\mathbf{E_{ij}^{SR}}$ and shear modulus $\mathbf{G_{ij}^{SR}}$ for the rotating–stretching analytical model. As shown in Figure 2-16, this system constructed by several square elements with the side length $\boldsymbol{l}$ and thickness z which were deformable whilst $\boldsymbol{Ks}$ was the stretching force constant and presented by blue springs. These squares were connected together at an angle $\boldsymbol{\theta}$ by hinges with the rotational stiffness coefficient of $\boldsymbol{Kh}$ as shown in Figure 2-16. In contrast to the analytical model of "stretching connected squares" where $\boldsymbol{\theta}$ was the fixed angle, for "rotating–stretching analytical model", θ was defined as a variable parameter and was changed by applying stress.

$$\nu_{ij}^{SR} = -\frac{4\sin(\theta)+k[1-\sin(\theta)]}{4+k[1-\sin(\theta)]} \qquad (2\text{-}37)$$

Where:

$$k = (\frac{K_s}{K_h})l^2$$

$$E_i^{SR} = \frac{8K_sK_h}{4zK_h+K_szl^2[1-\sin(\theta)]} \qquad (2\text{-}38)$$

$$G_{12}^{SR} = \frac{K_S}{z[1+\sin(\theta)]} \quad (2\text{-}39)$$

All above analytical models predicted the auxeticity of soft materials and structures which deformed in the elastic range of the base material and the deformation was reversible and repeatable. However, when the deformation enters the plastic range for metallic structures and materials, several new features will emerge, which do not exist in the elastic deformation range such as permanent deformation and strain hardening.

2.1.3.2 2D and 3D auxetic soft CMS with various microstructure configurations

As mentioned before CMS are defined by a porous microstructure where the porous part can be natural heterogeneous caused by foaming process or can be very regular as a result of engineering manufacturing process.

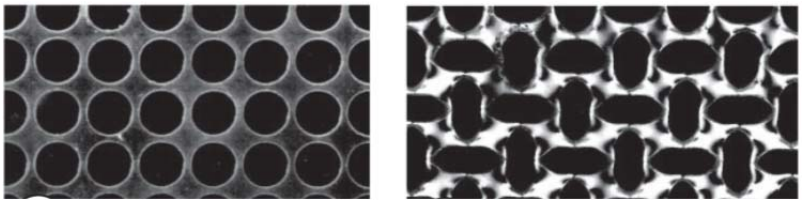

Figure 2-17 Experimental images of a 2D elastomeric lattice with circular holes at macroscopic strains of 0 and 3.5%. [103]

In the recent years, the interest of researchers was concentrated on the development of a manufacturing method to produce auxetic mechanical CMS with different geometries. The most popular method which solved the bottleneck of manufacturing of auxetic CMS, was changing the deformation pattern of bulk block of materials with positive PR which led to auxeticity. In other words, several pieces of bulk material were cut from a block or sheet, which resulted in a geometric configuration that was similar to several mechanisms with the possibility of exhibiting NPR behaviour. For the first time, this method was used by Grima et al. [24] to develop an auxetic deformation mechanism with rotational square elements. The rotating unit analytical model was realised in practice by Mullin et al.[103] through manufacturing a 2D latticed cellular structure which exhibited auxetic behaviour under applied load as shown in Figure 2-17. In fact, this 2D auxetic lattice opened several new avenues for designing new auxetic materials and structures at different levels of micron and nanoscales. The nonlinear stress–strain behaviour of cellular solids aroused a

great deal of interest because of energy absorption property. The mechanical deformation of 2D elastomeric lattice with circular was studied by Bertoldi et al. [4] and it was found that the observed deformation pattern can be used to trigger NPR behaviour. The experimental and numerical results revealed that, under compression, the 2D lattice exhibited a linear response caused by an initial structural instability of the cell's walls of microstructure and no auxetic behaviour was observed. When the applied stress reached a critical level, the initial instability led to a transformation of deformation pattern that developed simultaneously throughout the material. The experimental results clearly showed that the localised buckling mode which was similar to H&V alternation led to NPR behaviour under compression. In other words, the localised buckling mode altered ellipse with their long axes parallel to horizontal and vertical directions in the side parallel views. It was revealed that the pattern transformation of 2D lattice structure was reversible and repeatable. Bertoldi et al. [4] showed that a possible alternative to modifying the deformation pattern of a structure was using lower modes of linear buckling analysis, for example, replacing some holes with inclusions.

As mentioned before the performance of a metamaterial was dominated by the geometric features and deformation mechanisms of its microstructure. For a certain mechanism, the geometric features have bounds in which the performance of a metamaterial such as NPR can be designed. The previous investigation on buckling-induced auxetic metamaterial revealed that there was a geometric limit for its microstructure to exhibit auxetic behaviour in infinitesimal deformation. It was investigated that the size, arrangement, shape and volume fraction (percentage of porosity) of void parts had a significant effect on stability and global response of buckling-induced cellular metamaterials.

Accordingly, the dependence of auxetic property of 2D elastomeric lattice with circular holes on the percentage of porosity was studied by Bertoldi et al. [5]. The percentage of porosity was presented with the term ϕ which was defined as the ratio of the total area of voids divided by the surface area of the sample. The numerical results showed that when $\phi \leq 0.34$ the macroscopic instability firstly was happened along the direction of applied load. Therefore, the instability led to total buckling of structure in the form of collapsed band of holes. The PR's value was measured directly from the numerical results on the (representative volume elements) RVEs that contained four unit cells, and

using the nominal strains in axial and lateral directions. It should be mentioned that for $\phi \leq 0.34$ the PR's values was always positive under an applied load. In contrast, when $\phi > 0.34$, NPR behaviour was originated from the localisation of buckling mode which triggered a global change in the deformation pattern. The buckling in walls of unit building cell led to an alternate rotation of rigid parts and suddenly produced a square of ellipses with horizontal and vertical parallel axes. Experimental results showed that the 2D lattice structure exhibited positive PR's value up to a critical value of strain. Upon the critical strain, the deformation pattern was changed which was originated from the linear instability of cell's wall of the microstructure. Therefore, the PR's value decreased until it eventually became negative. The relation between the architecture of microstructure and the nonlinear stress-strain behaviour of cellular metamaterials has been an open research area for many researchers. Accordingly, Bertoldi et al. [59] conducted a systematic numerical investigation to identify the influences of changing of pore shape geometry on the non-linear response of a 2D elastomeric lattice with circular holes when the porosity, hole arrangement and loading conditions were constant. It was concluded that the pore shape resulted in structural stability, critical strain, but mainly affected on changing the deformation pattern from local buckling of the microstructure (led to NPR) or total buckling and collapse of structure(no NPR). As a result, it was found that only a few number of pore shapes led to periodic structures with the possibly of buckling induced instability and NPR behaviour. Also, it was indicated that a little reduction in porosity led to a wide range of pore shapes which were reversible and applicable and took the advantage of mechanical instabilities at critical strains. In other words, it was shown that through changing the pores shape, the non-linear response of a soft porous structure could be tuned and optimal structure could be designed [59]. Also, it was shown that the circular pores did not lead to optimal response and the compaction of the system could be significantly improved through a careful design of the pore shape [59].

As mentioned before, the most popular method for solving the bottleneck of manufacturing of auxetic CMS was changing the deformation pattern of bulk block or a sheet of materials with positive PR which leads to auxeticity. Another try to realize the mechanism of rotating polygons models in practice was done by Grima et al. [104] through cutting diamond and star perforations in sheets as

shown in Figure 2-18. The sheet was made from available conventional non-crystalline materials, and the capability of auxetic behaviour for both structures was investigated by FE simulations. It was shown that the auxetic behaviour of these 2D porous structures was originated from the mechanism of "rotating rigid triangles".

Figure 2-18 Realisation of the mechanism of rotating polygons models in practice through cutting diamond and star perforations in sheets was done by Grima et al. [104].

Several 2D auxetic metamaterials were presented by Mizzi et al [105] through cutting slit perforations in sheets. As illustrated in Figure 2-19 The perforations were cut based on different patterns to create a novel class of metamaterials with different auxetic mechanisms such as rotating polygons, chiral, nodule fibre, and other models with respect to their potential to exhibit a NPR. The simplicity of the presented technique led to deliver an extensive possibility for different applications such as skin grafting.

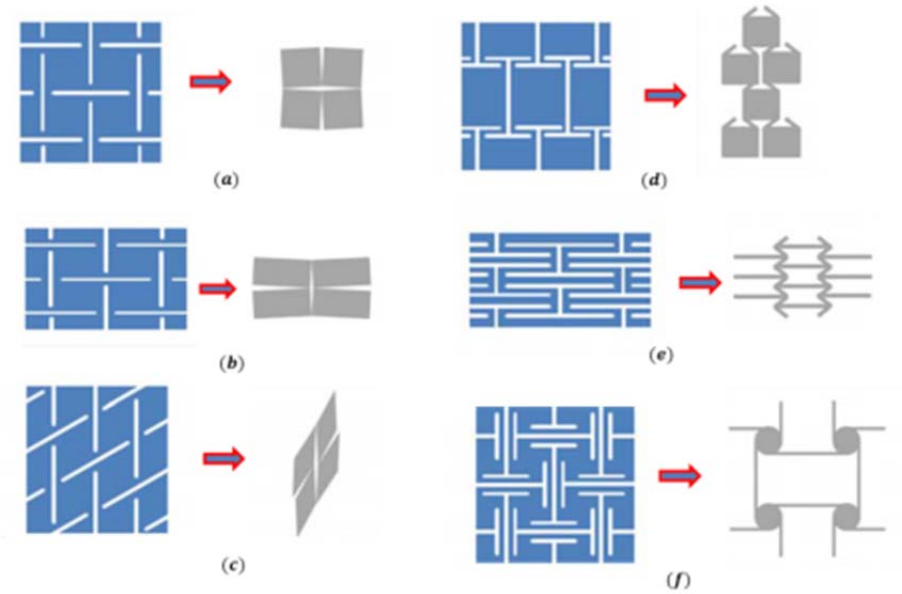

Figure2- 19 Slit perforation patterns with corresponding mechanisms; (a) rotating rigid squares; (b) rotating rigid rectangles; (c) rotating rhombi; (d) fibrils and nodes; (e) re-entrant honeycomb; (f) anti-tetra chira.

It is worth to note that natural materials with unique behaviours such as NPR behaviour were less symmetric. Also, most of the literature focused on symmetric ideal 2D systems without any randomness in their design or imperfections. Motivated by this fact Grima et al.[106] investigated the possibility of auxetic behaviour from the sheets with randomly oriented cuts as shown in Figure 2-20.

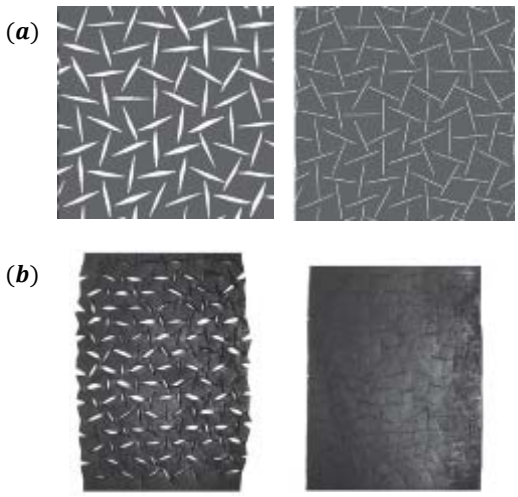

Figure 2-19 Non-symmetrical 2D system without randomness cuts presented by Grima et al.[106]; (a) FE simulations; (b) experimental results.

It was shown that through the definition of several of nonsymmetrical quasi-random cuts, the deformation pattern of a regular conventional elastomeric sheet was changed and a new 2D elastomeric metamaterial with auxetic behaviour was generated. The most important advantage of this nonsymmetrical 2D system was a high degree of perfection which was not necessarily required to produce these systems. This important advantage made the new 2D auxetic system practical for use in different applications.

Recently, a 2D porous solid with planar auxetic and isotropic behaviour was presented by Carta et al. [107]. The pores disposition with 45° rotation relative to each were introduced inside the 2D structure as shown in Figure 2-21 where **l** was the side of the hexagon and **θ** was the orientation angle of the perforations with respect to the normal to the hexagonal sides. Numerical and experimental results were conducted to reveal that the effective NPR property was independent of boundary conditions also it was scale-independent. The results of the parametric study revealed that the PR's value of the new system strongly was influenced by the relative orientation of the pores. The most

important advantage of the new designed system was that it was simple to manufacture and tuneable for a great variety of industrial applications.

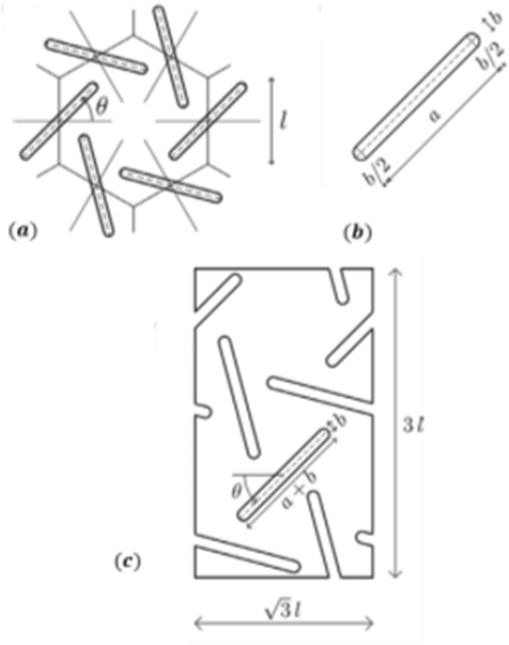

Figure 2-20 (a) The pores disposition with 45 °rotation relative to each were introduced inside the 2D sheet, where l was the side of the hexagon and was the orientation angle of the perforations with respect to the normals to the hexagonal sides; (b) detail of perforation; (c) representative unit cell of the infinite periodic structure.

All the above mentioned auxetic cellular systems were 2D with a porous microstructure. Theses 2D systems were formed through the introduction of the regular patterns of pores into the sheet of conventional materials to change the deformation pattern of the sheets with positive PR. This alternative was extended to design a new class of 3D auxetic cellular metamaterials with the possibility of retaining this unusual response over a wide range of applied strains. In other words, through the introduction of regular patterns of pores into a bulk block of conventional materials, the deformation pattern of the bulk block with positive PR was changed to a new CMS that led to auxetic behaviour. For this purpose, a new design approach for 3D soft metamaterial with auxetic behaviour was proposed by Babaee et al. [3] using "buckliball" as the building cell which extended the strain range further to 0.3. Three different types of a unit building block with 4, 6 and 12 holes were generated as shown in Figure 2-22. The geometric configuration of proposed unit building cells consisted of thicker parts and thinner links. Under applied strain, the local buckling induced instability at the walls of a unit cell led to the transformation of deformation pattern of system and NPR

behaviour. In other words, the buckling in thinner parts of unit building cell led to an alternate rotation of thicker parts and suddenly produced a new mechanism which was similar to auxetic mechanism "rotating of rigid squares."

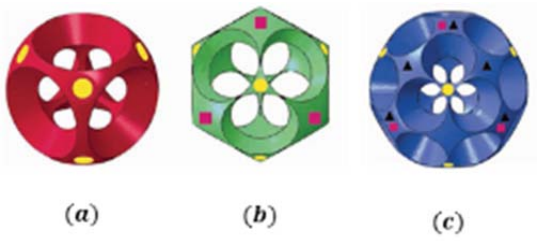

Figure 2-21 Topologies of 3D unit building blocks with 6, 12 and 24 holes

However, it is worth to note that the topologies of proposed building blocks were relatively complicated and the fabrication processes problems such as removing supporting materials from 3D printed sample or extra bonding interface, led to inaccuracy in the mechanical properties measurements. Motivated by this bottleneck, Shen et al. [7] developed a series of the novel design of auxetic metamaterials using buckling mode with NPR behaviour which was originated from two types of simple building cells. The geometric configuration of the first type of building block consisted of a void sphere inside a cube and the second geometry type consisted of a void octahedron inside a cube as shown in Figure 2-23.

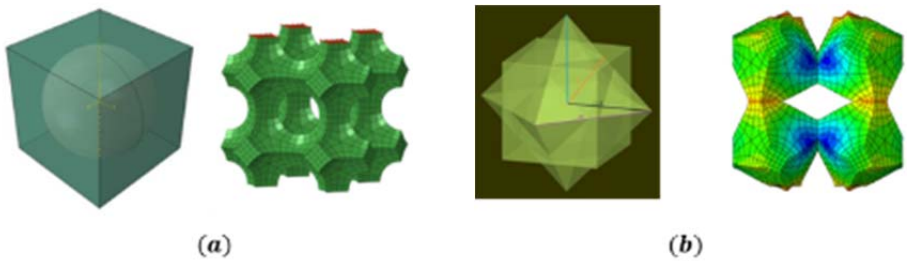

Figure2- 22 Topologies of simple 3D unit building blocks; (a) building block consisted of a void sphere inside a cube; (b) building block consisted of a void octahedron inside a cube.

Those NPR metamaterials with simple building blocks had a tuneable auxetic behaviour which was strain-dependent under both tension and compression. It had the potential to be used as a mechanism for redistributing the base material of the metamaterial according to the external loads so as to support the external loading more effectively [7].

The numerical investigation was accomplished to consider a geometrical controllable parameter for a simple 3D auxetic metamaterial to control the volume fraction and through the buckling analysis. A line strip for this controllable parameter was defined to provide the volume bounds in which the designed metamaterial exhibited auxetic behaviour in infinitesimal deformation. A relation between the void volume fraction and the auxetic properties was investigated through numerical analysis. The void volume fraction or $\emptyset$ was defined as a ratio that was composed of the derivation of the total volume of the void part by total sample's volume. Regarding the first type of the building block, the void volume fraction depended on the radius length of the spherical void part of the model. By changing the radius of the void part, volume fraction was changed. Because of the geometrical limitation, a range was defined for the length of sphere radius. The minimum value of radius is 6.65 mm and the maximum is 8.8 mm. For this range of the radius, the $\emptyset$ could be changed between 25.5% to 96.35%.

As mentioned before, the NPR behaviour of buckling-induced auxetic metamaterials was originated from the localised buckling mode shape. The linear buckling analysis was employed to find the bounds of the geometric parameters as the effective range of auxetic behaviour. If the first buckling mode was similar to the desired local buckling pattern, the bulk material had auxetic behaviour under compression. A systematic study was carried out by varying the defined parameters. The results of the numerical investigation revealed that the critical value of the diameter of the sphere was 7 mm which was corresponding to the volume fraction of 0.31. Thus, for the sphere-in-cube design, the NPR behaviour would most likely occur when spherical diameter ranged from 6.65 to 7 mm.

Therefore, a geometrical controllable parameter was defined for a simple 3D auxetic metamaterial to control the volume fraction and through the buckling analysis, a line strip for this controllable parameter was defined to exhibit auxetic behaviour in infinitesimal deformation. However, it should be mentioned that the limit for auxetic metamaterials undergoing large deformation is different from that under small deformation and has not been reported yet. Auxetic

behavior in an infinitesimal deformation range usually does not have any practical value to use it in the applications to control the auxetic performance for efficient usage.

2.2. Auxetic metallic materials and structures

Only a few researchers studied the NPR performance of metallic auxetic metamaterials undergoing large plastic deformation. Therefore the knowledge on the deformation features and auxetic performance of metallic metamaterials is very limited. Here, the works those presented systemic approaches to design auxetic metallic materials and structures have been reviewed.

Friis et al. [60] did a seminal work in this research area and investigated the NPR behaviour of a non-periodic copper foam. Three different methods were proposed to transfer the material properties of conventional foams to re-entrant metal foams such as triaxial compression followed by heat treatment for thermoplastic polymer foams, triaxial compression during the foaming process for thermosetting polymer foams and sequential plastic compression in three directions for metal foams [60]. The idealized unit cell of re-entrant foam and conventional foams were presented in Figure 2-24. It was found that the NPR's value and Young's modulus of the re-entrant foams were smaller than conventional foams. Also, it was shown that re-entrant foams were more flexible than the corresponding conventional foams. The deformation pattern of the re-entrant transformation of metal foam originated from two different mechanisms, both plastic hinge formation and plastic buckling of the cell ribs.

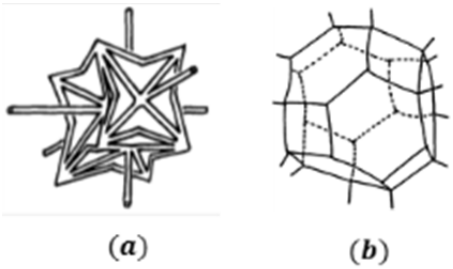

Figure 2-23 Idealized unit cell; (a) re-entrant foam; (b) conventional foam.

Following that Taylor et al.[61] presented a 2D metallic auxetic periodic structure with low porosity through the introduction of a square array of mutually orthogonal elliptical voids inside a 2D metallic sheet as shown in Figure 2-25.

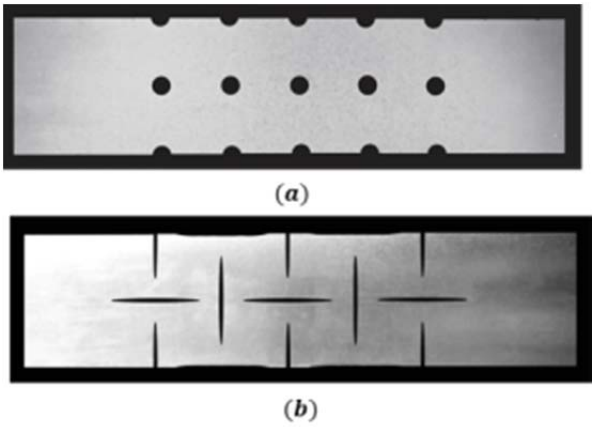

Figure 2-24 2D metallic auxetic periodic structure with low porosity; (a) aspect ratio is 1; (b) aspect ratio is 30.

According to experimental and numerical results, it was shown that the PR's value of the new designed system was influenced by the dimensions of the voids of pores microstructure. An aspect ratio was defined to control the geometry of voids of microstructure which was the relation between height and width of the holes. The minimum value of aspect ratio was 1 when the shape of the holes is circular as shown in Figure 2-25a. By increasing the aspect ratio, the shape of voids was changed from circle tho ellipse. In this minimal system, the PR's value can be effectively controlled by changing the aspect ratio of the voids. For low aspect ratios, the structure was characterised by positive values of PR. However, as the aspect ratio increased, the PR was found to decrease monotonically and eventually becoming negative. Another research in this area was carried out by Dirrenberger et al. [62] on the auxetic behaviour of the metamaterial undergoing plastic deformation. The full-field numerical simulations were conducted on an auxetic periodic hexachiral lattice and the elastoplastic property was characterised by the yield strain, failure strain and the ratio of ultimate strength to yield strength of base materials.The mechanical properties of the auxetic system in the plastic zone were explored and It was found that the auxetic behaviour of structure in the plastic zone remained and the auxetic behaviour became even stronger with plastic yielding. Also, it was shown that with the expansion of plastic zone, the auxetic behaviour of the system was disappeared because of the plastic anisotropy response for the 6 fold symmetric lattice which was becoming weaker with plastic saturation. Moreover, the elastoplastic behaviour of the periodic microstructural arrays that

can exhibit NPR' value was investigated by Gilat et al. [108] through using a continuum-based micromechanical model.

2.3. Materials and structures with negative linear compressibility behaviour

The second scope of this study is to develop new materials and structure with the unique behaviour of NLC for desired application. In recent years, there has been increasing interest in the NLC behaviour, mostly due to its many potential applications which were mentioned before. Similar to auxetic materials and structures, the NLC materials and strucutures can be classified as naturally occurring or artificial. Also according to occurring level of NLC property, NLC materials and structures can be classified into two main categories of the molecular level and micro or macro level. The class of molecular or non-structural occurring level is out of the scope of this research and the focus area of this research is limited to artificial NLC structures and materials in the micro and macro occurring level.

For the first time Baughman et al. [14] presented a basic structural type deformation mechanism that was called "wine-rack–like deformation mode" to explain the NLC effect. The schematic view of the "wine-rack–like deformation mode" is presented in Figure 2-26. According to the presented deformation pattern, the NLC behaviour arose from the operation of hinged joints or bending at nodes of frameworks. This deformation pattern included the materials with the structures of wine-rack, honeycomb, hexagonal, rhombic and other related geometries that deformed like the wine-rack mechanism [22, 23, 65].

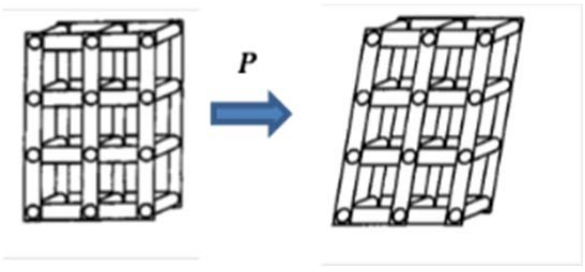

Figure2- 25 Schematic view of win–rack like deformation model.

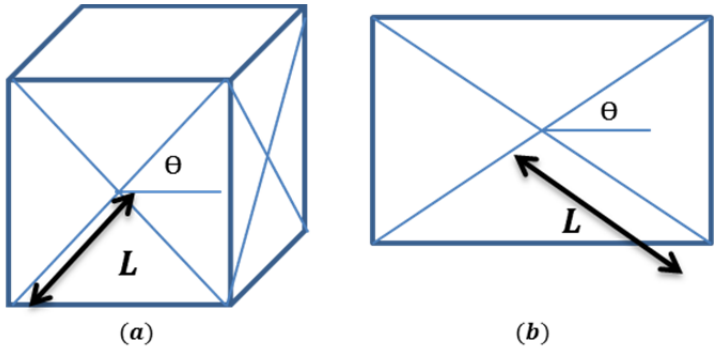

Figure 2- 26 Beam structure nomenclature; (a) show the layout of the 2D structure; (b) show the layout of the 3D structure.

It is noted that most of the artificial NLC materials and structures have a pre-determined topology. For example Barnes et al [109] used FE simulations to reveal the NLC property of a tetragonal structure that consists of a network of bending beams. The responsible mechanism for NLC property of the new structure was identified and a new analytical model was developed based on beam theory to explain FE results as shown in Figure 2-27. It was shown that the NLC property of these 2D and 3D structures were influenced by angle at the central intersection of bending beams. Therefore it was possible to optimize the structure for NLC by adjusting the angle. The optimum angle for maximum absolute NLC was 25.9° to 64.1° for 2D structures while for 3D type this was slightly changed to 26.6° to 61.2°.

In the Following, Grima et al.[22] showed that the NLC property may be exhibited by systems having high positive PR (non-auxetic), including non-re-entrant hexagonal honeycombs and wine-rack models as shown in Figure 2-28. The new proposed system was deformed through changing the angles between ribs of structures.

The mechanical property that has the possibility of leading to NLC property is auxetic behaviour. Therefore it is possible that the NLC property occurs simultaneously with NPR property along one or two perpendicular directions to NLC axis. Grima et al. [23] realised this concept through presenting an elongated hexagonal dodecahedron with NPR and NLC/NAC properties as shown in Figure 2-29. Similar to the most of the structure with NLC behaviour, the new designed structure was deforming through changing the angles between the ribs and hinging mechanism. It was shown that the new designed structure exhibited NPR in a particular plan when the geometry in that particular plane is re-

entrant. However, the same structure with non-re-entrant geometry exhibited positive PR's value in the particular plane. It was found that the angles between ribs and horizontal lines were independent, therefore the in-plane deformation of this 3D system along different planes was tuneable.

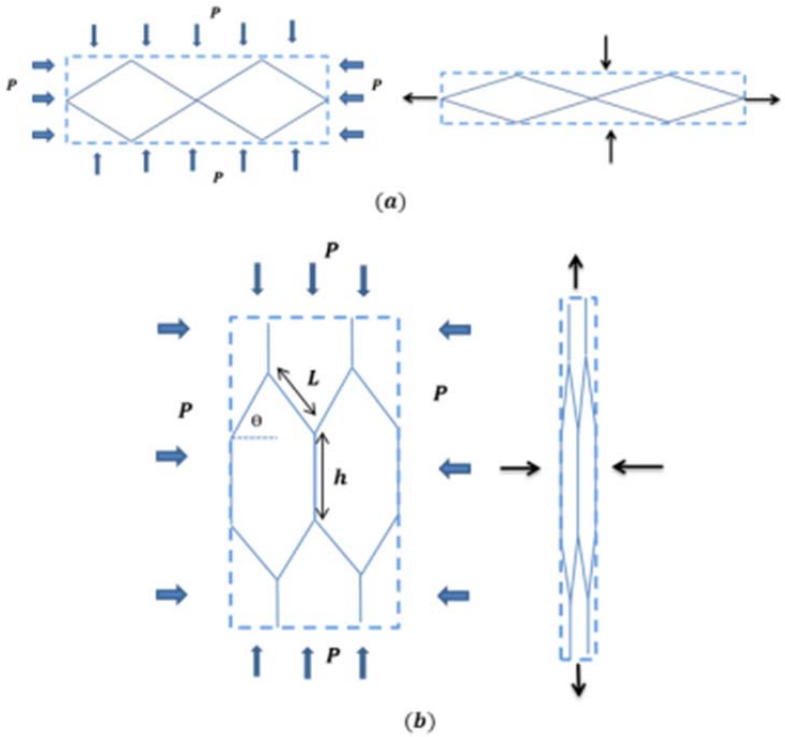

Figure 2-27 The proposed (a) hexagonal honeycomb and (b) wine-rack model which may exhibit negative linear compressibility when placed under a hydrostatic stress p.

Hence, it was possible to have negative, zero or positive PR's values in different planes simultaneously. Also, the new designed structure had the possibility of exhibiting NLC property when the geometry of structure was non-re-entrant at least in one particular page.

It should be noted that all the above mentioned NLC materials and structures have the pre-determined topologies and they were not developed through a general technique for designing materials with NLC property. For the first time Xie et al. [42] proposed a new materials design approach using topology optimization for designing new materials with NLC/NAC, zero linear compressibility (ZLC) and zero area compressibility (ZAC).

The optimization method was based on the bi-directional evolutionary structural optimization (BESO). The main idea of BESO was that by removing ineffective material in a gradual way from a

raw structure and redistributing the material to the most critical locations to develop the structure to an optimum.

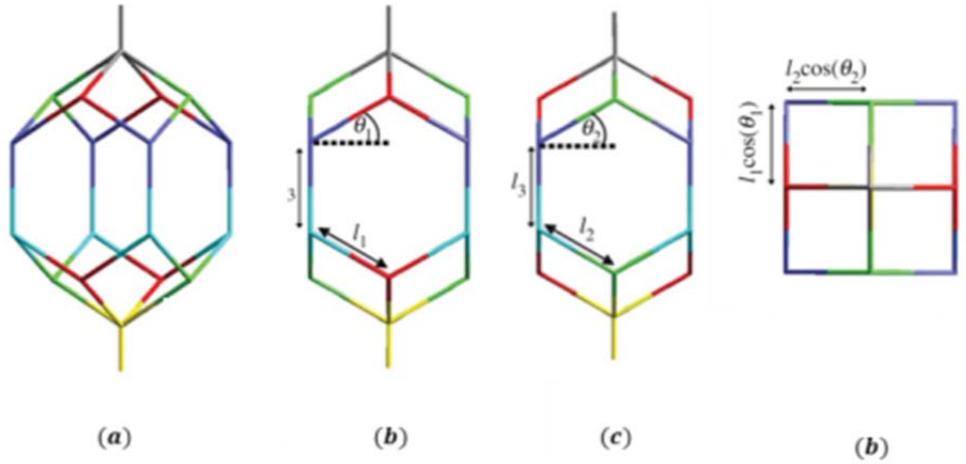

Figure2- 29 The re-entrant microstructure (elongated hexagonal dodecahedron) with NPR and NLC/NAC properties; (a) 3D view; (b) first lateral view; (c) second lateral view (d) top view. Where L_1 , L_2 and L_3 are the lengths of ribs. Θ_1 and Θ_2 are the angle between ribs and horizontal line.

A new 3D unit cubic cell was presented and the new materials were constructed as arrays of microstructures as shown in Figure 2-30. The material properties were determined using the homogenization theory. The experimental sample was fabricated using a 3D printer with NLC property and was tested in the laboratory under both unidirectional loading and triaxial compression. The experimental results are compared with the numerical predictions.

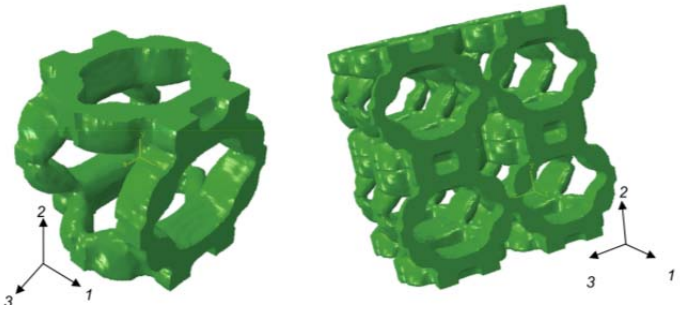

Figure 2-28 Topology of obtained NLC material; (a) unit cell; (b) array of 2 x 2 x 2 cells.

NLC composite materials and structures are rare in the literatures and so far have been found in a very limited range of applications. For the first time Baughman et al. [14] presented a composite material with NLC performance that consisted of a continuous network with a helical chain configuration in low-density porous solid as showin in Figure 2-31.

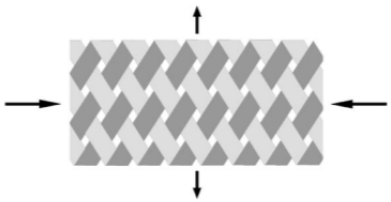

Figure 2-29 continuous network with a helical chain configuration of composite material.

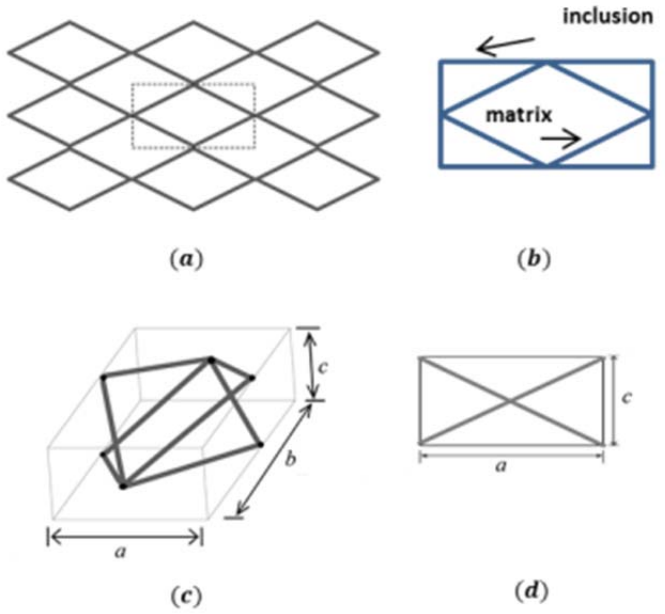

Figure 2-30 A schematic view of a 2D an d 3D composite model with continues network; (a) a periodic array of 2D composite network; (b) a unit cell of 2D composite network consists of network and matrix; (c) unit cell of 3D composite network; (d) lateral view of unit cell of 3D composite network.

In the following, Weng et al. [110] investigated the 2D and 3D composite materials with a rhombus-like hinged framework inside the filler component as shown in Figure 2-32.

The NLC behaviour of these NLC materials was originated from the wine-rack–like deformation pattern of the embedded networks. Also, a systematic parametric study was conducted to consider the influence of The ratio between modulus of elasticity of matrix and inclusions on NLC property.

Recently Miller et al. [111] presented some common materials particularly carbon fiber composites that exhibited NLC. All the above mentioned NLC composites have the embedded networks with predetermined and continuous topology so that the NLC property arises from the function of hinged joints. Thus, the corresponding mechanism for NLC can be presented by a wine-rack model which is frequently used to quantify NLC properties.

2.4 Applications in negative pressure wound therapy system

At the end of most surgical incisions into the abdominal cavity, the abdominal fascia can be closed primarily. However, sometimes full fascial closure is not possible and the operating surgeon is forced to leave the abdomen open. The open abdomen caused mortality rates of 30%[112-115]. Recently, a greater understanding of intra-abdominal hypertension and abdominal compartment syndrome caused to the development of a great range of surgical and non-surgical measures in an attempt to reduce the number of mortality [116, 117]. Three most commonly results in the commencement of an open abdomen are as follows: 1) Bowel edema which caused by infection, 2) expanded bowel during surgery and 3) increase intra-abdominal pressure in patients with abdominal compartment syndrome (ACS)[118]. In These cases, the intra-abdominal pressure persists after the laparotomy, and the surgeon must leave the abdomen open, and the open abdomen requires temporary closure.

Different techniques were employed for temporary abdominal closure. It should be noted that after temporary abdominal closure, the abdominal fascia must be closed primarily [112, 119-124]. However, many surgeons instead of primary fascial closure they use mesh and granulation tissue with split-thickness skin grafting to close the abdominal wound. In case of persistent visceral edema, loss of domain, or lateral retraction, the only option is to close the wound with mesh or granulation tissue with split-thickness skin grafting [125].

Whilst the abdomen remains open, numerous methods of temporary abdominal closure have been described, including towel clipping of skin edges, adhesive drapes, open packing, zipper closures, the Wittmann Patch, synthetic mesh, various plastic closures (such as the Bogot´a Bag, using an empty, opened intravenous fluid bag). However, the commercial acceptance and Wound Preservation are not applicable. Also, they may cause penetration or breaks of the skin.Recently, the new, different forms of negative pressure (suction) wound therapy is using which is a new commercially available device specifically designed to facilitate management of the open abdomen where primary closure is not possible or advisable, or where repeated planned abdominal entries (‘re-looks’) will be required.

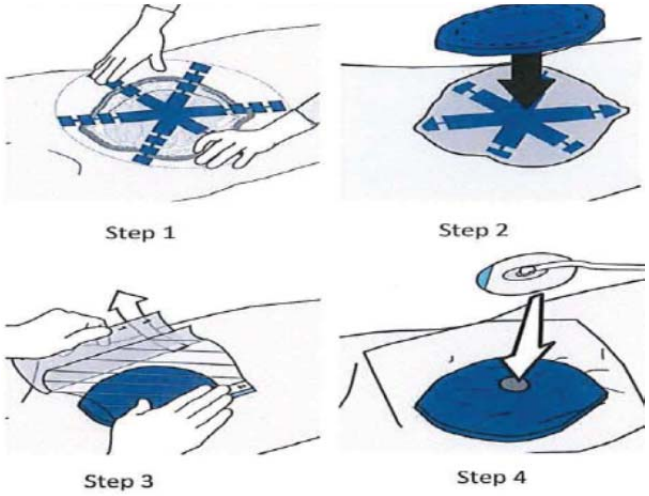

Figure 2-31 Illustration of NPWT procedure for open abdomen.

The other design aims are providing a separate surface between wound and external region, sucking out infective fluid and material from the wound when applying sufficient pressure, reducing the swelling size and removing exudates. In the proposed modified NPWT system shown in Figure 2-33, a vacuum will be fitted to control the pressure in the abdomen cavity. The method of treating a wound consists of placement of a wound filler of into a wound bed; covering the wound filler with a wound cover; and applying negative pressure to the wound cover. The net pressure on the smart foam is the combination of the pressures induced by pumps and the forces from the drapes as shown in Figure 2-34.

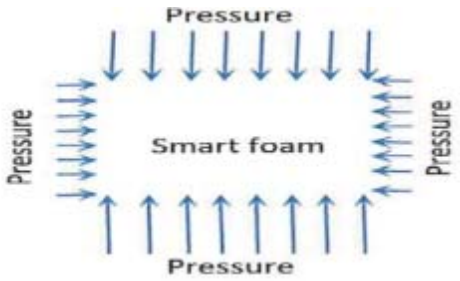

Figure 2-32 Loading condition and preferred deformation pattern for the inserted foam.

Smith & Nephew, the industry partner of this project, invented different patents as the wound fillers and include applications in negative pressure wound therapy such as patents with International Application numbers PCT/US2013/050619, PCT/US2013/050698 PCT/IB2013/001555, PCT/IB2013/001562 and PCT/IB2013/002485 [126-130]. Due to The drawback of the existing products include: (1) high cost of the device (2) invasiveness of the procedure (3) detrimental pressure

on the abdominal contents from the bowstringing effect (4) poor cosmesis of the healed wound geometric complexity, their uses in wound therapy applications are still very limited.

By enhancing the horizontal collapse of the wound filler through reducing the vertical movement of middle part of wound filler, and by reducing attachment of the wound filler to the wound margins, improved wound closure can be obtained. Smith & Nephew invented a pattern with international application number PCT/IB2013/001555 where in upon application of negative pressure to the wound filler, the wound filler is configured to contract horizontally with the vertically extending members reducing vertical movement of the wound filler [126]. Also, another product with international application number PCT/IB2013/002485 consists of comprising a support member and a cover member positionable over the wound in use. The support member can support at least a middle portion of the cover member above a surface of the wound so as to define a space between the wound cover and the wound [130]. Also, they are currently using normal black foams or gauzes for NPWT do not have such desired behaviour under negative pressure. The current black foam although, there is potential to significantly improve on these by making them easier to shape and cut, and at a lower cost.

Chapter 3

Development of auxetic metamaterial based on functionalization of base materials and topologies

Cellular materials and structures (CMS) have a variety of useful physical, mechanical and thermal characteristics that solid materials don't have it. The physical properties of CMS are influenced by the base material property and geometric configuration of their microstructure. The performance of a metamaterial is dominated by the geometric features and deformation mechanisms of its microstructure. Some of these deformation mechanisms are influenced by the nonlinear material properties of its base materials. In this Chapter, the geometric bounds of designed auxetic metamaterials are identified first through different analysis approaches in Section 3.1. Then the influence of metallic base materials on auxetic performance of buckling-induced are explored in Section 3.2. Special features caused by plasticity of metallic base material are identified. Those findings are applied in designing for a 2D planar auxetic metamaterial in Section 3.3 and corresponding theoretical models to predict the variation of NPR with respect to strain and plasticity are derived in Section 3.4.

3.1 Geometric bounds for buckling-induced auxetic metamaterials undergoing large deformation

For a certain mechanism of CMS, the geometric features of microstructure have bounds in which the performance of a CMS such as negative Poisson's ratio (NPR) is present and tuneable. The previous investigation on buckling-induced auxetic metamaterial revealed that there is a geometric limit for its microstructure to exhibit auxetic behaviour in infinitesimal deformation. As discussed in the chapter 2, section 2.31, the effect of void shapes on nonlinear response of a planner metamaterial was investigated by Bertoldi et al. [59]. More recently a geometrical controllable parameter was defined for a simple 3D auxetic metamaterial to control the volume fraction by Shen et al. [7]. A bound for this controllable parameter was defined through buckling analysis and was expressed graphically as a line stip within which the designed metamaterial exhibited auxetic behaviour in infinitesimal deformation. For both studies, the geometric limits of the microstructures of auxetic metamaterials were investigated in the elastic and infinitesimal deformation range. However, the limit for auxetic metamaterials undergoing large deformation is different from that under small deformation and has not been reported yet. Therefore, the auxetic behaviour under large deformation of buckling induced auxetic metamaterials was influenced by the shape and size of the void part of the microstructure. In the first part of this chapter, the geometric limit was investigated in an elastic and infinitesimal deformation range using linear buckling analysis. Then, experimentally validated finite element models were used to identify the geometric limits for auxetic metamaterials undergoing large deformation. Depending on the control parameters of the topology, the bounds were represented graphically by a line strip for one controlling parameter, an area for two controlling parameters and spatial domain surrounded by a 3D surface for three controlling parameters.

3.1.1 Microstructure

A 2D elastomeric buckling-induced auxetic structure with four geometrical parameters was used to represent the geometry of microstructure because of their simplicity. The geometry of the investigated structure is similar to the 2D buckling-induced structure which has been designed by Mullin et al. [103]. These parameters have been defined to control the size of the void part of the microstructure.

Respectively, T_A denotes the thickness of thinner part of unit building cell; T_B represents the thickness of thicker part of unit building cell, L_A shows the length of thicker part of unit building cell and L_B is the center to center distance between neighboring units building cells in the unreformed configuration as shown in the Figure 3-1.

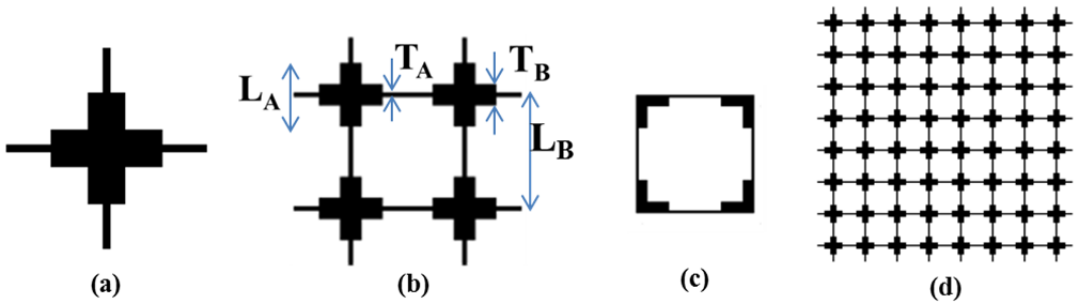

Figure 3-33 Buckling-induced auxetic structure; (a) unit bundling cell of 2D structure; (b) representative volume element for the structure; (c) topology of the void part of the structure; (d) bulk structure for numerical and experimental investigation ($0< T_A< T_B$, $0< L_A< L_B$, $0< T_B< L_A$).

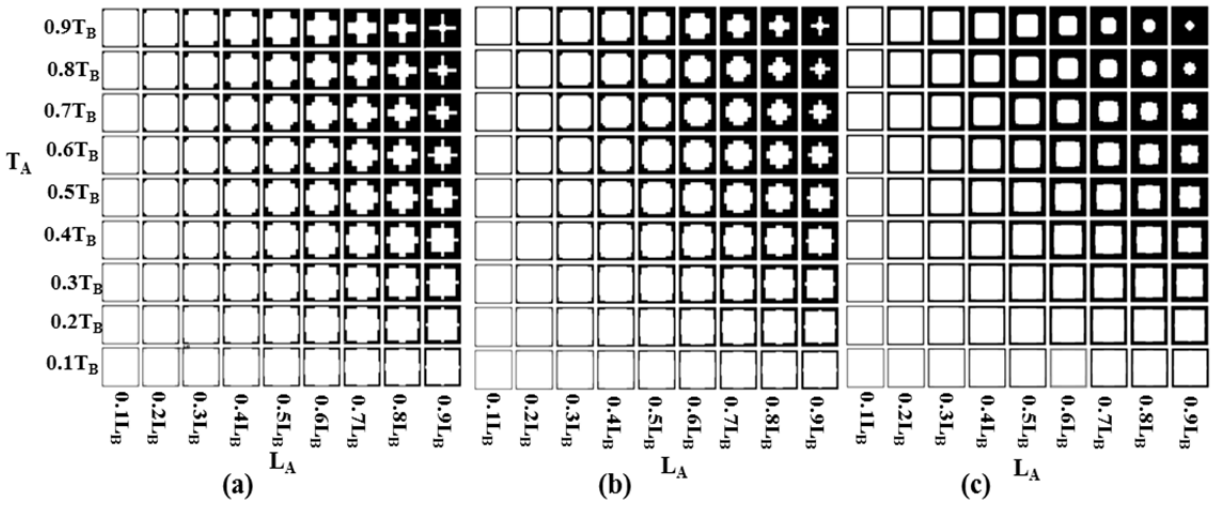

Figure 3-34 Examples of variation of geometric parameters on the microstructure of 2D structure; (a) for T_B=0.3 T_A; (b) for T_B=0.6 T_A; (c) for T_B=0.9 T_A.

Through changing these geometric parameters, a variety of microstructures with different void sizes can be obtained as shown in Figure 3-2. For example, L_B is fixed as a constant value and T_B=0.3T_A, by changing L_A and T_A a variety of microstructures can be produced as shown in Fig 3-2a. Respectively, Figure 3-2b and 3-2c are presenting microstructures when T_B=0.6 T_A and T_B=0.9 T_A.

3.1.2 Modelling

FE simulations were conducted to investigate the nonlinear response of the periodic 2D elastomeric buckling-induced auxetic structure. Firstly, the geometry of model and boundary conditions were

introduced. Then the microscopic or macroscopic instability of structure was investigated by using linear buckling analysis. Finally, the post-buckling analysis was conducted to investigate the deformation pattern of the structure under large deformation.

For purely elastic models, Young's modulus was 0.925±0.02 Mpa, and the PR's value was found to be 0.48. In order to form the bulk material, eight building cells (see Figure 3-3a) were patterned along two normal directions as shown in Figure 3-3c. According to deformation pattern of metamaterial after buckling; four unit building cells were used as the representative volume element (RVE) as shown in Figure 3-3b.

In order to identify the desired buckling mode, FE simulations were performed on the existing cross lattice. The stability of these microstructures was evaluated using commercial FE software ABAQUS with standard solver (Simulia, Providence, RI) and a linear perturbation procedure was conducted to find the critical loads (eigenvalues) for different buckling modes (Eigenmodes). The numerical models were constructed with linear solid elements of the secondary accuracy (element C3D8 with a mesh sweeping seed size of 0.4 mm) as shown in Figure 3-3. It should be noted that the applied boundary conditions influenced the buckling modes of the finite-sized numerical model [7]. In this study, all degrees of freedom on top and bottom nodes of the numerical model were constrained except for the nodal movement of the top surface in the direction of the applied load.

A set of nonlinear post-buckling analyses under uniaxial compression was carried out using ABAQUS/Explicit to simulate the standard uniaxial compression on cross lattice and investigation of the deformation pattern of the structure under large deformation. It should be noted that the results of post-buckling analyses were affected by the effects of complex self-contact and inertia effect. Remarkably, the complex self-contact was an unavoidable factor in large deformation analysis. To overcome this obstacle, the explicit simulation was carried out with a prescribed velocity profile and interaction properties. Therefore, interaction properties were defined based on the surface to a surface algorithm which was penalty based. Also, the inertia effect was minimized by defining amplitude to apply the velocity on top of the FE model as it was used in reference [131] by using the equation 3-1. Where $\boldsymbol{d_{max}}$ was the maximum applied deformation, $\boldsymbol{T}$ was the total duration of the loading and **t** was

the variable of time. The velocity was applied gradually, and the acceleration at the beginning and ending of compression process was zero.

$$\vartheta(t) = \frac{\pi}{(\pi-2)}\frac{d_{max}}{T}\left(1 - \cos\left[\frac{\pi}{2T}t\right]\right) \quad (3\text{-}1)$$

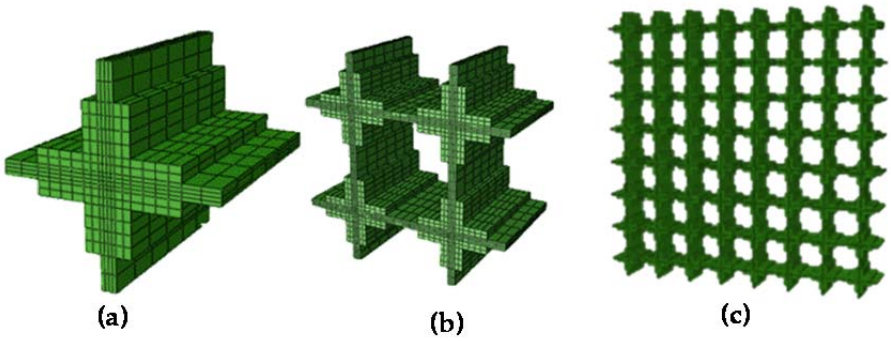

Figure 3-35 (a) Unit building cell of microstructure; (b) representative volume element; (c) designed bulk metamaterial with cross-shaped microstructures for experiments (T_A=0.8mm, T_B =2.4 mm, L_B=7.33mm).

3.1.3 Validation of FE model

An experimental specimen was fabricated and through the comparison of the deformation process between experiments and numerical model, the FE simulation was validated. The 3D printer was used to create a mold for casting liquid plastic as shown in Figure 3-4a and b. For the base foam, two liquid agents from Feguramed GmbH company was mixed.The weight ratio of the two liquid agents was 50:50 (Part A: Part B). The experimental fabricated model was shown in Figure 3-5.

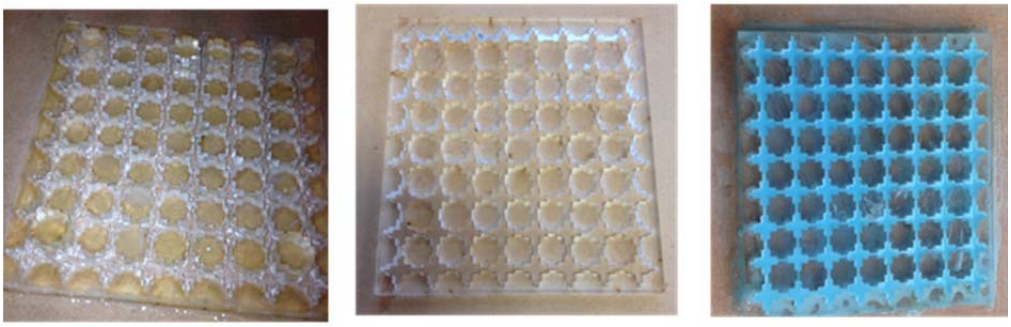

Figure 3-36 Casting process of liquid plastic base foam; (a) fabrication of 3D printed mold; (b) top view of 3D printed mold; (c) casting the liquid plastic base foam in the mold.

The performance of fabricated bulk material was tested under compression at a strain rate of $5x10^{-3}$ S^{-1}. The auxetic response of the 2D bulk metamaterial was recorded by two cameras from two

different directions and was presented in Figure 3-6 for the planar view. A comparison of the deformation process between experiments and numerical model revealed an excellent agreement between them. The FE simulations results with 3D elements were validated by comparing with experimental results as shown in Figure 3-6. Also, the FE simulations results with 3D elements were validated by comparing with experimental results as shown in Figure 3-9b. The difference between stress-strain curves in compression for numerical results and experiment was negligible, and agreement between them was clear.

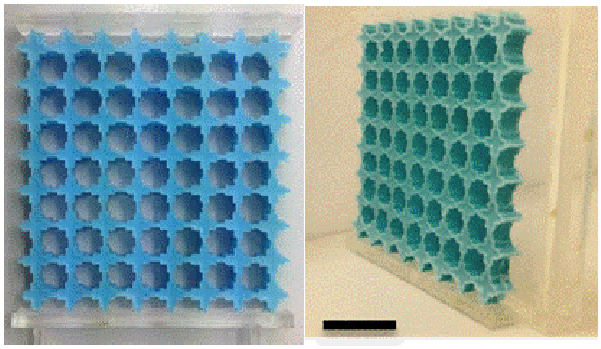

Figure3- 37 2D Experimental specimens from different perspectives. (height×width×depth: 92.8×88×10mm, Scale bar: 20 mm).

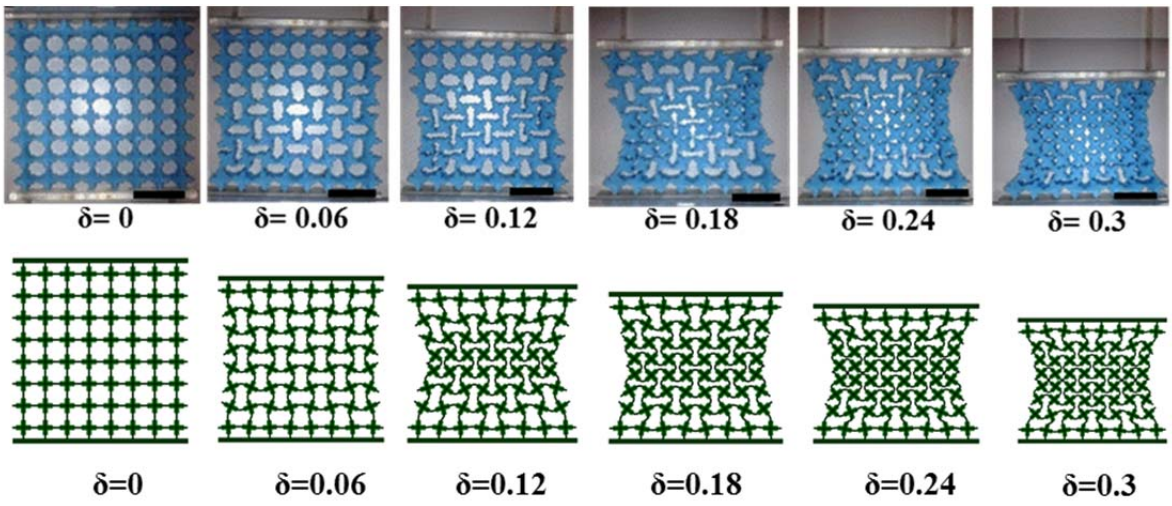

Figure 3-38 Comparison of deformation pattern of 2D auxetic metamaterial between FE results and experimental results. The upper row shows experimental results and lower row shows numerical results (Scale bar: 20 mm, strain rate: 5×10^{-3} S^{-1}).

3.1.4 Methodology

As mentioned before, the NPR behaviour of buckling-induced auxetic metamaterials was originated from the localized buckling mode shape [7]. So it is possible to predict the material failure due to buckling using linear perturbation analysis. The linear buckling analysis was employed to find the

bounds of the four defined geometric parameters as the effective range of auxetic behaviour. For this purpose, a linear algebraic equation for the unknown displacements was solved. $K\,\delta = F$, the strains and corresponding stresses which were obtained from this equation were compared to design stress (or strain) to predict an allowable range for stress (or strain). When the FE simulation revealed that the applied strain and corresponding stress exceeded the allowable range, it was assumed that material would buckle.

It should be noted that this instability usually occurred within the elastic range of the material. In such cases, it is worth to note that the buckling load was independent of the strength of a component the base material, however, the buckling load depended on the stiffness of the component. In other words, the buckling load depended on to the elastic instability of a component and was independent of the strength of this component. The lose of structural stiffness led to the buckling failure, and it was not governed by the usual linear FE simulation. However a FE eigenvalue (eigenvector equation), $|K + \lambda m\, KF|\ \delta m = 0$ was solved to calculate the multiplier or eigenvalues that scaled the magnitude of the load (up or down) to that required to cause buckling. Where λm is the buckling load factor (BLF) for the m^{th} mode, KF is the additional "geometric stiffness" due to the stresses caused by the loading F, and δm is the associated buckling displacement shape for the m^{th} mode. The microstructure of 2D lattice (See Figure 3-1) consisted of two parts with different thicknesses. As mentioned before, the localization of buckling at thinner walls of microstructure led to a rotation of thicker parts (Similar to rotation of rigid parts in the NPR mechanism of "auxetic behaviour from rotating of rigid squares"), and the hinges occurred at the middle thin links. So the desired buckling for NPR behaviour was similar to the mechanism with local buckling as shown in Figure 3-7 a, in contrast to the global buckling mode shape as shown in Figure 3-7 b and other non-symmetric mode shapes which led to non-auxetic behaviour.

A systematic study was carried out by varying the defined geometric parameters to find critical values for these parameters based on results of buckling analysis. The critical values were determined by the buckling analysis on our structure with 7x7 cells. Firstly it was supposed that the T_B was a constant value (for example T_B=0.1 T_A) then the values of L_A and T_A were decreased to half of its

previously used values (Respectively, L_A=0.5 L_B and T_A=0.5 L_A). It should be noted that the possibility of occurring of buckling for lower eigenvalues was more than other higher eigenvalues.

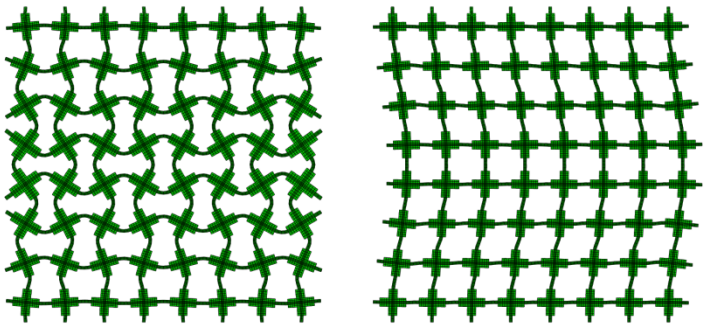

(**a**) (**b**)

Figure 3-39 Two different buckling mode shapes; (a) local buckling mode shape which led to auxetic behaviour; (b) global buckling mode shape which led to non-auxetic behaviour.

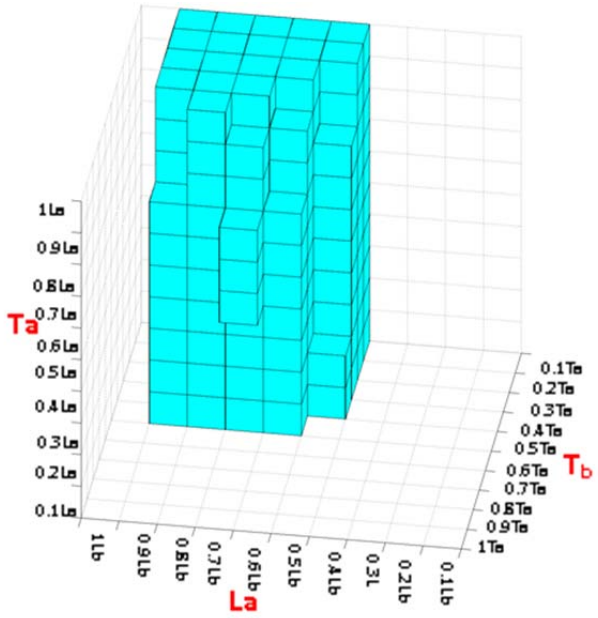

Figure 3-40 Geometric bound of three geometric parameters for auxetic behaviour identified by buckling analysis.

Therefore, the first buckling mode shape was checked whether it was similar to the local buckling pattern. If not, we decreased the values of L_A and T_A in a similar manner, and if it did, we increased L_A and T_A to the half values of the sum of the current value and its upper range bond.This procedure continued until the gap between two selected values was less than 10% of the current value.

It should be noted that when the geometric parameters exceeded the critical limits, the first buckling mode shape was changed from the local buckling to a global buckling. By using this method the corresponding limits were calculated and were represented by a surface in the space of the three geometric parameters as shown in Figure 3-8. There were obvious limitations on the bounds identified by buckling analysis because the auxetic behaviour only occured in an infinitesimal deformation range. For some cases, the auxetic materials within these bounds have little practical value for efficient usage in their intended application involving large deformation. The boundary conditions also influenced the results of buckling analysis. By changing the applied boundary conditions, the eigenvalues corresponding to different buckling mode shapes could be changed so it was possible that the first buckling mode shape was changed from the desired local buckling to global buckling mode shape. Also, it should be noted that for metamaterials undergoing large deformation, several possible configurations may happen and these configuration are corresponding to different buckling mode shapes. When the dispersion of eigenvalues of first three mode shapes is very low, it is possible that the deformation pattern of the metamaterial is changed from a specific configuration to another configuration corresponding to different buckling mode shapes. Here, inspired by these findings the investigation approach of NPR behaviour was developed from buckling analysis to post-buckling analysis and we focused on large deformation of the metamaterial to find the range of geometrical parameters for auxetic behaviour. It should be noted that the effects of shape, size and arrangement of void parts on the performance of cellular metamaterial were investigated by other researchers before. But to our knowledge, the effective strain range for auxetic behaviour has never been employed to find a geometric bound for auxetic behaviour. The starting point of this range was the critical strain at which buckling occurred and the metamaterial began to exhibit auxetic behaviour and the end point was the densification strain as presented in Figure 3-9. Beyond the densification strain, the cellular metamaterial was regarded as beingcompletely compacted. When the applied strain reached this value, the stress value increased sharply as shown in Figure 3-9b.

The energy efficiency method was employed to find the exact value of densification strain. In this method, firstly the absorbed energy was defined as the total area under the stress-strain curve.

Then, the energy efficiency parameter was found by dividing the absorbed energy by the stress itself, as shown below:

$$E(\varepsilon) = \frac{\int_0^{\varepsilon} \sigma(\varepsilon) d_{\varepsilon}}{\sigma} \qquad (3\text{-}2)$$

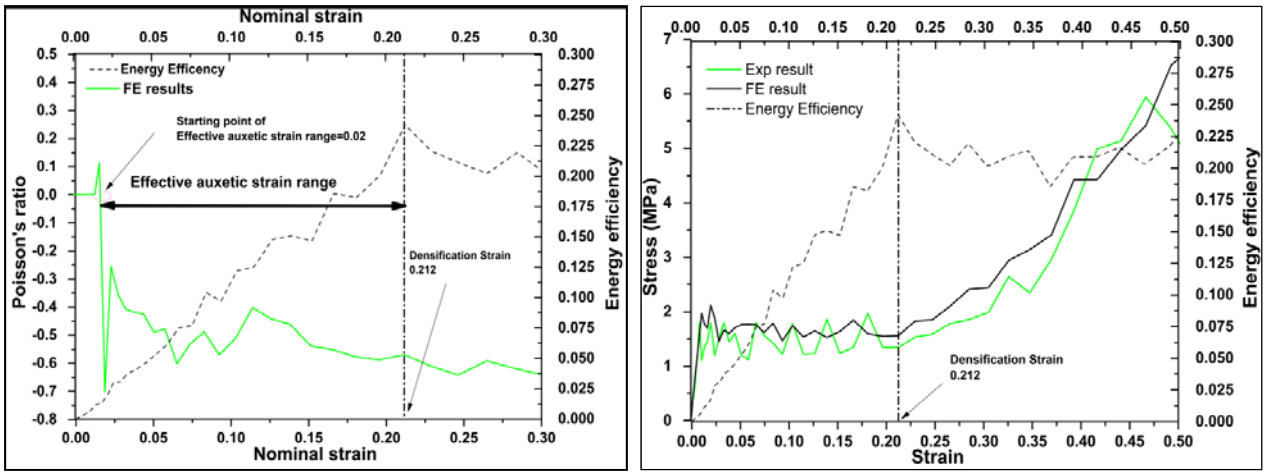

Figure 3-41 Clarification of energy efficiency method to define effective auxetic strain range; (a) illustration of upper bond and lower bond of effective strain range; (b) finding densification strain as the upper bound of effective auxetic strain range.

When the E(ε) reached the maximum point, the corresponding strain was the densification strain. The densification strain was marked by a dashed line in Figure 3-9a and b. It can be seen from this figure that the densification strains from the experimental data were similar to those from the FE results.

It was assumed that under large deformation, the metamaterial was considered as auxetic when the effective strain range was larger than a prescribed value, i.e. 0.05 or 0.1 which was determined by the intended applications. A systematic investigation was carried out by employing validated FE simulations, and the results were presented in Figure 3-10. A spatial region surrounded by a 3D surface has been illustrated in Figure 3-10a. Inside the defined region, the length of effective auxetic strain range was at least 0.05. The similar surface was obtained when the effective auxetic strain range was at least 0.1, and the results is presented in Figure 3-10b.

The comparison of geometric bounds based on linear buckling analysis in Figure 3-8 and the geometric bounds based on the post-buckling analysis in Figure 3-10 shows the lack of agreement

between them. The geometric bounds based on linear buckling analysis had the largest cover range and covered more microstructure designs than the other twos. Also the cover range of post buckling results with the effective strain range of 0,05 was larger than 0.1. Therefore, the results of our investigation revealed that the performance of a buckling-induced metamaterial under large deformation would not exhibit NPR behaviour when the geometric parameters used were within the bound identified by buckling analysis.

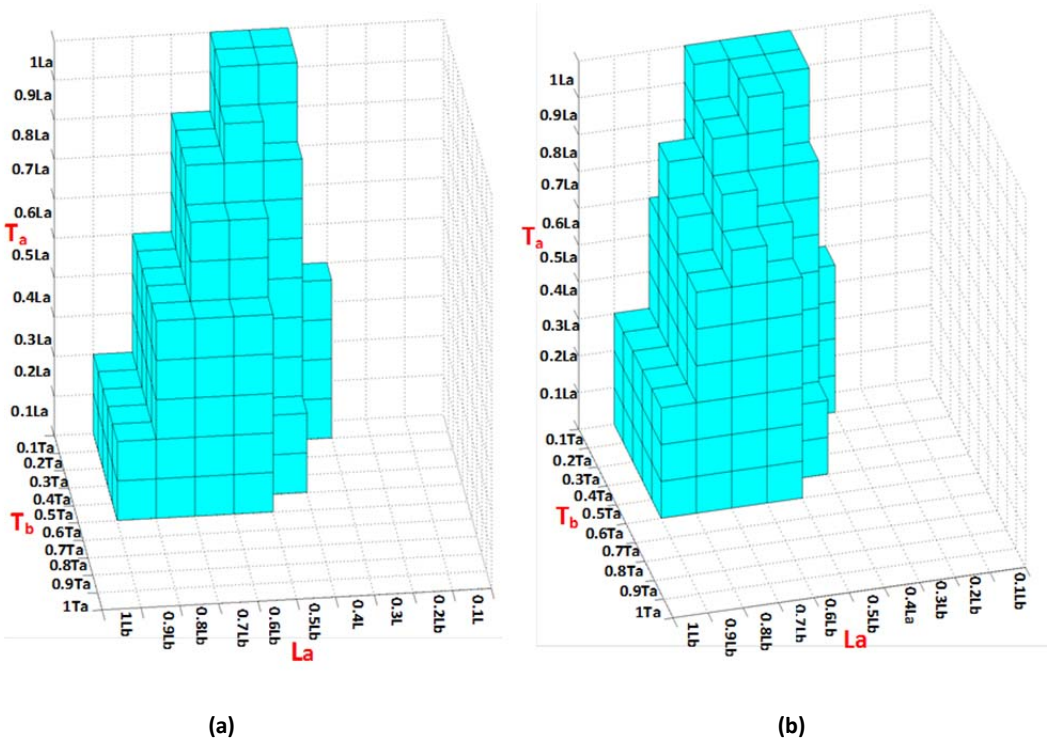

Figure 3-42 Geometric bound of three geometric parameters for auxetic behaviour under large deformation; (a) 3D surface for an effective strain range of 0.05; (b) 3D surface for the effective strain range of 0.1.

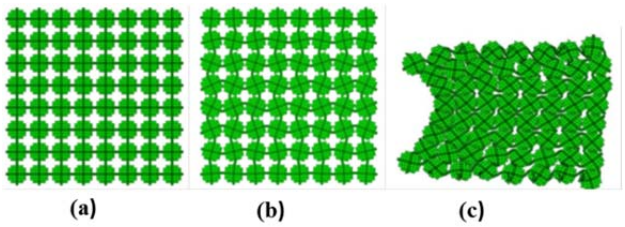

Figure 3-43 Comparison the large deformation analysis result and linear buckling analysis; (a) unreformed metamaterial; (b) First buckling mode shape; (c) Observed deformation pattern under large deformation (strain=0.33).

As an example, the observed deformation under large deformation and the first linear buckling mode shape of a metamaterial with specific geometrical features (TB=0.2TA, LA=0.8LB, and TA=0.7LA) were presented in Figure 3-11. In this case the first buckling mode shape is exactly

similar to local buckling pattern for auxetic behaviour; however, the result of large deformation analysis revealed that the exhibited deformation pattern was similar to a global buckling without auxetic behaviour.

3.1.5 A brief summary of conclusions for this section

- A new bound theory was explored to investigate the geometric range of pore size of microstructure of 2D auxetic metamaterials within which the designed metamaterial exhibited the buckling triggered auxetic behaviour. Under large deformation, the effective strain range for NPR was bounded by the buckling strain and the densification strain. The energy efficiency method was used to identify the densification strain. The following conclusions can be drawn from the results mentioned in this section: The bound identified by linear buckling analysis may not be a reliable to designing the auxetic metamaterials under large deformation;
- A more reliable geometric bound was identified from this study and it can be used more effectively to design an auxetic metamaterial for those applications which require an auxetic behaviour occurring in a strain range larger than 0.05.
- The geometric bound was represented by a graphic method which could be used easily by other engineers designing auxetic metamaterials for a specific application.

It is also worth noting two limitations of the present study. Firstly, the proposed method required a massive computational effort compared to buckling method to obtain a geometric bound for auxetic behaviour. Secondly, the proposed method was only applicable to buckling-induced auxetic behaviour and it may not be applicable to predict the auxetic geometric bound for other types of auxetic metamaterials.

3.2 Investigation of the influence of base material properties on buckling pattern

For many base materials, Young's modulus is a constant value over a range of strains. Such materials are called linear and are said to obey Hooke's law. Examples of linear materials include Rubber and soil (except at very low strains).

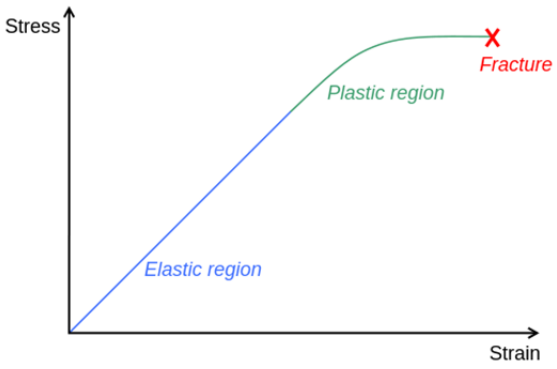

Figure 3-44 Stress-strain curve for nonlinear materials.

In contrast, for nonlinear materials (such as steel, carbon fibre, glass, brass, and aluminum) after the yield strength, the material enters the plastic deformation region, which means that the deformation of the material is permanent. In the plastic region, the loading modulus is slowly decreased, the stress-strain curve enters a plateau region instead of the original curve of the elastic region as shown in Figure 3-12. And there is a permanent extension when all stress is removed. Differences in the shape and limits of the stress-strain diagram determine whether a material is considered ductile or brittle, elastic or plastic.

The main aim in this part of the study is to investigate the influence of base material properties on buckling patterns of the initial 2D metamaterial with origin geometry. In this way, the raw aluminum was used as the bass material to construct a 2D metallic metamaterial through manual techniques in the workshop because of its excellent ductility. The geometry of the design is within the bounds indentified with a effective auxtic strain of 0,1 in Section 3.1. In other words, in this way the manufactured aluminium cellular material should exhibits NPR in a strain range of 0.1.

3.2.1 Fabrication of aluminium specimen for experiments

An aluminium specimen was fabricated using manual techniques in the workshop. It should be noted that the NPR property was independent of boundary conditions also it was scale-independent. Therefore, the geometrical configuration of this new metallic specimen was exactly similar to the pervious 2d rubber specimen in section 3.1.3 however the dimensions of rubber model were changed by the scale factor of 1: 5.681 to fabricate the new metallic specimen. The aluminum specimen was fabricated by using the aluminum sheets with the exact thickness of 0.5 mm. Sixteen columns were

cut from aluminum sheets that the width of each column was 56 mm and the height was 500 mm as shown in Figure 3-13a.

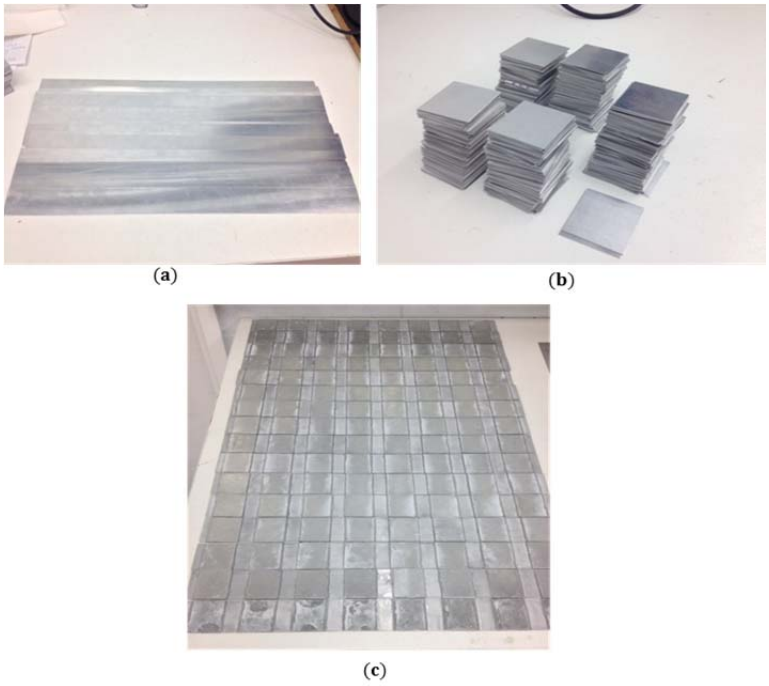

Figure 3-45 Fabrication process of aluminium experimental model; (a) aluminium column with the dimensions of height×width: 500×40mm; (b) aluminum squares with the dimensions of height×width: 31.25×31.25mm; (c) aluminum squares were bonded to with the dimensions of height×width: 31.25×31.25mm.

As mentioned before the microstructure of 2D buckling-induced structure consists of two different parts with different thicknesses. In order to create thicker parts of microstructure, 512 aluminum squares were cut from the sheets (see Figure 3-13b) and they were bonded on top and bottom of the interior joint points of lattice columns by using Loctite® Super Glue Liquid Professional as shown in Figure 3-13c. In order to assembling the aluminum columns together, several slots were created at the interior joint points of lattice columns, and then the aluminum columns were assembled together. The super glue was used to fix them perfectly. Figure 3-14 clearly presents the manufacture process of aluminum lattice specimen.

The 2D periodic aluminum bulk metamaterials for original buckling-induced design is shown in Figure 3-14 d. The dimensions of the experimental specimen was height × width × depth = 500×500 ×56 mm. Two plates were added to top and bottom of the experimental specimen to constrain the degrees of freedom of the top and bottom nodes' surfaces except for a degree of freedom in the direction of

load. In order to find the mechanical properties of aluminium alloy, 10 dog bones specimens were cut from aluminium sheets by using laser cutting machine.

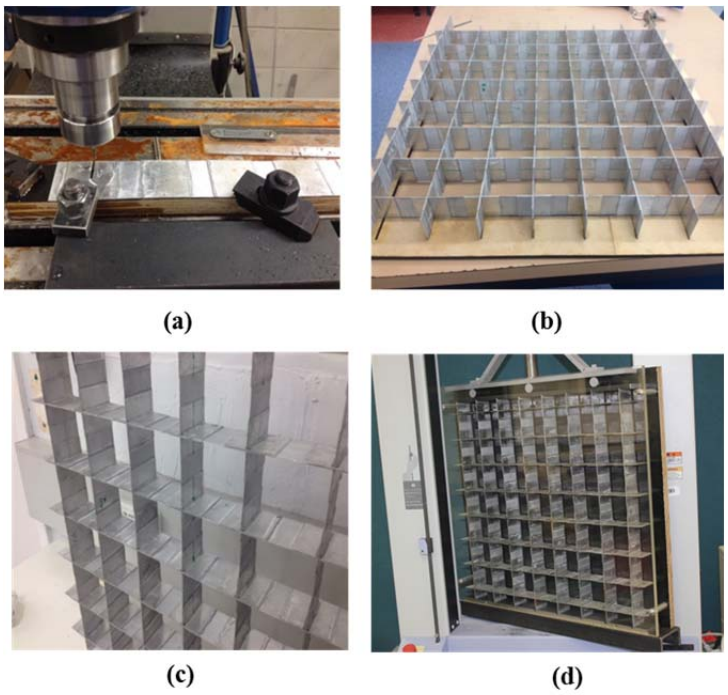

Figure 3-46 Fabrication process of aluminium experimental model; (a) creating several slots at the interior joint points of lattice columns; (b) assembling lattice columns at the interior joint points of lattice; (c) perspective view of the aluminium experimental specimens ; (d) Quasi-static uniaxial compression tests under compression by Shimadzu machine (PSF=0%, height×width×depth: 500 mm ×500 mm×56mm).

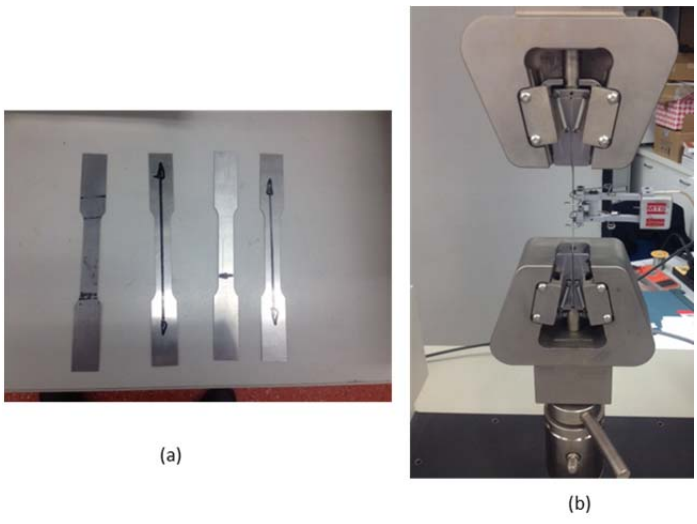

Figure 3-47 Tensile test of aluminium dog-bone specimens using MTS machine; (a) Front view of aluminium dog-bone specimens; (b) MTS machine.

The size of these specimens was chosen based on ASTM B557-M (American Standard Test Material). According to this standard, two types of dog bone specimens were fabricated for tensile

test. The first type of dog bone specimens were cut parallel to the direction of rolling of the aluminium sheet and the second type of dog bone specimen were cut orthogonal to the direction of rolling of the aluminium sheet as shown in Figure 3-15a. The material properties of the aluminium alloy were measured through the standard tensile test of 10 dog bones with same configuration using an MTS machine (MTS Company, Eden Prairie, MN, USA), which is shown in Figure 3-15 b.

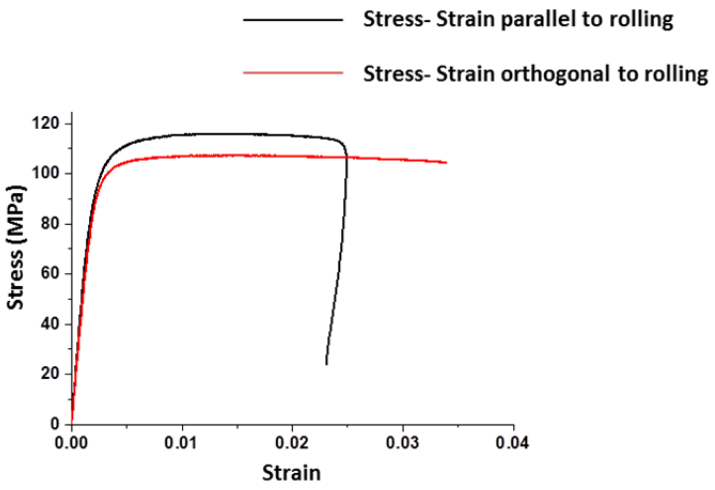

Figure3- 48 The results of tensile test on two types of aluminium dog-bone samples.

The tensile process stopped at a true strain of ε= 0.024 and ε= 0.03164. The results indicated that the constitutive behaviour could be accurately represented by an elastic–perfectly plastic model as shown in Figure 3-16. It should be noted that the dog bone specimens exhibited slightly anisotropic behaviour. The Young's modulus along the rolling and orthogonal rolling was 52±.06 GPa. The yield stress for specimens along rolling direction was 112.48 Mpa and orthogonal to the rolling direction was 102.68 Mpa.

3.2.2 Comparison of the deformation pattern of rubber and metallic (aluminium) metamaterials with initial same geometric design

The performance of the new metallic specimen with buckling-induced designed was tasted under standard uniaxial compression test similar to the normal compression test of other cellular materials [7]. The Quasi-static uniaxial compression test was conducted by a Shimadzu machine (Shimadzu Company, Kyoto, Japan) at a fixed strain rate of 5×10^{-3} s^{-1}. The deformation process was captured by two cameras and the result of this compression test is presented in Figure 3-17.

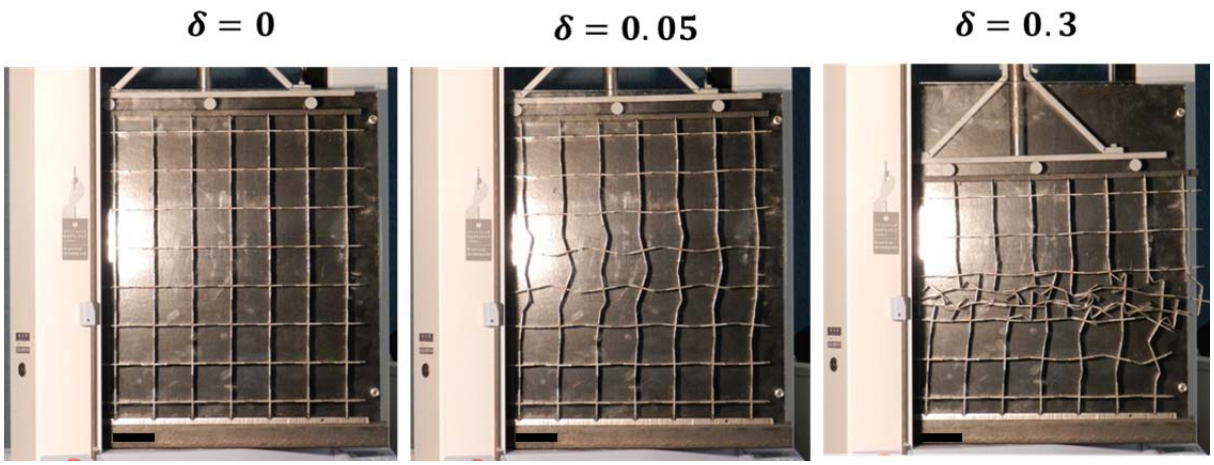

Figure3- 49 Deformation pattern of the experimental 2D aluminium metamaterial with buckling induced design; (Scale bar= 71.5mm, strain rate: 5×10^{-3} S^{-1}).

Surprisingly, the transformation pattern of the 2D metallic specimen was in the stark contrast with the deformation pattern of 2D elastomeric specimen that was manufactured using silicon-based rubber. As discussed in the previous part of this chapter, the elastic auxetic specimen was made using an elastomer (silicone rubber) and the NPR behaviour was observed consistently in both laboratory experiments and FE analysis. Indeed the rubber model exhibited the auxetic behaviour which originated from localized buckling mode. In contrast, the 2D metallic specimen displayed the non-auxetic behaviour under compression despite the fact both models had the same topology. So it was found that the NPR behaviour disappeared. This peculiar phenomenon was illustrated in sharp contrast in Figure 3-18. From both experimental observations and FEA simulation, it is noted that the plastic strain localisation of the base materials was a dominant factor affecting the final deformation pattern. When the metallic base material at the weak links yielded and underwent plastic deformation before the buckling of the overall bulk material, the sharp decrease of Young's modulus of metallic base material (69GPa for aluminium) to plastic hardening modulus caused that the massive plastic deformation occurred in a localized region to form a crushing layer. The deformation intended to concentrate in this layer until the large geometry changed or inner contact of the members in the building cell provided more resistance to the strain localization.

It should be noted that the initiation of the deformation pattern of the designed metamaterial was sensitive to the initial imperfection in the original geometry of the periodic microstructures. As a

result, there were two ways to restore the NPR behaviour for this design. One was to increase the plastic hardening modulus of the base material to a level close to its elastic modulus. This was inapplicable to most of metallic materials. The other approach, whichwas advocated in the presented study, was to alter the initial geometry of the RVE with an "imperfection" large enough to set the deformation of the metamaterial to a certain pattern with NPR behaviour.

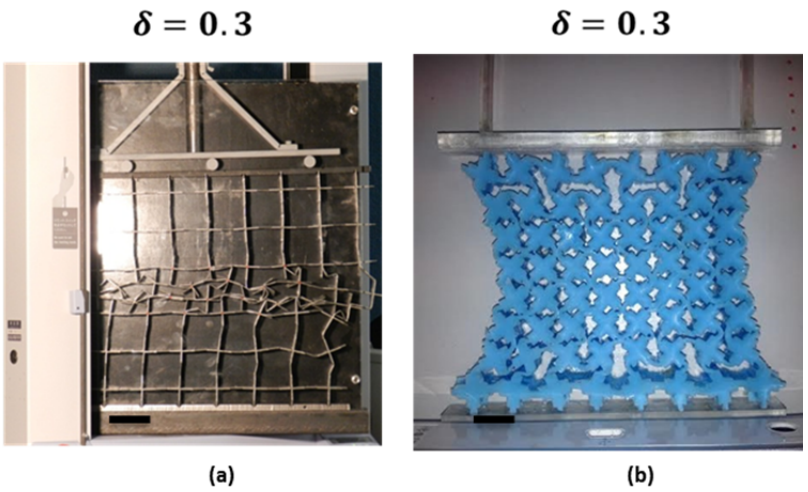

Figure 3-50 Comparison of the deformation pattern of aluminium and rubber specimens; (a) Non-auxetic behaviour of aluminium specimen (scale bar=71 mm); (b) auxetic behaviour of rubber specimen (scale bar=20 mm).

3.2.3 Brief summary of conclusions from this section

In this section, a 2D aluminium buckling-induced auxetic metamaterial was used to study the deformation pattern of metamaterial undergoing large plastic deformation. It was confirmed that the loss of buckling-induced NPR behaviour would occur in metamaterial with metallic periodic cells undergoing plastic deformation. We concluded from the results of this section:

- When the base material deformed in its elastic range, this planar metamaterial behaved in a similar manner to the 2D buckling-induced auxetic metamaterials with auxetic behavior.
- When the deformation of base material entered into plastic range, the loss of buckling-induced NPR behaviour occurred.
- We attributed the loss of buckling-induced NPR to the localization of plastic strain for designed buckling-induced auxetic metamaterials.

3.3 Development a general approach for designing metallic auxetic metamaterials from regular periodic microstructure deformation

The loss of negative Poisson ratio (NPR) behaviour in Section 3.2 led us to propose a new approach to designing metallic metamaterials with NPR under large plastic deformation. A 2D auxetic metamaterial was derived from a regular square lattice to confirm and investigate these new features further in this section. The design approach was developed from previous works on buckling-induced elastic auxetic metamaterials. By altering the initial geometry of microstructure with the desired buckling pattern, the 2D metallic metamaterials exhibit NPR behaviour with tunable mechanical properties. Both experiments and finite element simulations were used to verify the effectiveness of the new approach. A systematic parametric study using the validated finite element models was conducted to reveal the novel features of metallic auxetic metamaterials undergoing large plastic deformation. Detailed description of the following sections will provide a useful guideline for the design of 2D metallic auxetic metamaterials for various applications.

3.3.1 Methodology

In order to obtain a novel class of 2D metallic auxetic metamaterials with the potential to retain tuneable auxetic behaviour under a wide range of applied strains, a general systematic approach was developed. This general approach led to the possibility of tuning the auxetic behaviour and mechanical properties for the targeted applications. The key idea of this methodology was the exploitation of a pattern from the linear buckling analysis to create microstructures of metamaterials with an auxetic response. This methodology could be divided into four steps as described in the following sections. Moreover, the magnitude of alteration of microstructure and plastic properties of the base material were studied as the primary key factors in tuning the performance of 2D metallic auxetic metamaterial. These details are presented in the following sections.

3.3.1.1 Initial geometric design of microstructures modified from a regular pattern

The auxetic performance of a metamaterial was determined by the geometrical features and deformation mechanisms of its microstructure. According to the geometry of microstructure of metamaterials that exhibited auxetic behaviour induced by elastic instability, the ribs of their building

cell were slightly thicker in the proximity of their connecting points than the middle parts of the ribs. Consequently, rotation occurred at the middle parts of these ribs in clockwise and counter-clockwise directions, to form a deformation mechanism after the buckling of the ribs. These observations and mechanisms led us to think that buckling-induced auxetic cellular metamaterials could be produced from a conventional regular cellular lattice through geometrical modification of their microstructures.

In this research the microstructure of a new buckling-induced 2D auxetic metamaterial was produced from an existing conventional regular lattice through the proposed modification. This method consisted of moving a small portion of the middle part of their ribs to the proximity of the connecting joints. This geometrical modification on the microstructure was based on the hypothesis that, under deformation, joints behaved as "rigid joints" and rotated relatively to each other after the ribs buckled. The geometric modification of the unit cell of the regular lattice through the proposed method is illustrated in Figure 3-19 b and c. The new buckling-induced 2D auxetic metamaterial was similar to the buckling-induced auxetic metamaterials investigated by Mullin et al. [103]. According to the buckling pattern, RVE contained four unit cells as shown in Figure 3-19 d. Similar to the designing approach of elastic metamaterials, the bulk 2D metamaterial was constructed by replicating RVEs along two planar directions , as shown in Figure 3-19 e.

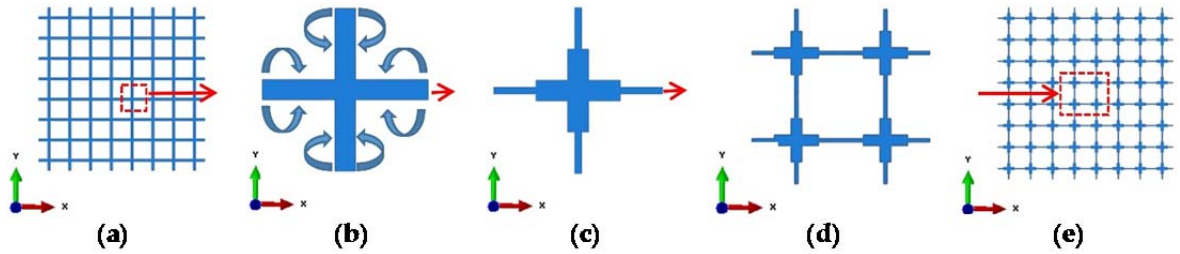

Figure3- 51 Modification of a regular pattern to form a new buckling-induced 2D auxetic metamaterial ;(a) Conventional regular lattice; (b) building unit cell of initial regular lattice; (c) modified unit building cell of microstructure; (d) representative volume element; (e) designed bulk metamaterial with cross-shaped microstructures for experiments.

3.3.1.2 Investigation of the instability of initial 2D auxetic metamaterial using a linear perturbation procedure

The elastic instability in elastomeric metamaterials triggered a pattern switching phenomenon above a critical load, which led to auxetic behaviour under compression. In order to identify the desired buckling mode, FE analysis was performed on the existing cross lattice and the modified periodic

cellular metamaterial. The stability of these microstructures was evaluated using commercial FE software ABAQUS with standard solver (Simulia, Providence, RI, USA) and a linear perturbation procedure was conducted to find the critical loads (eigenvalues) for different buckling modes (Eigen modes). The numerical models were constructed with linear solid elements of the secondary accuracy (element C3D8 with a mesh sweeping seed size of 0.4 mm). It should be noted that the applied boundary conditions influence the buckling modes of the finite sized numerical model. In this study, all degrees of freedom on the top and bottom nodes of the numerical model were constrained except for the nodal movement of the top surface in the direction of the applied load. The analysis was carried out to simulate the standard uniaxial compression. It is worth noting that for purely elastic models the buckling modes were independent of the modulus of elasticity; thus any value of modulus could be used to conduct the buckling analysis. Therefore, the proposed design approach was independent of the influences of the elastic base material. The Young's modulus of elasticity and Poisson's ratio of brass was used as the properties of the base material in numerical simulations.

3.3.1.3 Identification of the desired buckling pattern from an elastic instability analysis

As mentioned before, the linear buckling analysis yields a number of eigenvalues and buckling mode eigenvectors corresponding to these eigenvalues. Normally the lowest eigenvalue with the corresponding buckling mode is of interest because the buckling modes with higher eigenvalues are difficult to trigger under quasi-static loading. The desired buckling modes (which may not always be the first mode for the buckling analysis), termed alternating periodic buckling mode, were identified through the deformation features of buckling-induced auxetic metamaterials previously investigated. In most cases, the auxetic behaviour of this type of metamaterials was featured by such a mode with alternating mutually orthogonal ellipses. According to this identified principle, the seventh mode shape of initial metamaterial (regular conventional lattice) is similar to the observed buckling pattern that leads to the auxetic behaviour. In contrast, the first buckling mode shape of the newly designed metamaterial (with the lowest eigenvalue) can be adopted as the desired buckling mode shape.

3.3.1.4 Design of new metamaterials through superposition of desired buckling mode

The result of our study on designing elastic buckling-induced auxetic metamaterials (in section 3.2.2) revealed that altering the initial geometry of the microstructure was a way to trigger the deformation to a specific pattern that led to auxetic behaviour .One set of the output of the buckling analysis was a number of non-dimensional buckling modes. Thus, in order to define the magnitude of alteration of microstructure, a scale factor is required. In this study, the pattern scale factor (PSF) was proposed to add the desired buckling mode shape to the initial geometry of the metamaterial. To quantify the magnitude of the alternation, the PSF was determined using the special geometric feature of an RVE of the microstructure initially designed. The innermost RVE of the bulk metamaterial was selected to quantify the PSF. The final microstructures for metallic auxetic metamaterials were obtained by adding the desired mode shape multiplied by the specified design scale factor (DSF) to the original coordinates. DSF is an independent factor that consists of scaling the maximum displacement amplitude to visualize a deformed shape. When the walls at the center of the RVE touched each other, the corresponding DSF (in this case 0.0092) was defined as PSF = 100%, as shown in Figure 3-20c.

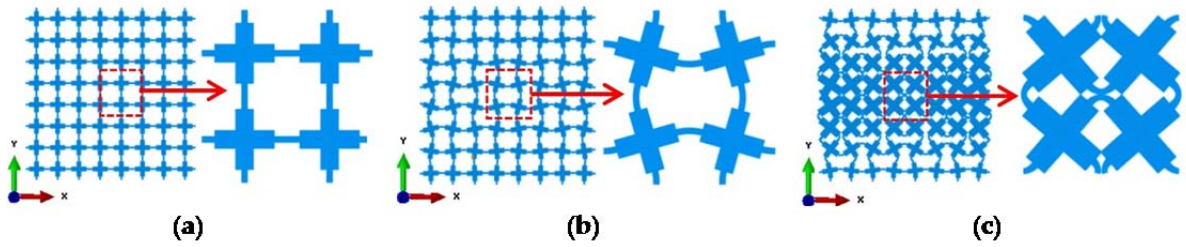

Figure 3-52 Definition of PSF to alter the initial microstructure of a buckling-induced metamaterial; the normalized desired buckling mode shapes scaled by different corresponding DSFs and their most central RVEs; (a) PSF = 0, DSF = 0; (b) PSF = 20%, DSF = 0.00184; (c) PSF = 100%, DSF = 0.0092.

Other magnitudes of PSF were defined accordingly as 0% and 20%, corresponding to DSFs of 0 and 0.00184, respectively. The normalized desired buckling mode and its innermost RVE with different PSFs are presented in Figure 3-20. Through changing the PSF, a new class of auxetic metamaterials with different auxetic performance was produced. The tuneable auxetic performance was a special feature of this class of auxetic metamaterials and potentially could be implemented in particular applications with a specific negative value of Poisson's ratio. It should be noted that, without this alternation, the deformation of this type of auxetic metamaterial was not uniform at the beginning stage under compression, which exhibited a positive Poisson's ratio (see Figure 3-17) until

buckling occurred. It should be mentioned that in another study by Shen et al. [7] on designing buckling induced auxetic metamaterials, the desired buckling mode of the bulk metamaterial was superposed to the original designed microstructures of metamaterial. It resulted in a non-periodic microstructure. The periodicity was achieved by patterning the altered central RVE of the bulk metamaterial in this study. The altered bulk metamaterial was formed by repeating this altered RVE as the unit cell.

3.3.2 Experiments

3.3.2.1 Fabrication of 2D metamaterials for experiments

The metallic specimens were fabricated using a casting method combined with a high-resolution 3D printing technique. In the first step, the metamaterial was printed in wax then the wax model was put inside liquid plaster. The wax was used as a supporting material to make a plaster mold. After setting the plaster, it was placed in an industrial oven to melt out the wax. Eventually, the molten metal was poured into the plaster mold and was placed at the fixed position to become solid.

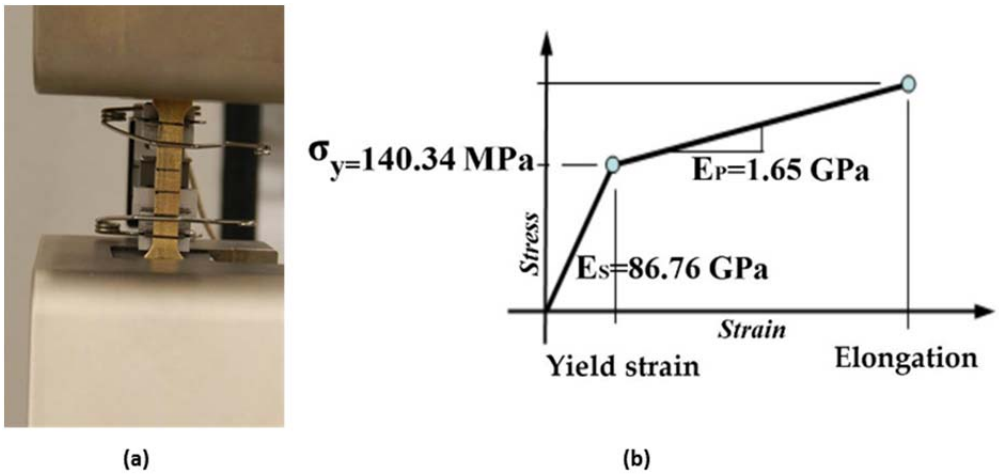

Figure 3-53 Tensile test of 3D printed brass dog-bone using MTS machine. (a) Front view of brass dog-bone. (b) Schematic curve of stress-strain for brass

Table 3-1 Material properties of brass.

Modulus of Elasticity (GPa)	Yield Stress (MPa)	Strain Hardening Modulus (GPa)	Density (GPa)
86.76	140.34	1.65	8720

Raw brass was selected as a representative base material of printed specimens because of its excellent ductility among available materials for 3D printing. The mechanical properties of brass were

obtained directly from a standard tensile test on six dog-bone specimens using an MTS (material test system) machine (MTS Company, Eden Prairie, MN, USA), which is shown in Figure 3-21. The average mechanical properties of brass tests were summarized in Table 3-1. The influence of the anisotropy of base material was not studied here. This anisotropy may be caused by the inevitable inclusion of air bubbles into brass specimens during the manufacturing process. The penetration of tiny bubbles causes very small holes inside the specimens and changes the mechanical properties and density of different printed specimens. However, the excellent agreements between the numerical and experimental results revealed that the influence of potential anisotropy was negligible in this study.

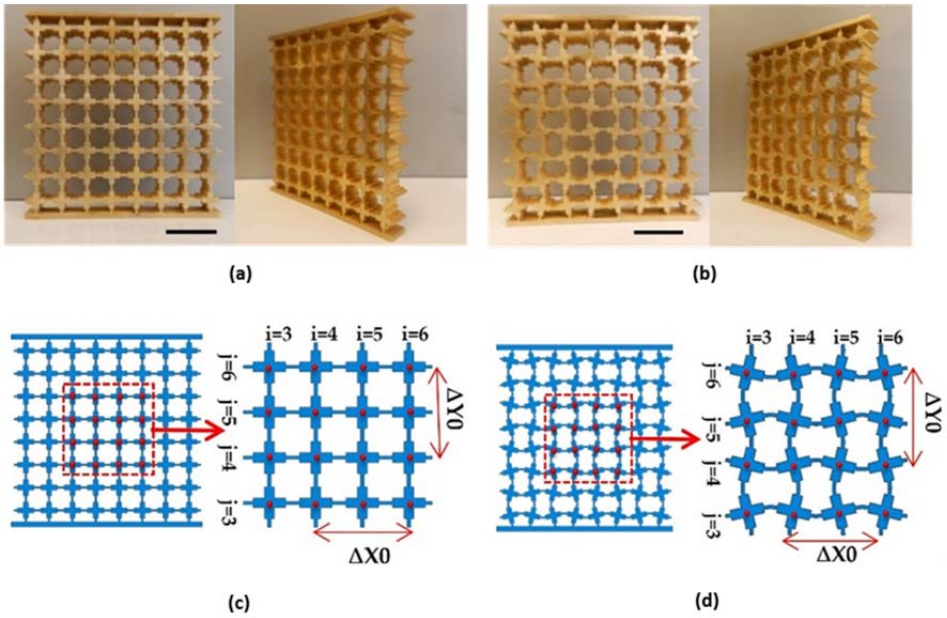

Figure 3-54 The final design of metamaterial employed for FEA and experimental investigation; (a) Front view and perspective view of buckling-induced metamaterial (PSF = 0%; density: 2798.05 kg m^{-3}, overall mass: 228.5 g, mass error: 1.08%, height × width × depth: 92.8 mm × 88 mm × 10 mm, Scale bar: 20 mm); (b) front view and perspective view of the metamaterial with altered geometry (PSF = 20%, overall mass: 222.57 g, density: 2725.43 kg m^{-3}, mass error: 2.06%, height × width × depth: 92.8 mm × 88 mm × 10 mm, Scale bar: 20 mm); (c) schematic diagram of central region with 16 nodes (PSF = 0%); (d) schematic diagram of central region with 16 nodes (PSF = 20%). The image processing was used to measure the horizontal and vertical center-to-center distances of nodes.

The 2D periodic bulk metamaterials for original buckling-induced design (PSF of 0%) and for an altered one with unit cells with a PSF of 20% are shown in Figure 3-22. The first 3D printed brass specimen was a buckling-induced metamaterial with PSF = 0, as shown in Figure 3-22a, and the other is the altered one that was superposed by the desired buckling mode with a PSF of 20%, is shown in Figure 3-22b. The dimensions of the first and second test specimens were height × width × depth =

92.8 mm × 88 mm × 10 mm. Two plates were added to the bulk materials to constrain the degrees of freedom of the top and bottom nodes' surfaces except for a degree of freedom in the direction of load.

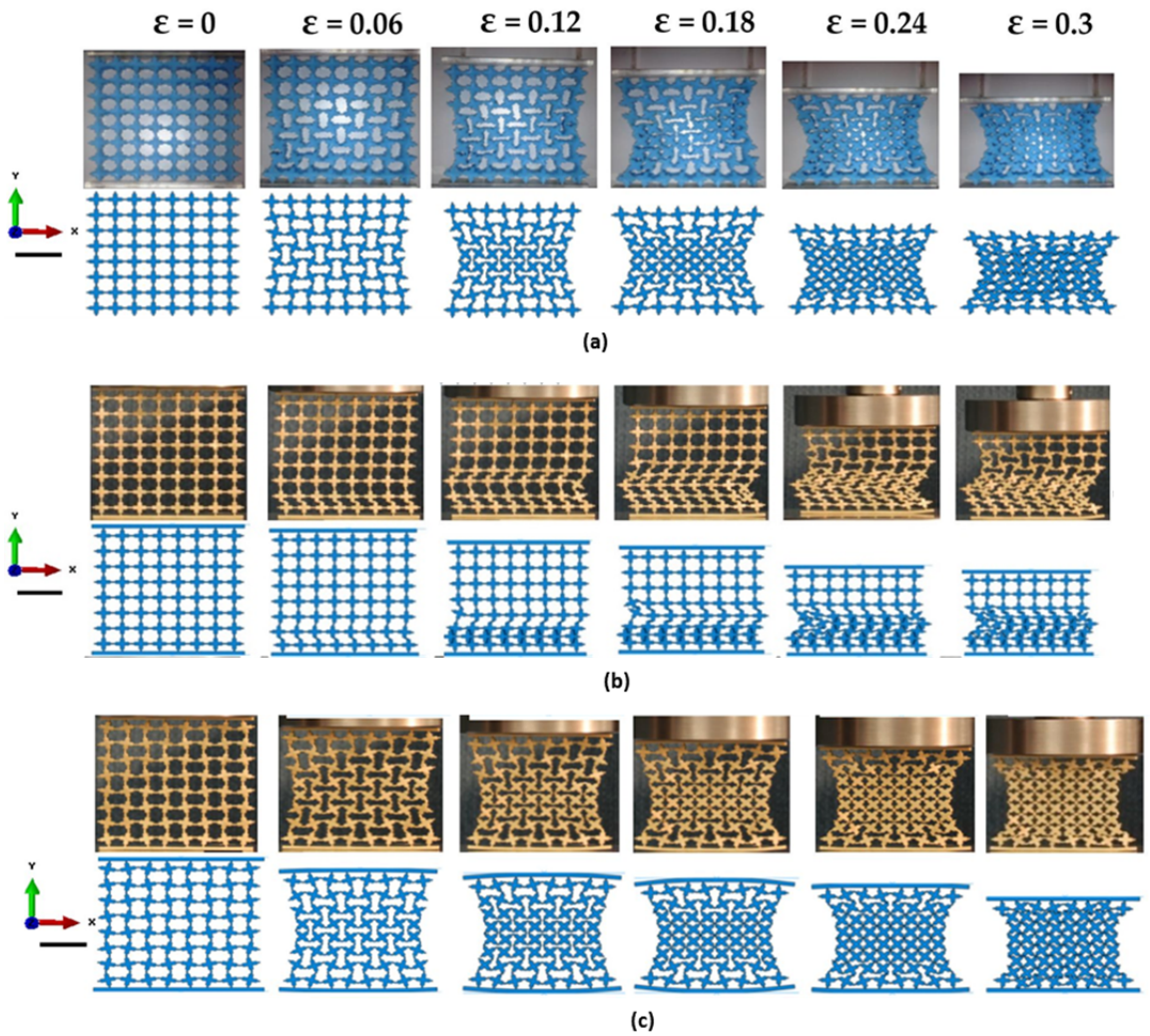

Figure 3-55 Comparison of deformation patterns of three new designed metamaterials between numerical and experimental results; (a) Experimental and numerical results of initial design of auxetic elastic metamaterial (rubber) with PSF = 0%; (b) experimental and numerical results of initial design of metallic metamaterial with PSF = 0%; (c) experimental and numerical results of the new design of auxetic metallic metamaterial with PSF = 20% (Scale bar: 20 mm, load direction Y, strain rate: $5 \times 10^{-3}\ s^{-1}$).

To check the accuracy of the manufactured samples, the weights of printed models were measured and compared with the weight of our initial design obtained from the numerical mode. The weights of printed samples were slightly heavier than the designed ones. A numerical comparison of models with the different weight obtained by changing the void of RVE confirmed that these small weight differences were negligible. In order to compare the deformation patterns of rubber and metallic metamaterials with initial geometric design (PSF= 0%), a 2D elastomeric specimen was

manufactured using silicon-based rubber as shown in the top-most row of Figure 3-23. The material properties of silicon-based rubber (Tango plus) were measured in the previous section 3.2.1.

3.3.2.2 Experimental setup for uniaxial compression testing of 2D metallic metamaterials

Quasi-static uniaxial compression tests were carried out to investigate the performance of 2D metallic auxetic metamaterials under compression. The tensile tests were conducted by a Shimadzu machine (Shimadzu Company, Kyoto, Japan) at a fixed strain rate of 5×10^{-3} s^{-1}. The deformation process was captured by two cameras. The first camera was used to capture photos in the lateral direction of our 2D test specimens every 30 s. The second camera was employed to record a performance video of the test process. The nonlinear response of metamaterials was considered to be in the range of effective auxetic strain. In other words, the focus of this research was on the behaviour of metamaterials, whereas the value of nominal applied strain was below the densification strain. Densification strain was defined as the maximum value of applied strain that satisfies the condition of maximum energy efficiency, as used by Shen et al. [132]. The experimental value of Poisson's ratio was calculated through image processing from the nodes in the central parts of ligaments, as shown in Figure 3-22 c and d. Indeed, at a specific value of nominal strain, the $(x_{i,j}, y_{i,j})$ coordinates of the centroid point of each unit cell were determined. The row and column indices were represented by $1 \ll i \ll 8$ and $1 \ll j \ll 8$, respectively. The central area under consideration consisted of 16 nodes; these were designated with a red dashed line indicating $3 \ll i \ll 6$ and $3 \ll j \ll 6$, as shown in Figure 3-22 c and d. The horizontal and vertical centroid-to-centroid distances were calculated by using coordinates $(x_{i,j}, y_{i,j})$, $\Delta x_{i,j} = x_{i+1,j} - x_{i-1,j}$ and $\Delta y_{i,j} = y_{i,j+1} - y_{i,j-1}$. Also, the center to center distances between the points of undeformed unit cells before compression were defined by $\Delta x(0)=\Delta y(0)=11$ mm. Equation 3-2 was employed to calculate the local values of the engineering strain Poisson's ratio.

$$\boldsymbol{\upsilon_{i,j}} = -\frac{\frac{\Delta \boldsymbol{X_{i,j}}}{\Delta \boldsymbol{x(0)}}}{\frac{\Delta \boldsymbol{Y_{i,j}}}{\Delta \boldsymbol{y(0)}}} \tag{3-3}$$

Eventually, four values of Poisson's ratio were calculated from the central nodes under consideration, and the average of them was computed at each specific value of nominal strain.

3.3.2.3 Experimental results

As expected, the deformation pattern of a brass metamaterial undergoing plastic flow was different from that of a rubber sample with only elastic deformation. When the base material was changed to metal, the auxetic behaviour disappeared, and a new non-auxetic pattern similar to the global buckling pattern for elastic bulk materials was observed, as shown in Figure 3-23b. This pattern usually yielded a zero or positive Poisson's ratio. In contrast, the test specimen with altered microstructures (PSF = 20%) exhibited obvious auxetic behaviour, as shown in Figure 3-23c. It developed from a localized buckling pattern and was similar to mutual ellipses with long orthogonal axes. The results for all samples are presented in Figure 3-23 as a function of nominal strain.

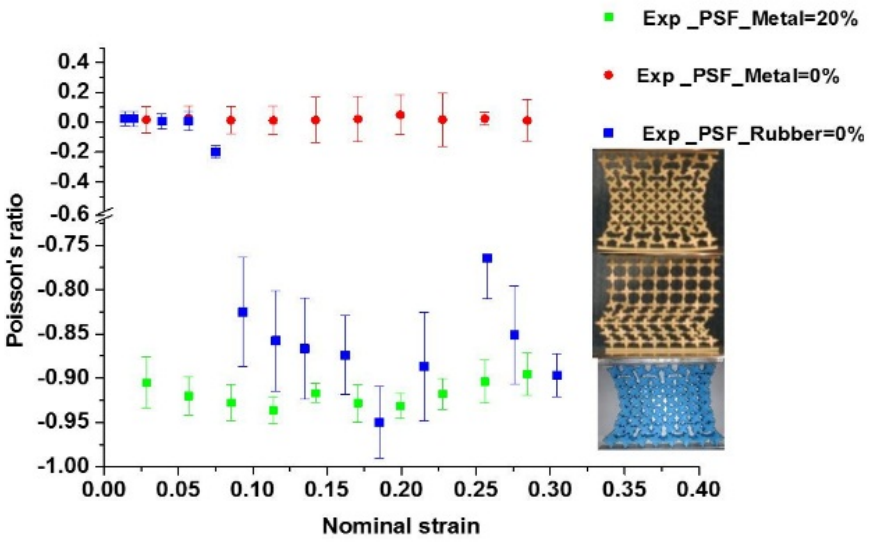

Figure 3-56 Comparison of auxetic and non-auxetic behaviour of new design of auxetic metallic metamaterial with PSF = 20%, initial design of metallic metamaterial with PSF = 0 and initial design of auxetic elastic metamaterial (rubber) with PSF = 0% (Scale bar: 20 mm, load direction Y, strain rate: 5×10^{-3} S^{-1}).

These experimental results revealed the significant influence of base materials with nonlinear properties or metal plasticity on the auxetic behaviour of the buckling-induced auxetic materials. They also proved the effectiveness of designing the metallic auxetic metamaterials using a buckling mode to alter the initial geometry of buckling-induced metamaterials. By applying different values of PSF, a family of metallic metamaterials were generated, which exhibited obvious auxetic behaviour nearly in the full range of its deformation process, as illustrated in Figure 3-24. A detailed analysis on the deformation process of the metallic specimen was conducted to reveal the reason behind the loss of auxetic behaviour in Figure 3-23b. At the beginning of the compression process ($\varepsilon < 0.06$), the initial

localization of plastic deformation occurred within the bottom layer of cells, and they were crushed firstly. As compression progressed, more localization took place within the central layers until all layers of the specimen were crushed and a non-auxetic deformation pattern was formed, as shown in in Figure 3-23b. The observed crushing process also showed that the localized plastic deformation did not propagate layer by layer. This deformation localization triggered a different pattern without auxetic behaviour. Thus, the key feature of the observed pattern in the brass specimen with PSF = 0% was the localization of plastic deformation. Inherently, deformation localization in one layer was caused by the sudden decrease of loading modulus of the metallic base material. The starting layer for this localization was determined by the manufacture imperfection in the brass specimen.

3.3.3 FE simulation

3.3.3.1 Post-buckling analysis and validation of numerical models

FE simulations were conducted to further clarify the loss of auxetic behaviour of metallic buckling-induced metamaterials and to reveal the features observed in experiments on the new metallic auxetic metamaterials. A nonlinear post-buckling analysis on all of those metamaterials under uniaxial compression was carried out using ABAQUS/Explicit (Simulia, Providence, RI, USA). It should be noted that the results of post-buckling analyses were affected by the effects of complex self-contact and large deformations. Remarkably, the complex self-contact was an unavoidable factor for large deformation analysis. To overcome this obstacle, the explicit simulation was carried out with a prescribed velocity profile. The mechanical properties of brass were set as a bilinear material model in FEA. In numerical models, the classical metal plasticity model was used to define the yield, hardening rule, and inelastic flow of the metamaterials at relatively low temperatures. The plasticity behaviour of this model was simplified as a bilinear isotropic hardening behaviour. The von Mises yield surface is used to measure isotropic yielding by defining the exact value of yield stress as a function of uniaxial equivalent plastic strain. The inertia effect was minimized by defining amplitude to apply the velocity on top of the FE model as it was used in reference [131]. The velocity was applied gradually and the acceleration at the beginning and ending of compression process was zero.

At the first stage of post-buckling analysis, the FE simulations were carried out utilizing 3D solid elements, the same as the previous buckling analysis. The deformation process of the newly designed metallic auxetic metamaterial with PSF = 20% is shown in Figure 3-23c. A comparison of the deformation process between the experiments and the numerical model revealed an excellent agreement between them, as shown in Figure 3-23.

Three-dimensional shell elements were used to reduce the computational costs. Four nodes, standard linear square element with second order accuracy (S4R) were used with at least five integration points at the minimum links in the FE model. The FE simulation results with shell elements were validated by comparing with experimental results and also with the result of previous post-buckling analyses with 3D solid elements, as shown in Figure 3-25a. They agreed with each other in general trend and features. However, the level of stress corresponding to FE results was higher than the stress level from the experimental results. These differences were attributed to the imperfection of the printed specimen in our experiments, which was supported by the large variation of properties.

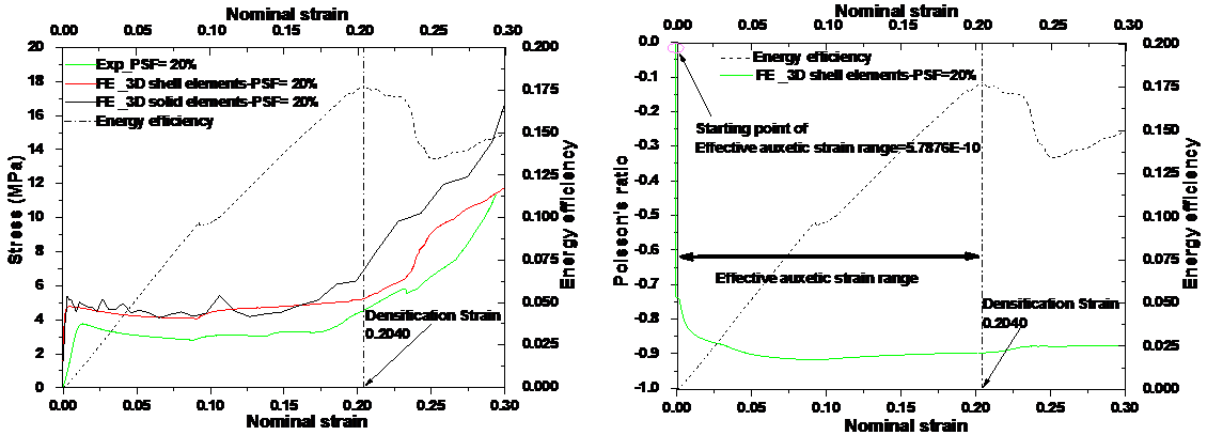

Figure 3-57 (a) Comparison of nominal stress-strain curves of the auxetic metamaterial between experiment and FE results (FE models with 3D shell elements and 3D solid elements) and using energy efficiency method to find densification strain; (b) defining the lower bound and upper bound of effective auxetic strain range.

3.3.3.2 Defining a strain range for auxetic metamaterials using the energy efficiency method

In this study, the effective auxetic strain range was defined as the strain between the starting point for negative value of Poisson's ratio shown in Figure 3-25b and the densification point from stress-strain

shown in Figure 3-25a and b. The starting point of effective auxetic strain range was defined as the first point that Poisson's ratio began to decline as shown in Figure 3-25b.

The auxetic behaviour of the metallic metamaterial started after application of a very small strain in the compression test, and this value was close to zero. The endpoint of the effective auxetic range was densification strain, and this physically corresponded to the starting pointof a sharply rise of stress in the stress-strain relationship as shown in Figure 3-25a. It was shown that from the densification strain onwards, the stress level in stress-strain curve rose sharply. The term "effective" was used to indicate two important features of the metallic auxetic metamaterials within the described strain range for their potential applications. One was that the nominal Poisson's ratio was negative and similar, and the other was that the stress level over the entire deformation range was similar and below the densification strain. A relative constant plateau stress and similar Poisson's ratio over the entire deformation range from the FE results were calculated using an energy efficiency method. Similar to section 3.1.4, firstly the absorbed energy was defined as the total area under the stress-strain curve by using Equation 3-2. Then, the energy efficiency parameter was found by dividing the absorbed energy by the stress itself. When the $E(\varepsilon)$ reaches the maximum point, the corresponding strain was the densification strain. The densification strain is marked by a dashed line in Figures 3-25a and b. As a special feature, the fact that the densification strains from the experimental data were similar to those from the FE results also proved the accuracy of the FE models.

3.3.3.3 Parametric studies

After the numerical models were validated, parametric studies were carried out to confirm the cause of loss of auxetic behaviour for buckling-induced metallic specimens identified in the experiments. As for the pattern-altered specimen, the dominant factors to control the performance of metallic auxetic metamaterials were identified and qualified using the validated FE models. Based on experimental observations, the reason for the loss of auxetic behaviour for metallic specimens was related to the plastic deformation of the buckling-induced auxetic metamaterials. The localization of the plastic deformation caused by buckling at an RVE length scale resulted in a global deformation mode rather than the desired buckling pattern in all RVEs. It was difficult to verify this assumption directly.

However, two methods to prevent the localization of plastic strain could be applied to buckling-induced design. The first method was eliminating buckling by introducing a large imperfection; the second method wass the increase of strain hardening modulus of its base material close to the elastic modulus. If those methods should be effective, the assumption would be proved indirectly. As mentioned before, the buckling mode alternation of the microstructure could be used as an innovative approach to design new metallic auxetic metamaterials.

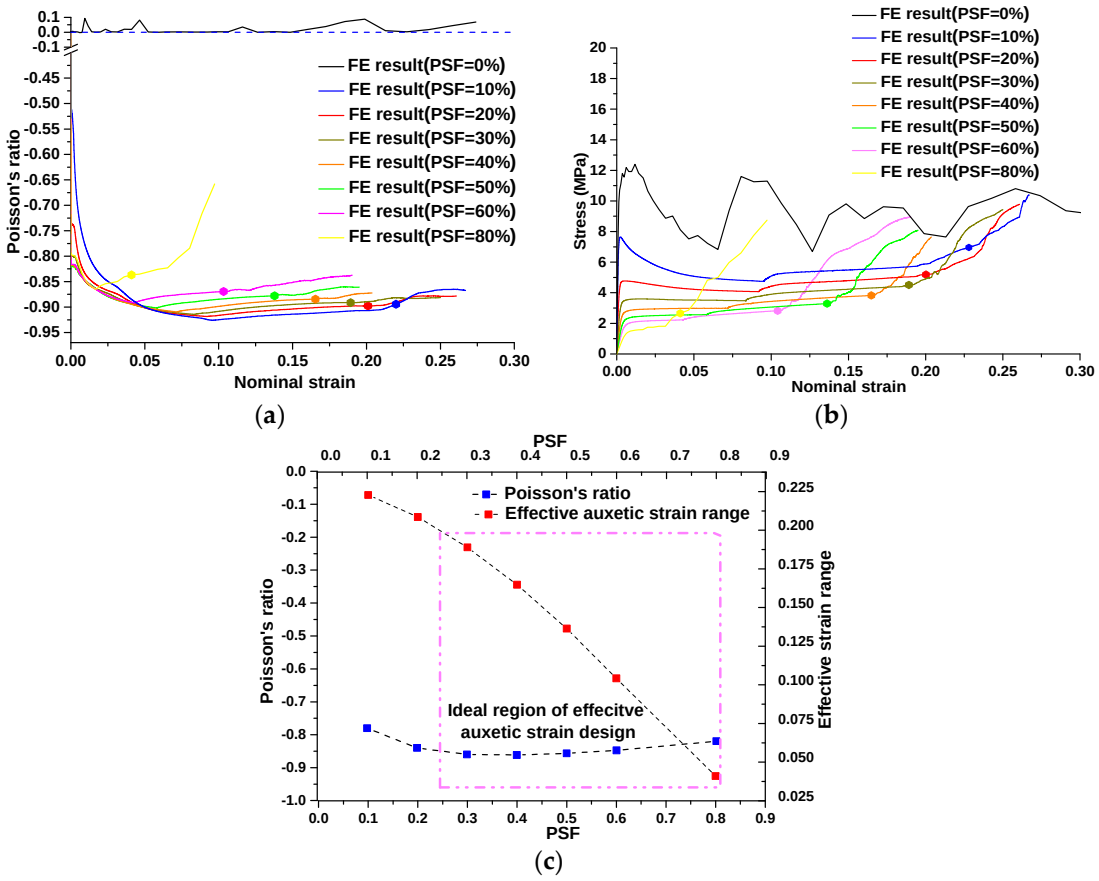

Figure 3-58 Parametric study on influence of PSF on auxetic behaviour; (a) evaluations of Poisson's ratio as function of applied strain corresponding to different PSF; (b) stress-strain curves corresponding to different PSF; (c) average values of Poisson's ratio and effective auxetic strain ranges corresponding to different PSF.

To enhance and facilitate its potential applications, an individual tuning method should be provided to assist with the design of a metallic metamaterial with a prescribed performance. Based on the feature of metamaterials, the change of Poisson's ratio could be achieved by adjusting the geometrical configuration of microstructures, while other mechanical properties can be achieved by changing the

elastoplastic properties of its base material. It was difficult to individually change those features by experimental methods, so the validated FE model was used to do the parametric study.

In the current study, the magnitude of alteration was represented by PSF. As mentioned before, the PSF was a key parameter to alter the initial topology of RVE with desired buckling mode. The range of variation of PSF was between 0% and 100%. A series of systematic simulations were conducted to study the influence of PSF on auxetic performance of the new metallic auxetic metamaterials. The elastoplastic properties of brass were defined identically to the material properties in the experiment. The results are presented in Figure 3-26, in which the effective auxetic strain range is marked with round dots.

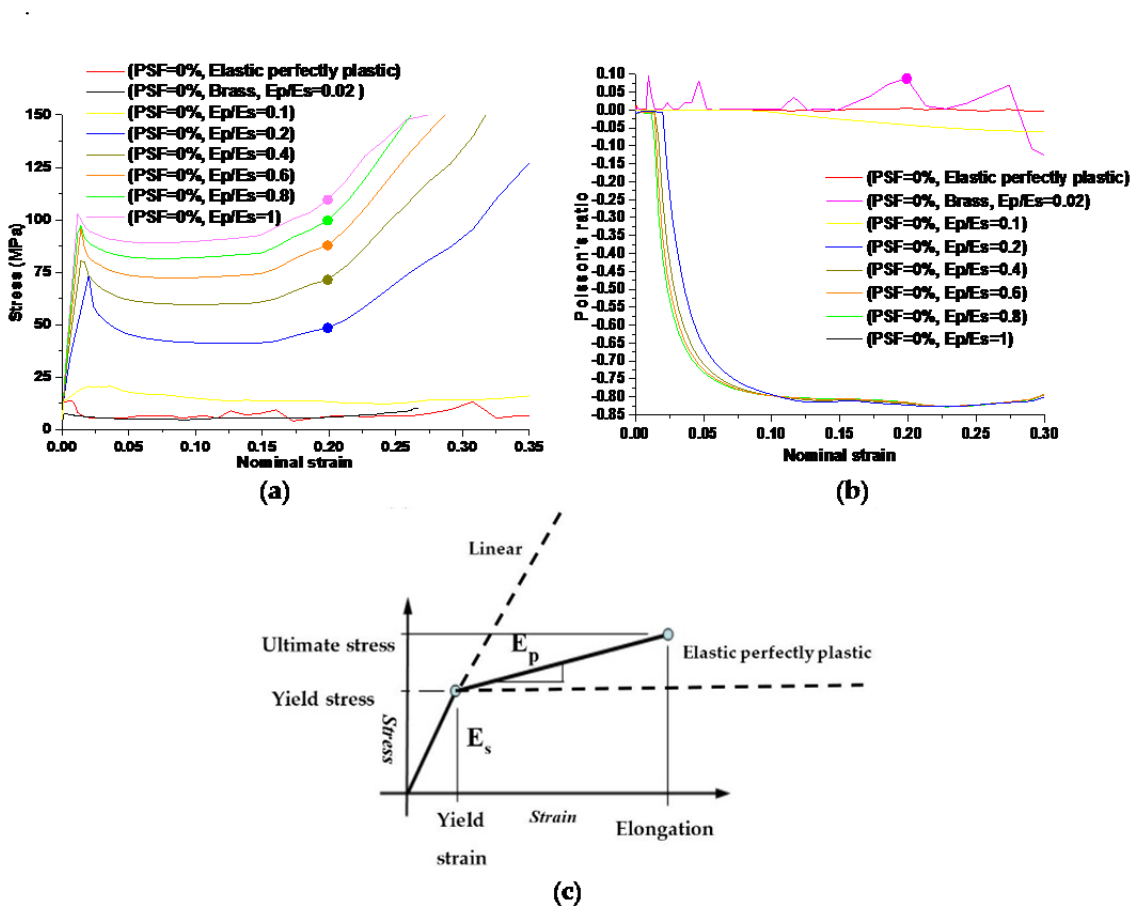

Figure 3-59 The results of a parametric study on the influence of plastic hardening on the recovery of auxetic behaviour; (a) evaluations of Poisson's ratio as a function of applied strain corresponding to different hardening ratios for metamaterials with PSF = 0%.; (b) stress-strain curves corresponding to different hardening ratios for metamaterials with PSF = 0%; (c) schematic curve of stress-strain for metallic materials (strain hardening ratio).

According to these results, it was determined that the increase of PSF resulted in the decrease of the densification strain and thus the effective auxetic strain range for auxetic behaviour. This

phenomenon was obvious, as shown in Figure 3-26c. By increasing the PSF, the mutual ellipses in RVE became smaller, thus the internal walls of the elliptical parts touched each other at a smaller strain. Therefore, the densification strains decreased accordinglyThe nonlinear response of Poisson's ratio with respect to compressive strain is shown in Figure 3-26a with different PSF values. The negative values of Poisson's ratio did not change much with respect to PSF, especially when the PSF were in the range of 10% to 60%. This finding revealed that the value of Poisson's ratio was dominated by the deformation patterns initiated by the buckling mode applied. In this PSF range, the effective auxetic strain range can be individually designed with a prescribed negative value of Poisson's ratio required by the aimed application, as illustrated in Figure 3-26c. An ideal region for individually altering the effective auxetic strain was defined and illustrated with a dashed rectangle in Figure 3-26c. Within this region, Poisson's ratio maintained a constant negative value and the effective auxetic strain could be individually changed by the value of PSF.

For most metals, the plastic hardening modulus was not a constent value and it decreases with the evolution of the plastic strain. Thus, it was difficult to examine this effect using experiments. Therefore, FEA simulations were used instead. As mentioned previously, the strain hardening of the base material could be used to prevent the localization of the plastic deformation caused by buckling at RVEs. Plastic strain hardening is a common phenomenon for metallic materials, which can be simplified as a linear relationship with respect to plastic strain. It is represented by the slope of this line, termed the strain hardening modulus (Ep), in the stress-strain curves shown in Figure 3-27c. In most cases, the stress-strain curve of a metallic material is determined by the elastic region (Es) as well as the plastic region (Ep). In this study, a simple ratio was defined as Ep/Es to characterize the effect of plastic hardening on the auxetic performance of our designed metamaterials. This ratio was termed the "plastic hardening ratio." The variation range of this ratio is between 0 and 1.

A ratio of 0 represents perfectly plastic material and a ratio of 1 represents purely elastic material. The result for a plastic hardening ratio of 1 with buckling-induced metamaterials confirmed that increasing the plastic hardening ratio will restore the auxetic behaviour of buckling-induced metamaterials. As shown in Figure 3-23a, the experimental rubber specimen with PSF = 0% exhibited

auxetic behaviour under compression as a purely elastic material or when Ep/Es = 1. This finding was further validated by a numerical investigation on the initial geometry of buckling-induced metamaterial with PSF = 0%. The FE results for different values of Ep/Es at PSF = 0 are presented in Figure 3-27a and b. The response of a metamaterial changed from non-auxetic to auxetic by increasing the plastic hardening ratio. Based on this evidence, the reason behind the loss of auxetic behaviour was attributed to the localization of the plastic deformation caused by buckling at RVEs. To evaluate the effect of plasticity on the auxetic behaviour of our newly designed metallic auxetic metamaterials, the hardening ratio was varied in the range of 0 to 1. The results of this numerical parametric study for the newly designed buckling-induced metamaterial with PSF = 20% are presented in Figure 3-28 and for other values of PSF are shown in Figure 3-29.

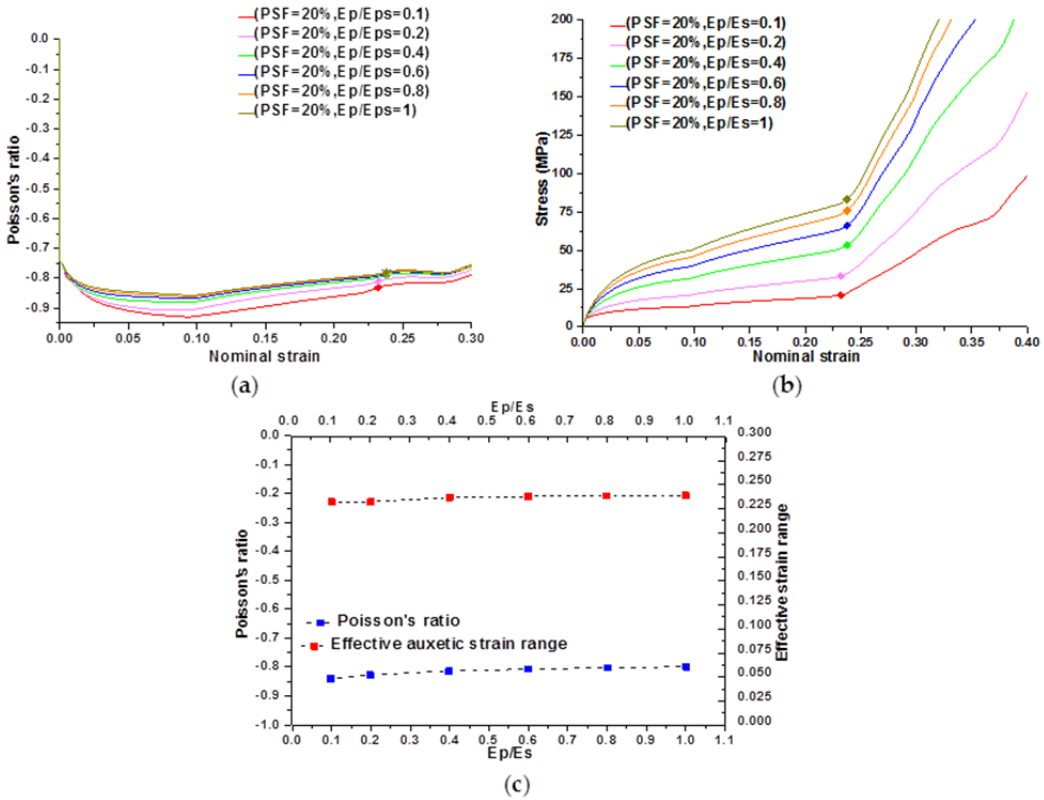

Figure 3-60 The results of a parametric study on the influence of plastic hardening on the auxetic behaviour of a metamaterial with PSF = 20%; (a) Evaluations of Poisson's ratio as a function of applied strain corresponding to different hardening ratios; (b) stress-strain curves corresponding to different hardening ratios; (c) average values of Poisson's ratio and effective auxetic strain ranges corresponding to different strain hardening ratios for metamaterials with PSF = 20%.

Also, it should be mentioned that when Ep/Es tends to zero, the response is closer to the rotation of rigid squares and so the Poisson's ratio tends to be -1. According to the numerical results shown in

Figures 3-28 and 3-29, the difference of the calculated negative value of Poisson's ratio for models with different strain hardening ratios were negligible. Also, the effective auxetic strain ranges for models with different hardening ratios were similar and the difference among these ranges can be neglected. Based on this observation, the auxetic performance of metallic auxetic metamaterials undergoing large deformation was dominated by the topology of the microstructures and it was independent of the properties of the base material. However, other mechanical properties such as the plateau stress increased considerably when the hardening ratios increased from 0 to 1.

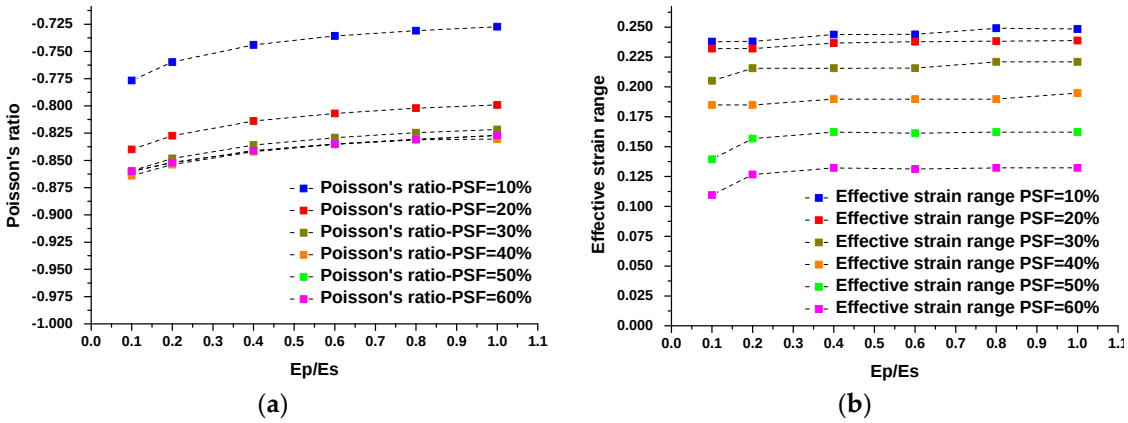

Figure 3-61 The results of a parametric study on the influence of pattern scale factors on auxetic behaviour and effective auxetic strain range; (a) Evaluations of Poisson's ratio as the function of hardening ratio corresponding to pattern scale factors; (b) evaluations of effective auxetic strain range as the function of hardening ratio corresponding to different pattern scale factors.

3.3.4 Effect of boundary conditions on the auxetic behaviour of the newly designed metallic auxetic metamaterials

Recently, Florijn et al. [133] presented a novel strategy to create a programmable mechanical metamaterial. They revealed that the response of a single metamaterial could be determined by confinement. Depending on the magnitude of the confinement, the deformation pattern and mechanical behaviour of the metamaterial could be tuned. Also, it was found from experiments that the boundary conditions had a significant effect on the deformation process of our metallic auxetic metamaterials. Thus, the influence of boundary conditions on the auxetic deformation patterns of those new 2D metallic auxetic metamaterials was investigated under compression using the validated FE model.

During the parametric studies in previous sections, the influence of the boundary was minimized by constraining all degrees of freedom on top and bottom surfaces nodes except for loading direction on the top surface. It was achieved in the experiments by adding two plates to the top and bottom of the designed specimen. However, in this part of the study, these plates were removed, so the top and bottom surfaces of new 2D designed metamaterial with PSF=20% were not constrained laterally as shown in Figure 3-30b. An experiment was conducted to reveal its effect on deformation process as illustrated in Figure 3-31. The only lateralconfinement was the friction between the specimen and on top and bot surfaces of the cross head of Shimadzu machine, but it was difficult to control its effect.

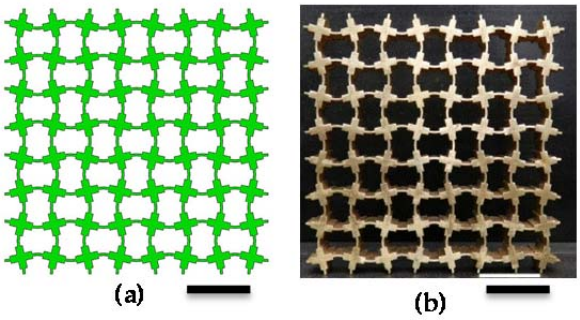

Figure 3-62 The new 2D design metallic metamaterial without top and bottom plates; (a) front view of numerical model with altered geometry (PSF= 20%); (b) Front view of printed brass specimen with altered geometry (PSF=20%, overall mass=185.57g, density=2728.53 kg m-3, mass error=1.08%, height×width×depth: 88mm×88mm×10mm, Scale bar: 20mm).

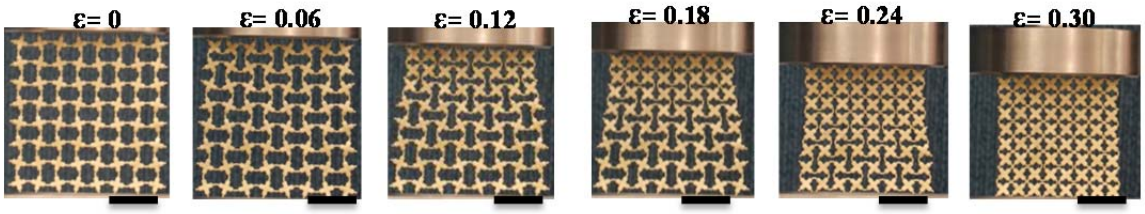

Figure 3-63 The different deformation pattern of the new 2D design of metallic auxetic metamaterial with PSF=20% without the top and bottom plates (Scale bar: 20 mm, load direction Y, strain rate: 5×10-3 S-1).

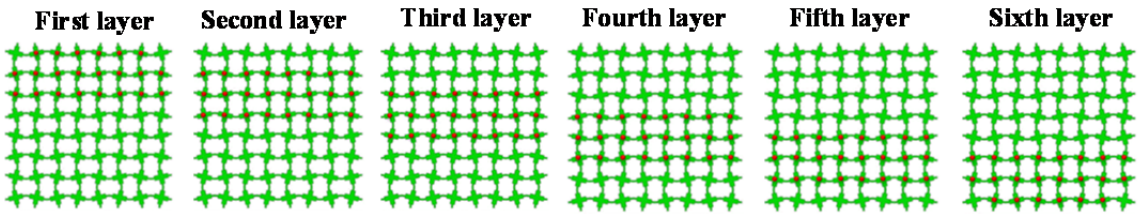

Figure 3-64 Identification of specified layers to calculate Poisson' ratio.

At the beginning of the test, a localized deformation occurred near the loading end. With further compression, the localized lateral inwards deformation developed from the top moving surface toward the bottom fixed surface. Interestingly, this deformation process led to obvious auxetic behaviour as shown in Figure 3-31 because the metamaterial contracted inward under compression from the top towards the bottom. Friction was one of the possible reasons to trigger such a sequential deformation process. One fair assumption was that the lateral friction force between the bottom surface and the bottom cross head of Shimadzu machine might be larger than that between metallic specimen and the top platen in the test. The coefficient of friction in the experiments was measured by the method described in [60], and the results confirmed and proved our assumption was correct.

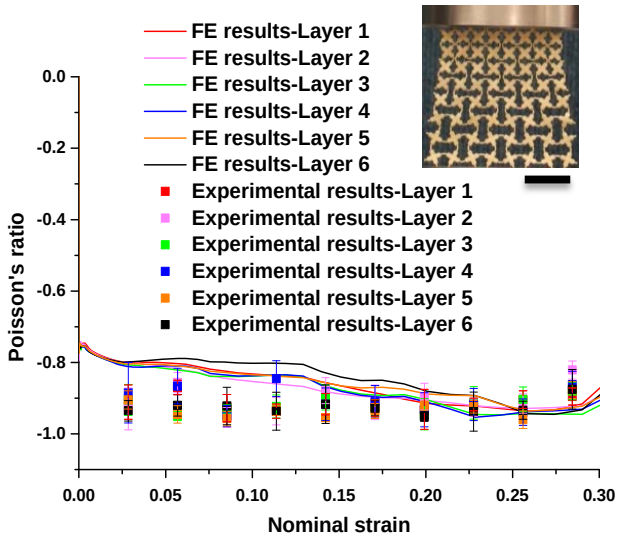

Figure 3-65 Comparison of NPR behaviour between experiments and FE simulation for a model with PSF=20% and without the top and bot plates (Scale bar: 20 mm, Volume fraction: 33.57 %, Load direction Y, Strain rate: 5×10^{-3} S^{-1}).

The surface of the specimen was divided into six layers from top to bottom to investigate the evolution of negative Poisson' ratio with respect to strain as shown in Figure 3-32, then the Poisson' ratio was calculated from the centre points of ligaments at each layer. A direct comparison of NPR at different compressive strains is shown in Figure 3-33 which demonstrates an excellent agreement between numerical and experimental results. It was also found that the NPR values corresponding to different layers were similar so as the overall tendencies with respect to compressive strain. Based on this finding, any layer can be used to calculate the NPR values to represent the auxetic behaviour of our designed metamaterial as a function of nominal applied strain as evidenced by Figure 3-33..

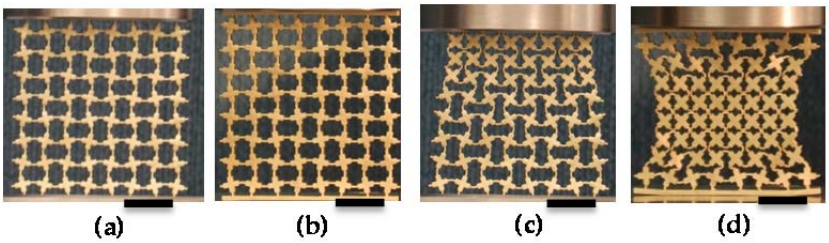

Figure 3-66 Different experimental deformation patterns of two printed specimens; (a) initial specimen with altered geometry (PSF=20%) without top and bottom added plates; (b) Initial specimen with altered geometry (PSF=20%) with top and bottom plates; (c) Auxetic deformation pattern of specimen with altered geometry (PSF=20%) without top and bottom added plates; (d) Auxetic deformation pattern of specimen with altered geometry (PSF=20%) with top and bottom added plates (Scale bar: 20mm).

The NPR versus strain curves of two specimens in Figure 3-34 were put together, and the results were presented in Figure 3-35. Interestingly, the overall trend and the average values of this set of NPR curves were similar. These observations illustrated that although the deformation process of our metallic auxetic metamaterial under compression was influenced by boundary conditions significantly, the auxetic performance was insensitive to the boundary conditions.

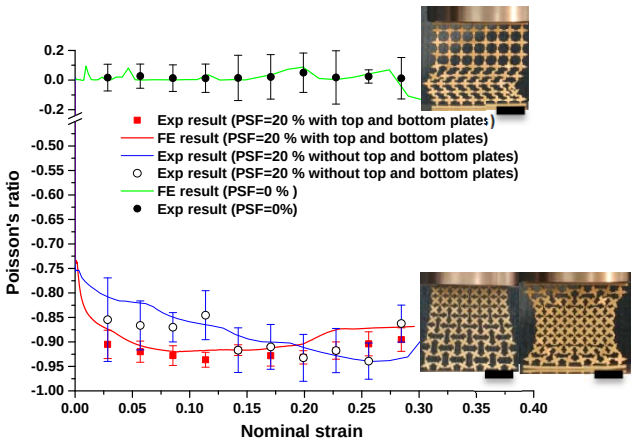

Figure 3-67 Comparison of auxetic and non-auxetic behaviours between buckling-induced design with PSF=0%, buckling pattern altered design with plates (PSF=20%) and buckling pattern altered design without plates (Scale bar: 20 mm, load direction Y, strain rate: 5×10^{-3} S^{-1}).

3.3.6 A brief summary of conclusions from this section

In the third part of this chapter a geometric modification of the conventional structure as RVE was proposed to design a new class of 2D metallic auxetic metamaterials. The effectiveness of the proposed method was validated by experiments. The experimentally validated FE models were used to carry out parametric studies on the effects of the plastic properties of the base material and the pattern scale factor on NPRs. The effect of boundary conditions on the auxetic performance of our 2D

auxetic metamaterial was also investigated. From the results of those investigations, the following conclusions can be drawn:

- The loss of auxetic behaviour in the metallic buckling-induced metamaterial was confirmed to be caused by the localization of plastic collapse of RVEs;
- The effective auxetic strain could be controlled individually by PSF while maintaining a similarly negative value of Poisson's ratio, especially when the PSF was in the range of 10% to 60%.
- The stiffness and strength of the metallic auxetic metamaterials could be individually controlled through adjustment of the properties of the base materials, while the negative value of Poisson's ratio remains relatively constant.
- The deformation process of the metallic auxetic metamaterial was influenced by boundary conditions; however, the auxetic behaviour and its performance corresponding to different deformation processes are insensitive to boundary conditions.

The results from FE simulation confirmed that the buckling-induced metamaterial would have auxetic behaviour after the plastic hardening modulus was large than a certain value determined by the microstructures of metamaterials. These results confirm that the effectiveness of increasing plastic hardening ratio will restore the auxetic behaviour of buckling-induced metamaterials.

Except for those solid conclusions based on our numerical and experimental results, there were some concerns relating to the 2D microstructures of our metallic auxetic metamaterials. The mechanism of the resultant metallic auxetic metamaterials is the rotating of joints/squares. The analytical model of rotating interconnected squares was proposed independently and simultaneously by Ishibashi & Iwata [134] and Grima & Evans [21]. Thus, most of the auxetic behaviour of the metallic auxetic metamaterial can be predicted by their model. To some extent, the PSF used to define the topology of the RVE can be equivalent to the rotation angle of the square units in the analytical model. The insensitive negative value of Poisson's ratio of −0.9 with respect to PSF can be approximately explained by the negative value of Poisson's ratio of −1 in a model of the rotating of joints/squares. However, there is a noticeable advantage to using PSF to design the microstructures of

metallic auxetic metamaterials, besides tuneability. The volume fraction does not vary significantly through changing the PSF, as shown in Figure 3-47. Thus, it can be revealed that a set of 2D auxetic metallic metamaterials that are obtained with different PSFs have similar volume fractions.

It should be noted that the Poisson's ratio was measured in the centre region of the prototypes both in experiments and FE simulations. The nominal strain of the overall prototype was using to plot all strain-related curves. This method was used in all recent experimental-related research on auxetic structures and materials. This measurement resulted in the insensitivity of the measured Poisson's ratio with respect to strain localization. It will enlarge the negative strain range for auxetic behaviour, evidenced by the constant negative Poisson's ratio of −0.9 after its effective strain of 0.2. Based on the observed deformation of a metallic auxetic metamaterial, the walls of central rows of unit building cells are touching. However, the unit building cells of the top and bottom rows are not compacted completely. As mentioned before, the base martial of the prototype was made of ductile metal. Beyond the auxetic strain range, the metallic metamaterial can still be compressed further by plastic deformation of those not fully compacted layers. While the local strains in the central region remain nearly constant or are slightly compressed, the Poisson's ratio will remain negative. Thus, the measurement of the Poisson's ratio in the centre region may not be representative of the whole prototype when the strain localization occurs. We present those data just for comparison purposes; the accuracy of this measurement should be checked further. For a similar reason, we used the densification strain to define the end point for an effective strain range.

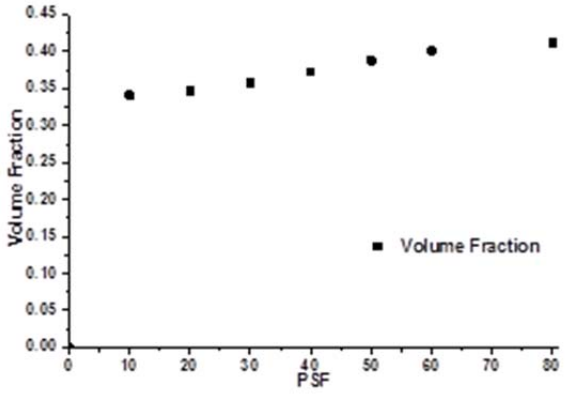

Figure 3-36 Relation between PSF and corresponding volume fraction.

It was revealed that the enhancement of the plastic-hardening ratio leads to restoring the auxetic behaviour of buckling-induced auxetic metamaterials. According to presented results, this effect is obvious when the hardening modulus is in the range of Ep/Es = 0 and Ep/Es = 0.3. Out of this range, the auxetic performance of models with different hardening ratios was similar and their differences could be neglected. This result is in accordance with the finding that the auxetic effect persists and becomes even stronger when the hardening modulus is in the range of h = 100 MPa and h = 1000 MPa by Dirrenberger et al. [62]. However, regarding the metallic auxetic metamaterials with altered microstructures, the influence of an enhancement of the plastic-hardening ratio on auxetic performance is negligible.

3.3.5 Development the analytical model of "auxetic rotating squares with plastic deformation" to describe the auxetic behaviour of the metallic auxetic metamaterial

In this section, a novel analytical model was developed to describe the auxetic behaviour of 2D metallic auxetic metamaterials with the potential to retain auxetic behaviour under large applied strains. Recently several idealized analytical models were developed to predict the auxetic behaviour of different auxetic systems, however these models were incapable to predict the complex deformation mechanism of auxetic systems undergoing large plastic deformation.

This new analytical model was based on previous work as the idealised analytical model of "rotating rigid squares" by Grima et al. [24]. Our new analytical model l could predict the auxetic behaviour and the of changing mechanical properties of the base material and changing geometry of microstructureusing PSF on the auxetic behaviour of the metallic metamaterials. The new development of the analytical model was to consider the plastic deformation of the rotating units. The new model started with the RVE of metamaterials constructed from four metallic deformable unit cells with two perpendicular intersecting diagonals which were connected by plastic hinges at their vertices. When the metamaterial was uniaxially compressed, the large amount of uniaxially deformation of the diagonal components of rotational unit cell occurred in the earlier stage of the large rotation of unit cells and the variation of axial strain was negligible in the later stage of the

rotation. Thus we neglected the plastic work done by the axial deformation.. In this analytical model, the contributions of these two mechanisms to the NPR were considered simultaneously. separated to derive. The analytical model would be more suitable to predict real metallic auxetic metamaterials than the idealized 'rotating squares' model. It should be noted that the analytical model was derived based on the assumption that the axial strain along loading direction had negligible effect on the rotation of the unit cells under large deformation. This assumption was supported by observation from both experiments and numerical simulations. Under such an assumption, the separate models could be used to describe the rotation through prime hinging model and axial deformation for large plastic strain of the unit cells.

3.3.5.1 Geometry of the analytical model of auxetic behaviour from rotating squares with plastic deformation

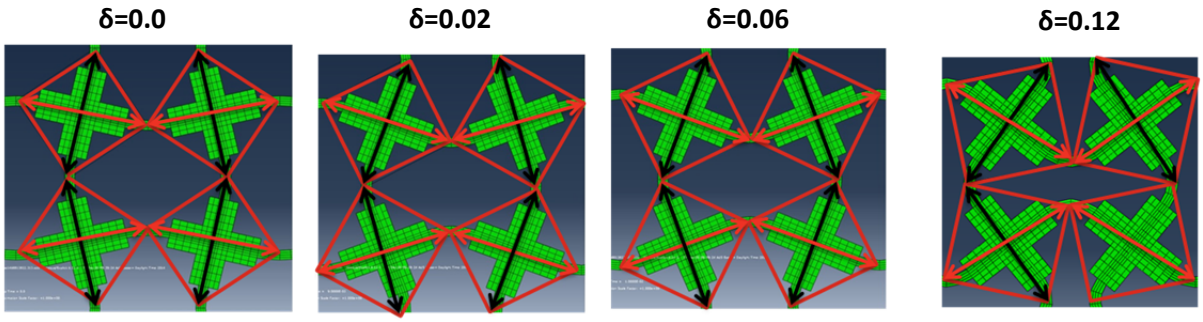

Figure 3-68 Deformation process of RVE of metallic auxetic metamaterial undergoing applied deformation.

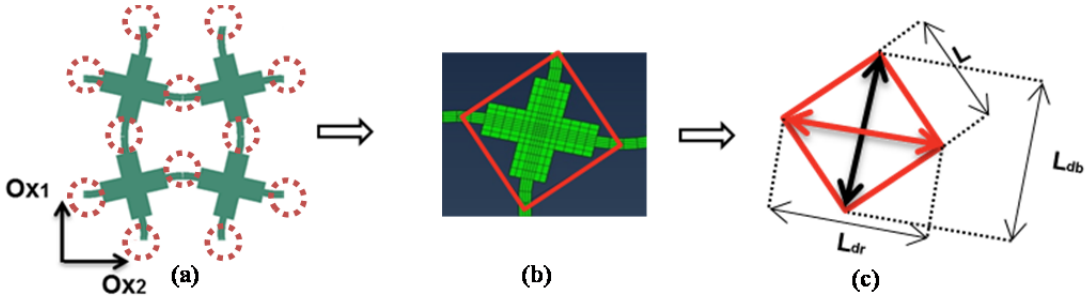

Figure 3-69 (a) Local buckling at the diffrenet regions of RVE; (b) rotational unit cell; (c) assumed perpendicular red and black diagonals of the unit cell.

According to the deformation process of RVE shown in Figure 3-37, the new analytical model was constructed from unit cells with two perpendicular intersecting diagonals with the lengths L_{dr} and L_{db}

which represented the lengths of two perpendicular diagonals of squares with the side length ***L***. Those dimensions are illustrated in Figure 3-38.

A set of FE simulation was conducted to investigate the axial deformation of two perpendicular diagonals (red and black ones) of a unit cell undergoing the rotation of unit cell. The PSF was fixed at 20%. The ratio of "plastic hardening ratio" (Ep/Es) varied in the range between 0 and 1.

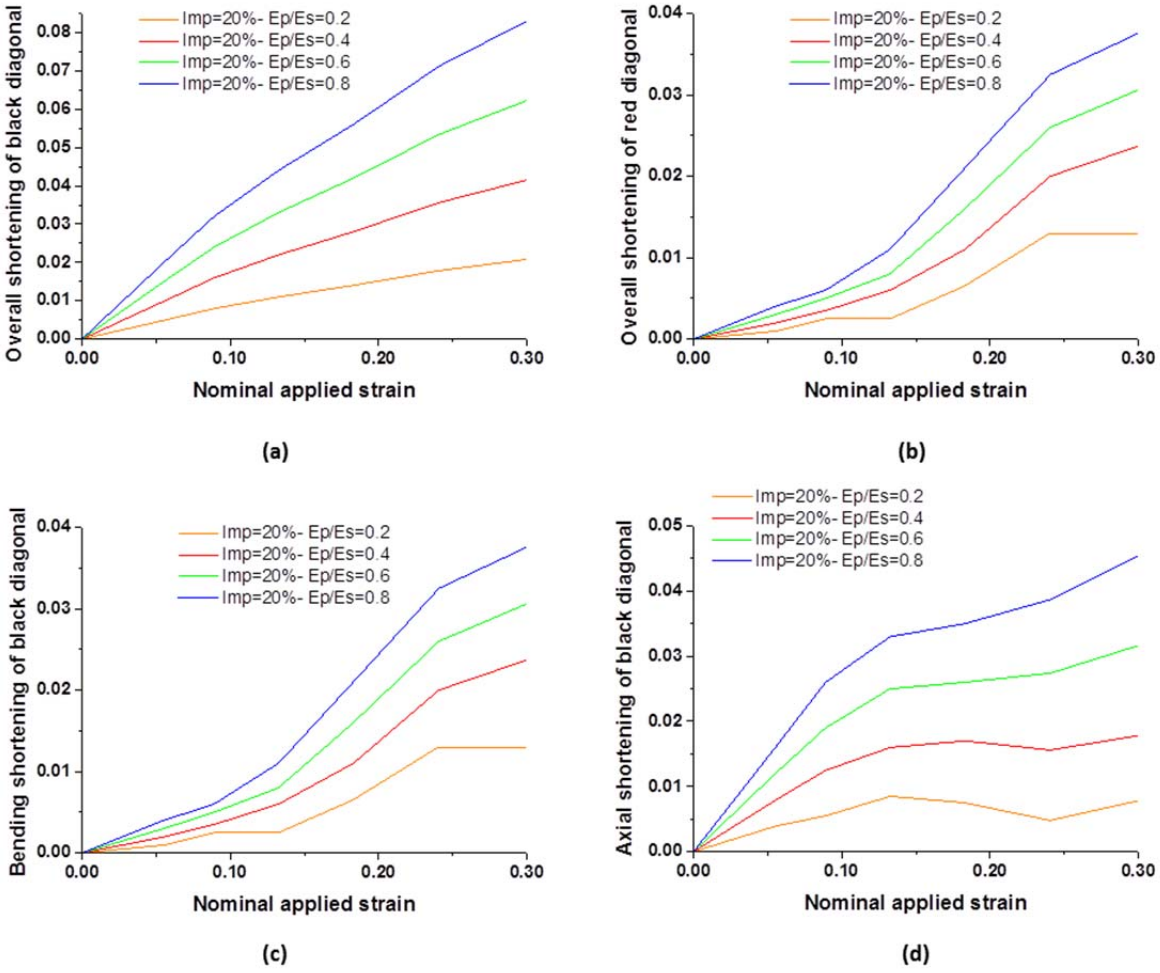

Figure 3-70 Comparison of the axial strain of perpendicular diagonals undergoing the rotation of unit cell; (a) axial strain of red diagonal; (b) axial strain of black diagonal; (c) Shortening of black diagonal.

The shortening of two assumed perpendicular diagonals (black and red) were compared together in Figures 3-39 a and b. The shortening was caused by two deformation mechanism in the black diagonals, i.e., axial strain of the diagonal as a result of applied load along OX_1 direction and the bending of the slender connection. For red diagonals, the shortening was only caused by bending because there was no axial load acting on it. Accordingly, we could assume the shortening by bending

were similar in red and black diagonals as shown in Figure 3-39 c. Then the axial shortening of the black diagonal could be obtained by subtract the overall shortening in Figure 3-39 a by the bending shortening of the black diagonal in Figure 3-39 c. The axial shortening of the black diagonal is shown in Figure 3-39 d. It shows clearly that the large amount of uniaxially deformation of the diagonal components of rotational unit cell occurred in the earlier stage of the large rotation of unit cells and the variation of axial strain was negligible in the later stage of the rotation. Accordingly, it was safe to assume that the axial strain along the black diagonal of unit cell would influence the NPR behaviour and the axial strain along the red diagonal of unit cell has negligible effect on NPR. Two diagonals within the same square were connected by a constrained joint similar to cross joint and were at a fixed angle φ = 90° to each other as shown in Figure 3-38 c.

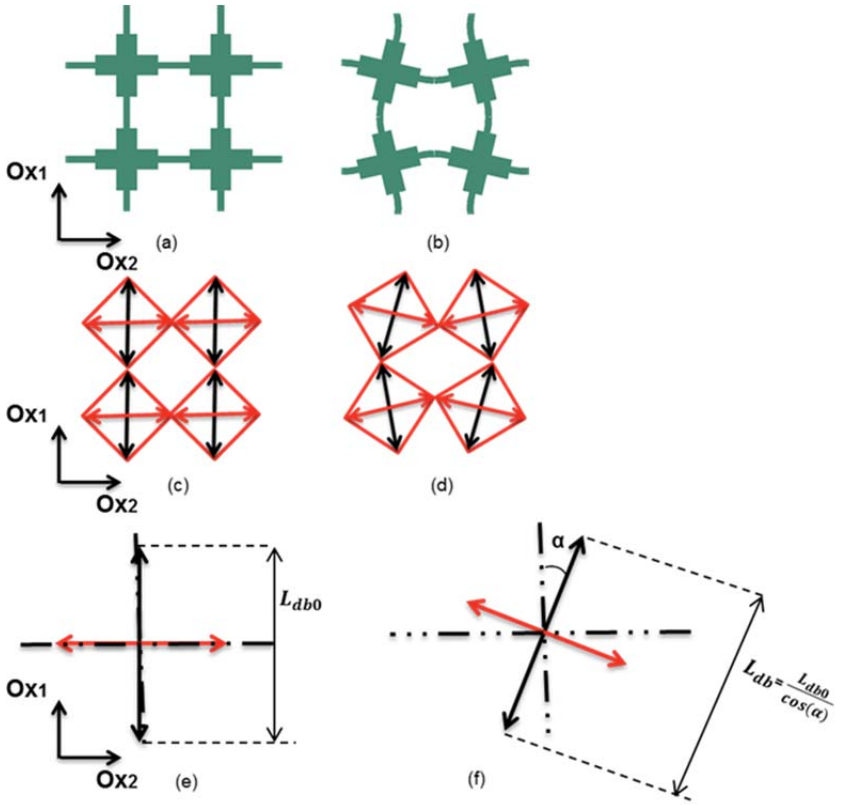

Figure 3-40 Definition of the variables of analytical model; (a) RVE of metallic auxetic metamaterial when PSF=0%; (b) RVE of metallic auxetic metamaterial when PSF=20%; (c) the geometry of analytical model for RVE when PSF= 0%, the squares shown in bold red, representing the original 'rotating squares' and the diagonals shown in bold red and black; (d) the geometry of analytical model of RVE when PSF= 20%; (e) the geometry of analytical model of unit cell where the squares are replaced by their diagonals when PSF=0%; (f) the geometry of analytical model of unit cell where the squares are replaced by their diagonals when PSF=20% and α= 9°.

Table 3-2 Variation of α with respect to different magnitude of alteration (PSFs)

PSF=0%	PSF=10%	PSF=20%	PSF=30%	PSF=40%	PSF=50%	PSF=60%	PSF=70%	PSF=80%
α= 0°	α= 4.5°	α= 9°	α= 13.5°	α= 18°	α= 22.5°	α= 27°	α= 33.5°	α= 36°

The diagonals from adjacent squares were connected by plastic hinges as shown in Figures 3-40 c and d. In order to define the magnitude of alteration of microstructure, a parameter, ***α,*** was defined to represent the change of the angle of the unit cell comparing to intial unit cell without alternation as illustrated in Figure 3-39 e. The variation of ***α*** was between 0° to 45° and each value of ***α*** angle was corresponding to one value of PSF as shown in in Table 3-2. In this analytical model, the angles α was used to calculate the load capacity and Poisson's ratio. Accordingly, the length of black diagonal $\boldsymbol{L_{db}}$ was the function of **α** parameter and was determined as $\boldsymbol{L_{db}}=\frac{\boldsymbol{L_{db0}}}{\boldsymbol{cos(\alpha)}}$ where $\boldsymbol{L_{db0}}$ was the initial length of black diagonal when PSF=0%.

3.3.5.2 Uniaxial loading in the OX_1 direction

Under compressive loading along OX_1 direction , the black diagonal deformed axially when the material at the joint entered into plastic deformation, and the unit cell begin to rotation. The diagonals from adjacent squares were also connected by hinges therefore the stiffness of microstructure of metamaterial resulted solely from the resistance to relative rotation of the diagonals**.** In other words, the diagonals were connected through plastic hinges with the moment of resistance of $\boldsymbol{M_P}$. Based on the rigid-plastic assumption of metallic base material,the theoretical limit of resistance was reached when the unit cell began to deform. After this, the section was fully plastic and the stress increase linearly above yield stress at all points in the section. The variation of plastic moment with respect to bending angle, θ, can be expressed in Equation 3-4. $\boldsymbol{M_P}$ was equal to $(\frac{\boldsymbol{bd^2}}{\boldsymbol{4}})\boldsymbol{\sigma_y}$ where ***b*** was the width of rectangular cross section, ***d*** was the height of cross section and $\boldsymbol{\sigma_y}$ was the yield stress. For the brass auxetic metamaterial , the width of rectangular cross section (***b)*** was $11*10^{-3}$ m, and the height of rectangular cross section **(*h*)** was $8.8*10^{-3}$m as shown in Figure 3-41, therefore the $\boldsymbol{M_P}$= 0.2464 N.m. Four moments acting on the unit cell of microstructure were as illustrated in Figure 3-41.

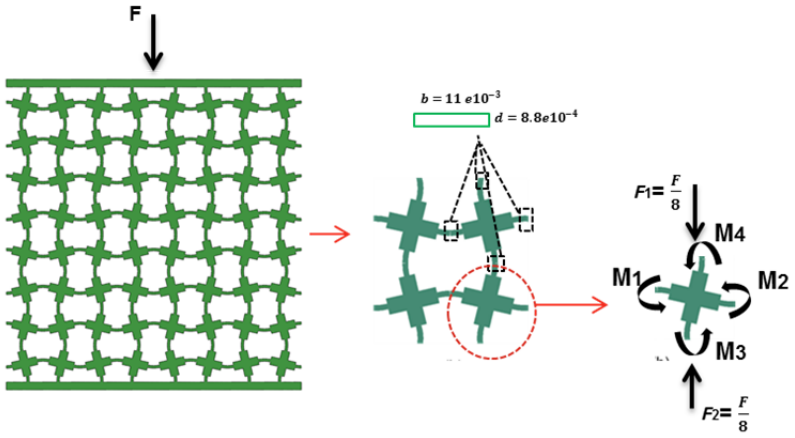

Figure 3-41 Definition of moments and forces acting on the unit cell of the microstructure of metallic metamaterial (M1=M2=M3=M4).

$$M = M_p\left(1+\frac{E_p\theta}{3\lambda\sigma_y}\right) \quad \lambda = 5 \tag{3-4}$$

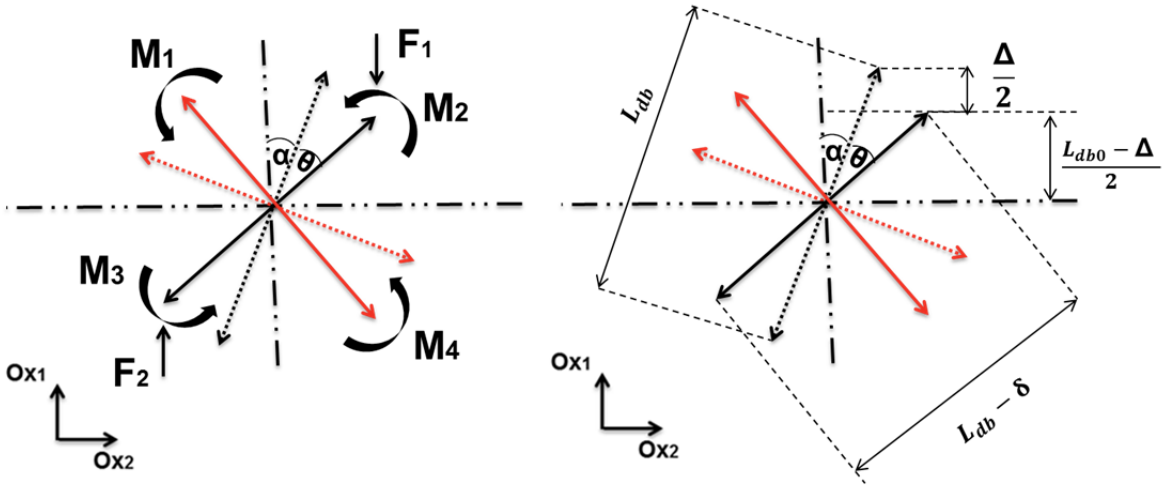

Figure 3-71 Definition of the variables of the analytical model under loading; (a) force and moment acting on diagonals under loading; (b) deformation of the unit cell in OX_1 where Δ presented the deformation of unit cell in OX_1 direction and δ presented the axial deformation of black diagonal.

Figure 3-41 represents the geometry of unit cell of new analytical model with all forces and moments acting on diagonals. Under loading along OX1 direction, the unit cell might deform through the rotation of diagonals which was presented by θ and the axial deformation of black diagonal which was presented by δ. Also, the deformation of the unit cell along OX_1 was presented with the parameter of **Δ**. The acting forces on the unit cell along OX_1 direction were presented with the

parameters of F_1 and F_2 and they were one-eighth of applied force to the bulk model as illustrated in Figure 3-41.

The amount of stress and strain of black diagonal under axial load (F_{axial}) was presented by Equations 3-5 and 3-6, Where σ_y and ε_y presented yield stress and yield strain of brass respectively, and E_p was the strain hardening modulus.

$$\sigma = \sigma_y + E_p \varepsilon_p \tag{3-5}$$

$$\varepsilon_p = \frac{(\sigma - \sigma_y)}{E_p} \tag{3-6}$$

The parameter of F_{axial} represents the applied axial force to black diagonal, and it was given by $F_{axial} = F_1 * \cos(\alpha+\theta)$. Therefore the stress of black diagonal was given as:

$$\sigma = \frac{F_{axial}}{A} = \frac{F_1 \cos(\alpha+\theta)}{bd} \tag{3-7}$$

As shown in Figure 3-4a a, the unit cell consists of two deferent parts with different thickness. The deformation of the thicker central part of unit cell was very small and it was negligible therefore it was supposed that only two third of the length of black diagonal was deformable. Therefore the Equation 3-6 was changed to:

$$\varepsilon_p = \frac{\delta}{\frac{2}{3}L_{db} - \delta} = \frac{1}{\frac{2}{3}\frac{L_{db}}{\delta} - 1} \tag{3-8}$$

According to Equations 3-7 and 3-8, the parameters of σ and ε_p were replaced in Equation 3-5 and it was given as:

$$\frac{F_1 \cos(\alpha+\theta)}{bd} = \sigma_y + \frac{3\delta E_p}{2L_{db} - 3\delta}$$
$$F_1 = \frac{bd}{\cos(\alpha+\theta)}\left(\sigma_y + \frac{3\delta E_p}{2L_{db} - 3\delta}\right) \tag{3-9}$$

According to Figure 3-41 b, the Equation 3-10 was derived to show the geometric relation among three parameters of θ, Δ, and δ.

$$\theta = arc\cos\left(\frac{L_{db0}-\Delta}{L_{db}-\delta}\right) - \alpha \quad (3\text{-}10)$$

In the following the equation 3-14 was derived to determine the axial deformation of black diagonal.

$$\frac{1}{\frac{2}{3}\frac{L_{db}}{\delta}-1} = \frac{\left(\sigma-\sigma_y\right)}{E_p} \quad (3\text{-}11)$$

$$\frac{2}{3}\frac{L_{db}}{\delta} = \frac{E_p}{\left(\sigma-\sigma_y\right)}+1 \quad (3\text{-}12)$$

$$\frac{L_{db}}{\delta} = \frac{3}{2}\frac{E_p+\left(\sigma-\sigma_y\right)}{\left(\sigma-\sigma_y\right)} \quad (3\text{-}13)$$

$$\delta = \frac{2L_{db}\left(\sigma-\sigma_y\right)}{3\left(E_p+\left(\sigma-\sigma_y\right)\right)} \quad (3\text{-}14)$$

According to Equations 3-7 and 3-10, the variable of $\boldsymbol{\sigma}$ and $\boldsymbol{\theta}$ were replaced in Equation 3-14 and it was given as:

$$\delta = \frac{2L_{db}\left(\left(\frac{F_1\cos\alpha}{bd}-\sigma_y\right)\right)}{3\left(E_p+\left(\frac{F_1\cos\alpha}{bd}-\sigma_y\right)\right)} = \frac{2L_{db}\left(F_1\cos(\alpha+\theta)-\sigma_y bd\right)}{3\left(E_p bd+F_1\cos(\alpha+\theta)-\sigma_y bd\right)} \quad (3\text{-}15)$$

Where: $\theta = arc\cos\left(\frac{L_{db0}-\Delta}{L_{db}-\delta}\right) - \alpha$

The virtual work is the work done by real force acting through a virtual displacement or a virtual force acting through a real displacement. A virtual displacement is any displacement consistent with the constraints of the structure, i.e., that satisfy the boundary conditions at the supports. The virtual work equation states that the external work is equal to internal work to relate two independent systems. Equation 3-16 determined the external work done by $\mathbf{F_1}$ and $\mathbf{F_2}$ corresponding to change in $\boldsymbol{\Delta}$. The internal work done per unit cell corresponding to change in $\boldsymbol{\theta}$, was given by Equation 3-17

where N is the number of hinges of a unit cell. , ***N*** was equal to 4, because each unit cell had four vertices and each vertex correspond to one hinge.

$$W_{external} = F_1 \Delta \tag{3-16}$$

$$W_{plasticwork} = 4\int_0^{\theta} M d\theta = 4\int_0^{\theta} M_p \left(1 + \frac{E_p \theta}{3\lambda\sigma_y}\right) d\theta = 4\left(M_p \theta\right) + \frac{2E_p\theta^2}{3\lambda\sigma_y} \tag{3-17}$$

Where: $M = M_p\left(1 + \frac{E_p\theta}{3\lambda\sigma_y}\right)$ $\lambda = 5$

From equating external and internal work, a new relation between deformation of the unit cell along OX_1 direction (***Δ***) and the axial deformation black diagonal ***δ*** was derived as following:

$$F_1 = 4\left(\frac{M_p\theta}{\Delta}\right) + \frac{2E_p\theta^2}{3\Delta\lambda\sigma_y} \tag{3-18}$$

The set of Equations 3-9 and 3-18 were solved by using Matlab software to calculate the acting force (***F_1***) on the unit cell along OX_1 direction for a varied range of ***Δ.***

$$\begin{cases} F_1 = \dfrac{bd}{\cos(\alpha+\theta)}\left(\sigma_y + \dfrac{3E_p}{2\frac{L_{db}}{\delta} - 3}\right) & (3\text{-}9) \\ F_1 = 4\left(\dfrac{M_p\theta}{\Delta}\right) + \dfrac{2E_p\theta^2}{3\Delta\lambda\sigma_y} & (3\text{-}18) \end{cases}$$

It is noted that the only variable of these Equations was ***Δ*** and through changing the magnitude of ***Δ*,** the corresponding value of ***F_1*** was calculated. Also it should be mantioned that the corresponding ***θ*** angle for different magnitudes of ***Δ*** was calculated by using the Equation 3-10.

A set of analytical equations was solved to study the effect of alteration of the geometry of microstructure on the stress-strain relation of auxetic system The set of Equation 3-9 and 3-18 was

solved for different values of **α** angle and the result of this analytical investigation was presented in Figure 3-43 b. Also, the same approach was employed to consider the effect of plastic hardening on the auxetic performance of our auxetic system.

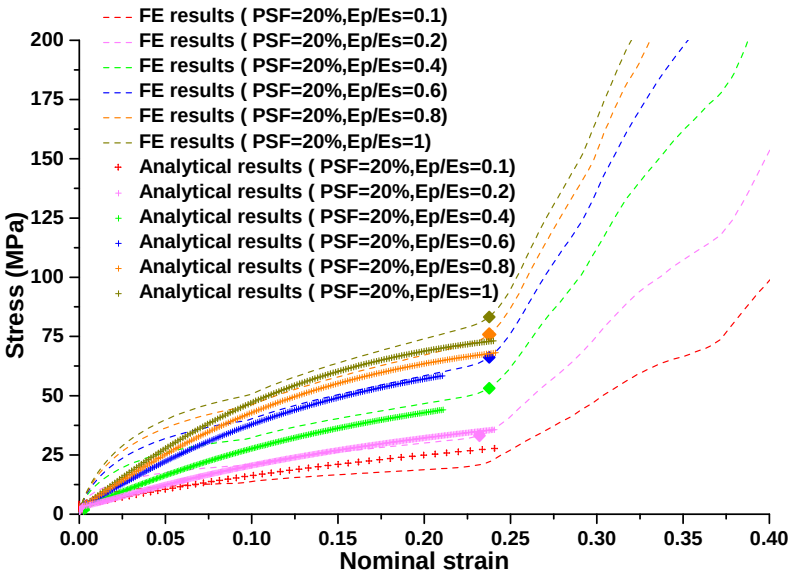

(a)

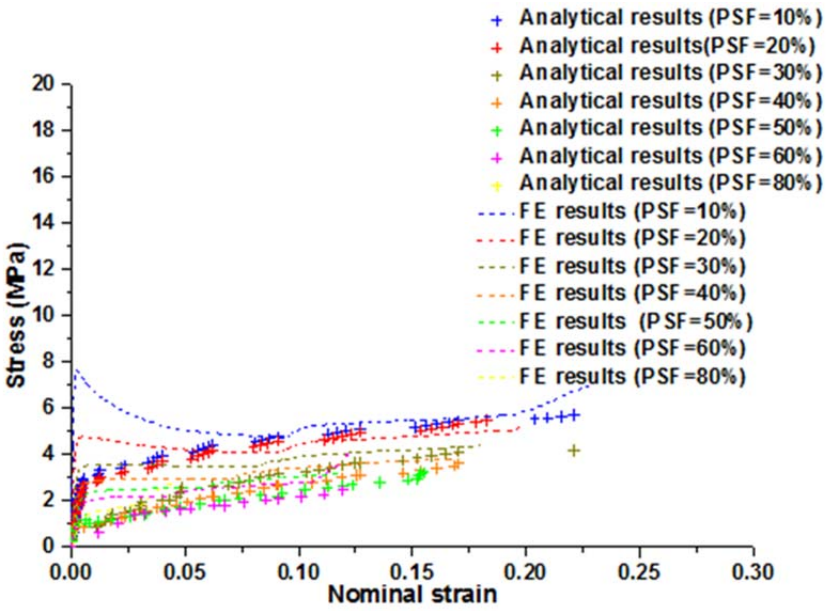

(b)

Figure 3-72 Comparison of the FE and analytical results of the parametric study; (a) the parametric study on the influence of plastic hardening on the stress-strain relationship of a metamaterial with PSF = 20%; (b) the parametric study on the influence of PSF the stress-strain relationship of a metamaterial with PSF = 20%.

The set of Equations was solved for different values of Ep / E and the result was reported in Figure 3-43 a. A comparison of the results of FE simulation and analytical investigation revealed an excellent agreement between them.

3.3.5.3 On-axis Poisson's ratio

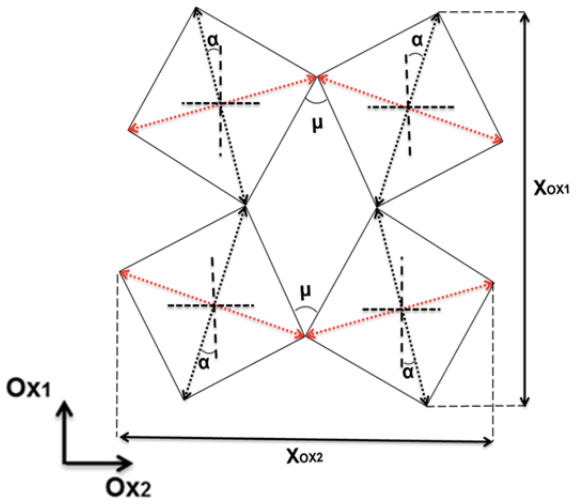

Figure 3-73 Geometry of RVE of an Idealized analytical model of "rotating rigid squares."

In the idealized analytical model of "rotating rigid squares" by Grima et al. [24], the geometry of analytical model was arranged involving rigid squares connected at their vertices by hinges. Referring to Figures 3-44, the diagonals of adjacent squares with the side length "l" at an angle μ to each other were connected by hinges. The dimensions of the RVE along OX_1 and OX_2 directions were given by:

$$X_{OX1} = X_{OX2} = 2l * [\cos\left(\frac{\mu}{2}\right) + \sin\left(\frac{\mu}{2}\right)] \quad (3\text{-}19)$$

Where $l = \frac{L_{db}}{\sqrt{2}}$ and $L_{db} = \frac{L_{db0}}{cos(\alpha)}$.

The Poisson's function for loading in the in the OX_1 direction defined by:

$$\vartheta_{OX1} = -\frac{d\varepsilon_{OX2}}{d\varepsilon_{OX1}} = -1 \quad (3\text{-}20)$$

It should be mentioned that the predicted value of PR from the idealized mechanism by Grima et al. [24] was an independent strain value and it was not the function of loading along OX_1 and OX_2 directions.

As mentioned before, under loading along OX_1 direction, the auxetic metallic system deformed through rotation of diagonals and the axial deformation of black diagonal as illustrated in Figure 3-45.

The mechanism of hinging at the vertices of intersecting diagonals and the plastic deformation of black diagonal, were combined to obtain the new analytical models for a system in which these two mechanisms act concurrently.

It was supposed that the axial strain along the black diagonal of unit cell influenced the NPR behaviour and the axial strain along the red diagonal of unit cell has negligible effect on NPR. Therefore, the dimension of the RVE along OX_2 direction was independent of plastic deformation, and it was given as an Equation similar to Equation 3-21:

$$X'_{OX2} = 2l * [\cos\left(\frac{\mu}{2}\right) + \sin\left(\frac{\mu}{2}\right)] \quad (3\text{-}21)$$

Referring to Figures 3-45 a new Equation was developed to measure the dimension of the RVE along OX_1 direction. The axial plastic deformation of black diagonal was measured by using the Equation 3-15. Therefore, the dimension of the RVE along OX1 direction was given as:

$$X'_{OX1} = 2l * \left[\cos\left(\frac{\mu}{2}\right) + \sin\left(\frac{\mu}{2}\right)\right] - 2\,\delta\cos(\alpha+\theta) \quad (3\text{-}22)$$

The PR value for loading along OX_1 direction defined by:

$$\vartheta_{OX1} = -\frac{d\varepsilon_{OX2}}{d\varepsilon_{OX1}} = -\frac{\frac{d\left(2l*\left[\cos\left(\frac{\mu}{2}\right)+\sin\left(\frac{\mu}{2}\right)\right]\right)}{d\theta}}{\frac{d\left(2l*\left[\cos\left(\frac{\mu}{2}\right)+\sin\left(\frac{\mu}{2}\right)\right]+2\,\delta\cos(\alpha+\theta)\right)}{d\theta}} \quad (3\text{-}23)$$

Where $\mu = 90 - 2(\alpha+\theta)$

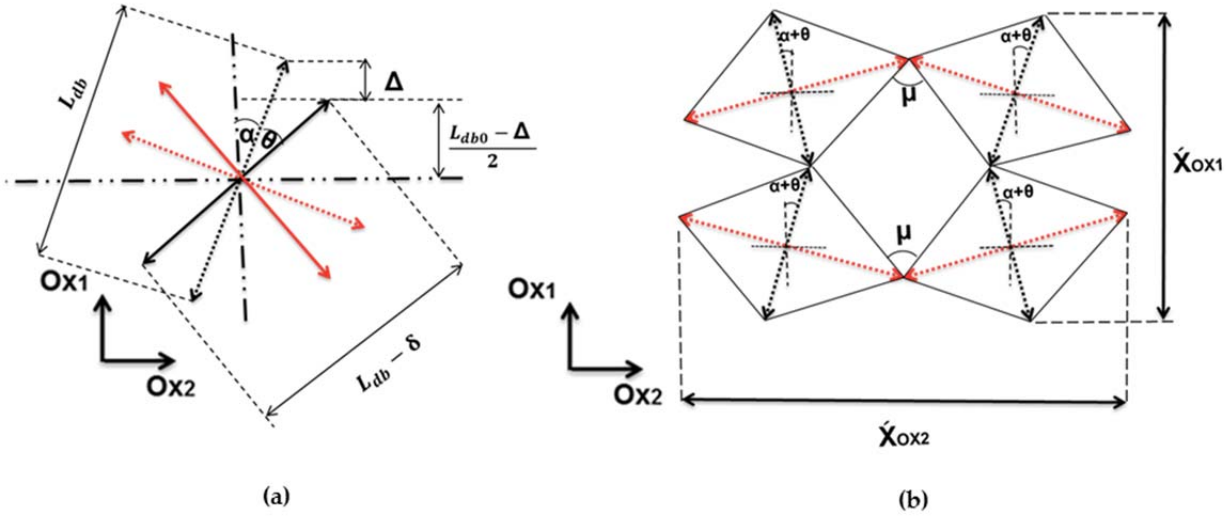

Figure 3-74 The Geometry of the new analytical model of "auxetic behaviour from rotating squares with plastic deformation"; (a) definition of the variables of the unit cell;(b) definition of the variables of the RVE.

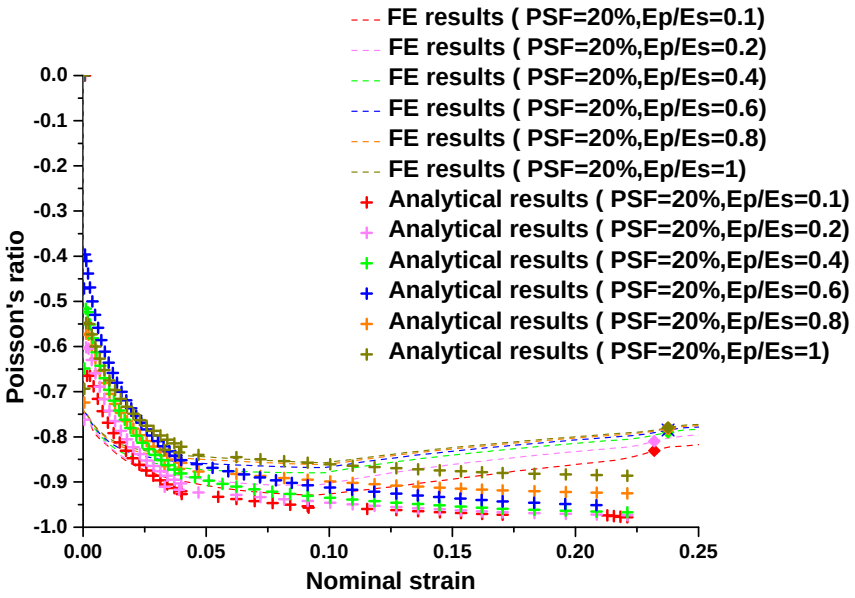

Figure 3-75 Comparison of the FE and analytical results of the parametric study; (a) study on the influence of plastic hardening on the auxetic behaviour of a metamaterial with PSF = 20%.

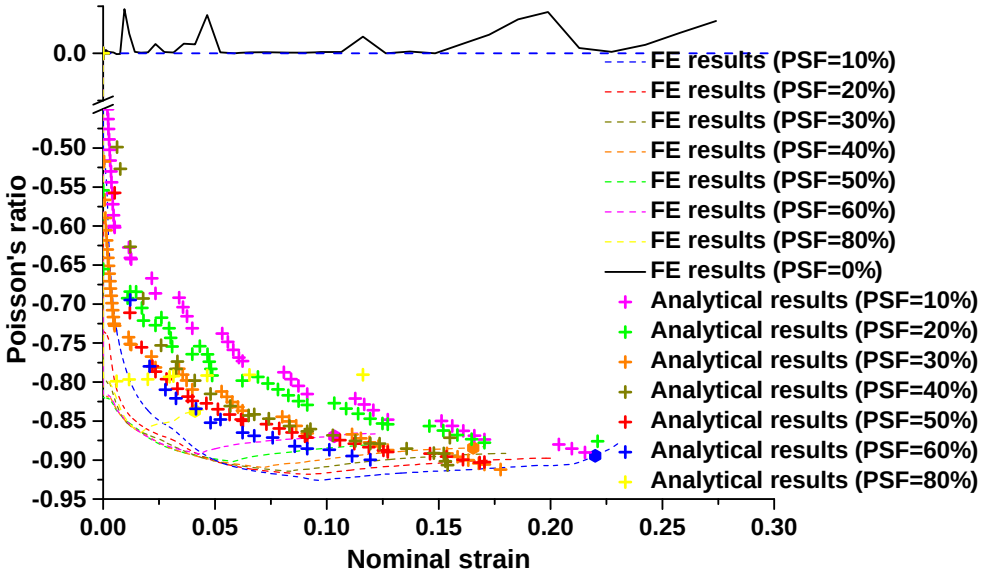

Figure 3-76 Comparison of the FE and analytical results of the parametric study; (a) study on the influence of plastic hardening on the auxetic behaviour of a metamaterial with PSF = 20%; (b) study on the influence of PSFon the auxetic behaviour of a metamaterial with PSF = 20%.

A set of analytical equations was solved to investigate the effect of alteration of the geometry of microstructure on auxetic behaviour (NPR value) of our metallic auxetic system under loading. Accordingly, the Equation 3-23 was solved for different values of α angle which were corresponding to the different magnitude of alteration of microstructure geometry, and the result of this analytical

investigation was presented in Figure 3-46 which demonstrates an excellent agreement between analytical and FE results. Also, the same approach was employed to study the effect of plastic hardening on the auxetic performance of our designed metamaterials. The Equation 3-23 was solved for different values of Ep / E and the analytical in Figure 3-47. A comparison of the results between FE simulation and analytical investigation revealed an acceptable agreement between them.

3.3.5.3 A brief summary of conclusions for analytical model

A novel analytical model was developed to describe the auxetic behaviour of 2D metallic auxetic metamaterials with the potential to retain auxetic behaviour under a wide range of applied strains. The new analytical model was developed based on previous work as the idealised analytical model of "rotating rigid squares" by Grima et al. [24]. Our new analytical model considered the plastic deformation of the base material and could predict the effect of large strain, plastic hardening, and initial geometric alternation using PSF on the stress-strain curves and NPR of the 2D auxetic metamaterial designed in previous sections. The theoretical prediction agreed well with both experimental results and numerical results from experimentally validated FE models.

3.4 Summary of Chapter 3

In this Chapter, several important factors relating to design auxetic metamaterials were explored including the geometric bounds of buckling-induced elastic auxetic metamaterialsm, the influence of metallic base materials on auxetic performance of buckling-induced metamaterials, special features of metallic base materials and analytical models for metallic auxetic metamaterials. Through those exploration, the following conclusions were drawn:

- A new reliable method were developed to identify the geometric bound for designing buckling-induced auxetic metamaterial under large deformation because the bound identified by linear buckling analysis may not be reliable in such cases;
- When the localization of plastic strain occurred in the microstructures, the buckling-induced auxetic behaviour was lost for the designed buckling-induced auxetic metamaterials. The loss

of buckling-induced auxetic behaviour was confirmed using samples with similar topological design but with different metallic base materials.

- Several new features of metallic auxetic metamaterials were identified and used to individually tune the effective auxetic strain of design metamaterials by PSF and the stiffness and strength by plastic properties of the base materials.
- A new analytical model was developed to predict the influence of large strain, plastic hardening, and initial geometric alternation on the stress-strain curves and NPR. The theoretical prediction agreed well with both experimental results and numerical results from experimentally validated FE models.

Chapter 4

Designing composites with negative linear compressibility

The phenomenon of negative linear compressibility (NLC) has attracted much interest because of its unusual deformation features with many potential applications. However, the designs and fabrication of materials and structures with NLC property were limited and rarely reported.

As mentioned before, there has been extensive work on materials and structures design using the composite techniques, covering various uncommon properties such as auxetic, negative stiffness, and negative thermal expansion. The basic idea of the composite technique was to improve the properties of materials and structures through adding a second phase to them in the form of fiber element or particulates. In Section 4.1 of this chapter, we proposed two approaches to designing and fabricating new NLC composite structures based on the application of composite techniques. The effectiveness of the proposed design approaches was validated experimentally using bulk specimens under uniformly distributed vacuum pressure. The deformation features, strain history, and the effective area reduction of the specimens were analyzed from the experimental data.

In Section 4.2 of this chapter, the progress of the research project entitled smart materials for negative pressure wound therapy (NPWT) was presented and the output of this research project was particularly applicable to treating a wound with NPWT system. The abdominal fascial could be closed

primarily at the end of most surgical incisions into a patient's abdominal cavity. However, sometimes full fascial closure was not possible and the operating surgeon was forced to leave the abdomen open. Different techniques were employed in order to temporary abdominal closure. It should be noted that after temporary abdominal closure, the abdominal fascia must be closed primarily. Whilst the abdomen remains open, numerous methods of temporary abdominal closure have been described, including towel clipping of skin edges, adhesive drapes, open packing, zipper closures, the Wittmann Patch, synthetic mesh, various plastic closures (such as the Bogot´a Bag, using an empty, opened intravenous fluid bag).

The aim of this project was designing wound filler and associated wound closure arrangement for NPWT system based on the designing approach for composite structures with NLC property which was proposed in Section 4.1. It should be mentioned the NPWT wound filler was useful in treating large wounds, such as abdominal wounds, where closure and approximation of the wound edges were challenging. The wound filler was configured to provide selective stiffness and deformation.
Accordingly, a physical wound model was built to study the open abdomen (OA) closure by using NPWT system. The composite prototypes with NLC was examined for OA wound closure.

4.1. Design and fabrication of new NLC composite structures

In this study, two design approaches were developed to produce a new series of NLC composite structures with a simplified manufacturing process. The main objective of these design approaches was to reinforce crushable foam with stiff members. The size of voids of composite structures was determined by the crushable foam cells, and the NLC behaviour was dominated by the deformation feature of the stiff members under vacuum pressure. The detailed design process was illustrated in the following sections.

4.1.1. Designing the NLC composite structure with a continuous hinged network

In the first design approach, a continuous network with NLC property was designed which the corresponding mechanism for NLC was similar to the wine-rack model. The topology design of the network microstructure was created through simplification of the results of our previous work [42] on the application of the bi-directional evolutionary structural optimization (BESO) to find the

microstructure of metamaterial with negative compressibility. As a result, similar to the geometry configuration in our previous work [42], the unit building cell of a continuous hinged network was generated as shown in Figure 4-1 a. According to the deformation pattern after loading, the representative volume element (RVE) of framework contained eight building cells as depicted in Figure 4-1 b. The continuous NLC hinged network was constructed with 8 RVEs along Y direction and 4 RVEs along X direction as shown in Figure 4-1 d. In order to form the building block of the NLC composite, specimens RVE of the continuous interior network was placed inside the filler component cube as shown in Figure 4-1 c. The building block was patterned along X and Y direction to form the bulk specimen of NLC composite structure as shown in Figure 4-1 e.

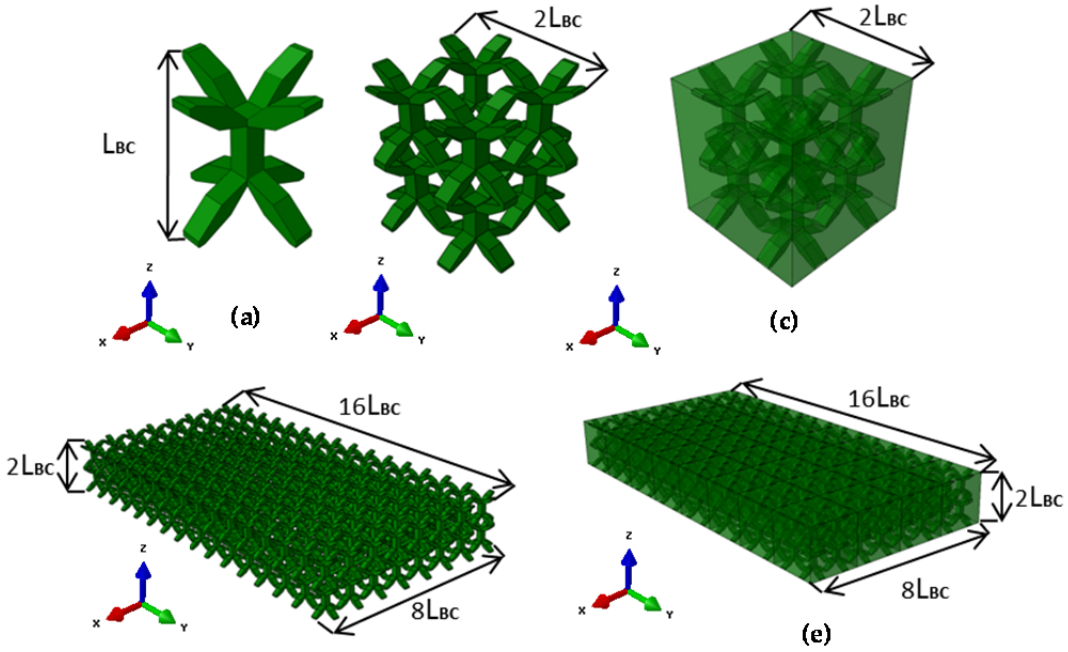

Figure 4-77 Topology design of NLC composite structure with continuous hinged network ;(a) unit building cell of NLC continuous hinged network; (b) representative volume element of NLC continuous hinged network; (c) building block of the NLC composite structure; (d) full size model of the continuous NLC hinged network; (e) NLC composite structure model with continuous hinged network (LBC=20 mm).

4.1.2. Designing the NLC composite structure with discrete truss elements based on specially ordered patterns

As mantioned before, the topology of the interior network of all known NLC composites was continuous, and the NLC property arises from a mechanism like a wine-rack model. The goal of this second design approach was to design a pattern of discrete truss elements which enables the

composite structure to exhibit NLC property with a different mechanism. The initial geometry of building blocks was very simple and was formed by embedding individual angled stiffeners in the highly compressible foam as shown in Figure 4-2 a.

The definition of NLC required a positive compressibility along two other axes perpendicular to the NLC axis. Under hydrostatic pressure, the volume compressibility must remain positive. Thus, increasing the PLC along two normal directions leads to the higher capacity of NLC along the third direction. The stiffeners were arranged in a particular pattern together with embedded apertures to facilitate their designed deformation mode inside the crushable foam as shown in Figure 4-2 a. The apertures were positioned between the stiffeners to assist the lateral movement of the stiffeners toward each other on the top surface. The apertures also enhanced the in-plane PLCs . Similar to the previous approach, the building block was patterned along two normal axes to form the experimental bulk specimen as shown in Figure 4-2 b.

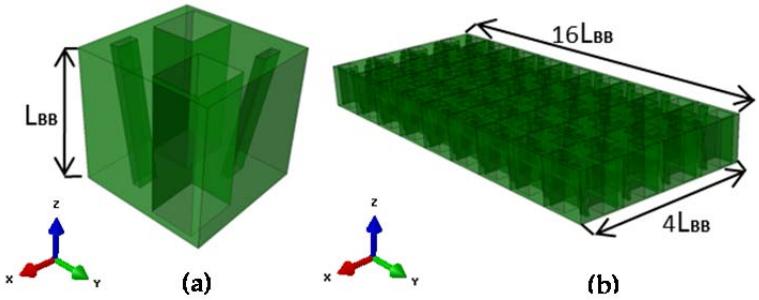

Figure 4-78 Topology design of NLC composite structure with discrete truss elements and the set of apertures; (a) unit building block with two angled stiffeners and two vertical apertures; (b) NLC composite structure model with discrete truss elements based on the specially ordered patterns (LBB=30 mm).

It should be noted that the stiffeners were more rigid and dense than the crushable foam material. The function of stiffeners was affected by the bonding between the filler component and the stiffeners. To improve the bonding effect, the surface of the stiffeners was indented to increase the contact areas. In this way, the friction between stiffeners and filler components provided sufficient resistance to prevent large relative sliding between the two different components.

4.1.3. Fabrication of specimens for experiments

Six experimental specimens were fabricated to examine the NLC property under vacuum pressure. The first and second specimens were manufactured based on the first design approach. The 3D

printing technique was used to create a continuous network by using the silicon base rubber material. The dimension of the printed continuous network was selected as height x width x depth = 40 x 160 x 320 mm as shown in Figure 4-3 a. The supporting material inFigure 4-3 in the original printed model was carefully removed by a drilling process followed by flushing using water. Various drills with different diameters (3, 8, 11 mm respectively) were used to remove the supporting material from small holes along X and Y directions. After the initial cleaning process, the printed networks were compressed 20% in all main directions, and they were flushed again by water.

For the base foam, we casted by using two liquid agents from PolyMech, the variation of the stiffness of the base foam could be achieved by adjusting the temperature of the foaming process and changing the ratio of the liquid agent. Based on the test we conducted, the weight ratio of the two liquid agents was changed from 100:55 (Part A: Part B) to 100:30. It should be noted that reducing the weight of part 2 resulted in the decrease of the strength of the base foam. If the weight ratio of part 2 was less than 30, the base foam produced was too weak for the current application.

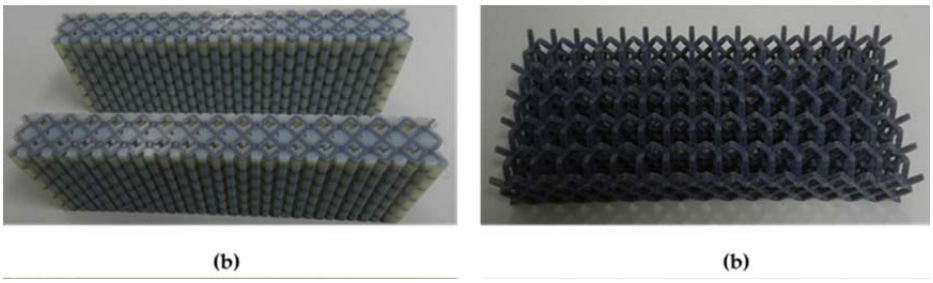

Figure 4-79 Removing supporting materials from 3D priniting model; (a) specimen of 3D printed NLC continuous network before removing supporting material; (b) specimen of 3D printed NLC continuous network after removing supporting material.

Using this method, the variation of density so as the densification strain for the base foam was very small. The closure ratio of the smart foam based on this base foam was not satisfactory. Initially, we used an oven with controllable temperature to cast the base foam, and it was successful for casting the base foam in a small size of 80mm×60mm×40mm. However, when we casted the prototype with a size of 240mm×190mm×50mm, the casting foam was failed because it could not reach its desired volume. The reason was that the large exposure area resulted in a faster consolidation of the base foam on the surface of the mixed liquids. It blocked the further expansion of the base foam during the foaming process. It resulted in a casting failure for the scaffolds printed by 3D printer as shown in

Figure 4-4 a. Later on, we improved our casting and foaming method by adopting a hot water bath using an incubator. The difference on the microstructures of the base foam was illustrated in Figures 4-4 b, and 4-4 c, which shows clearly the density of the foam reduces as the foaming temperature increases.

Accordingly, the temperature was kept at 80 degrees Celsius to manufacture the second specimen as shown in Figure 4-5 b.

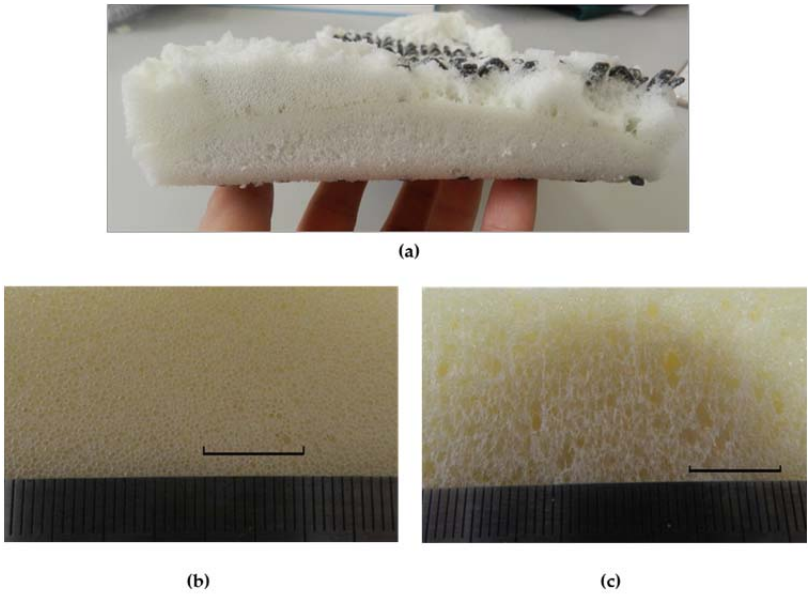

Figure 4-80 (a) Illustration of the denser layer due to the casting failure when manufacturing prototype; (b) illustration of casted base foam at room temperature; (c) illustration of casted base foam at 80º.

The dimensions of the third to six specimens were selected according to the availability of existing conventional foam. The third specimen consisted of pure foam without any stiffeners and apertures as shown in Figure 4-5 c and its behaviour was examined under vacuum pressure to show the lack of NLC property in the absence of embedded stiffeners. The fourth specimen with discrete truss elements and the set of apertures was shown in Figure 4-5 d. The stiffeners were common polyethylene, and the acute angle between them and the vertical Z axis was 10 degrees. The fifth and sixth specimens were fabricated in the same way but without apertures and the angle between stiffeners and vertical Z axis were about 10 degrees and 80 degrees respectively as shown in Figures 4-6 e and 4-6 f. A hot wire cutting technique was employed to make some slits for housing the

stiffeners inside the foam as illustrated in Figure 4-6. The apertures were cut in a similar manner, and their dimensions were selected as length x width = 10 x 12 mm.

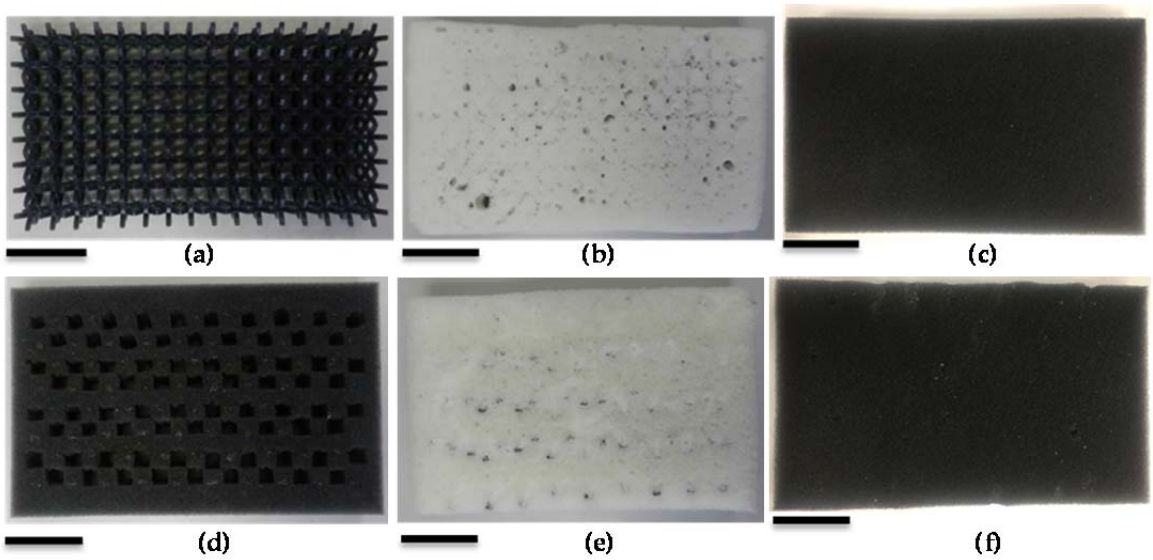

Figure 4-81 Six experimental specimens; (a) specimen of 3D printed NLC continuous network; (b) composite specimen with the continuous hinged network (overall dimensions of specimens with continuous network: height x width x depth = 40 x 160 x 320 mm); (c) experimental specimen of pure foam without discrete truss elements and apertures; (d) composite specimen with discrete truss elements and the set of apertures; (e) composite specimen with discrete truss elements without apertures (angle of stiffeners is 10 degrees); (f) composite specimen with discrete truss elements without apertures (angle of stiffeners is 80 degrees), (Number of specimens = 6, overall dimensions of specimens with discrete truss elements : height x width x depth = 30 x 120 x 270 mm), (Scale bar:20 mm).

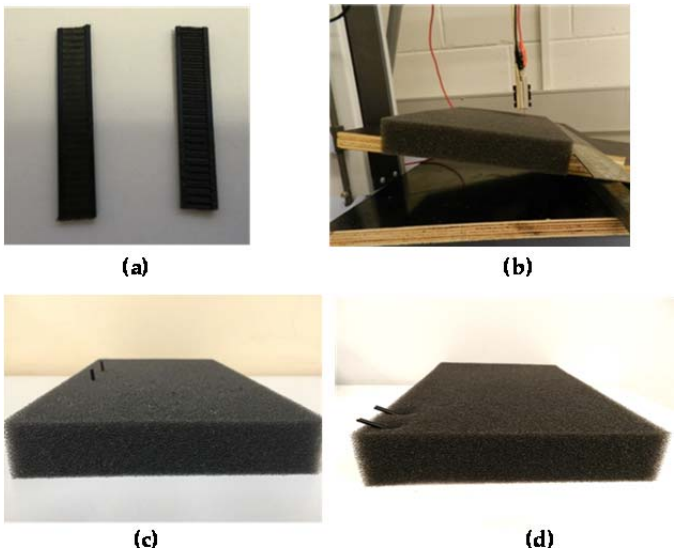

Figure 4-82 Fabrication process of experimental specimen with discrete truss elements using the hot wire cutters technique; (a) polyethylene stiffeners (height x width x depth = 31 x 10 x 2 mm); (b) passing the hot wire through the foam to make slits; (c) placing the stiffeners inside the foam with 10 degrees angle; (d) placing the stiffeners inside the foam with 80 degrees angle.

The fifth specimen was used to examine the influence of apertures on NLC property of the new design and the sixth specimen with 80 degrees angled stiffeners was fabricated to study the influence of the angle of stiffeners on NLC property.

4.1.4. Testing the performance of designed composite structures under vacuum pressure

4.1.4.1 Experiments on the base foam material

The base material of the composite specimens was the crushable foam, and its material properties were measured through standard compression test using six cylinder specimens with dimensions of diameter x height = 50 x 70 mm. The compression process stopped at the nominal strain of ε=0.85. A typical example of a nominal stress-strain curve was shown in Figure 4-7. The linear behaviour of foam was different from solid incompressible materials. Before densification, the foam materials exhibited a long plateau stress similar to the progressive crushing mechanism of metallic foams. However, the deformation and mechanical strength could be fully recovered after the load was removed and the stress-strain curves were repeatable when the same specimen was loaded several times. This behaviour originated from the buckling and elastic post-buckling deformation of cell walls of the foam.

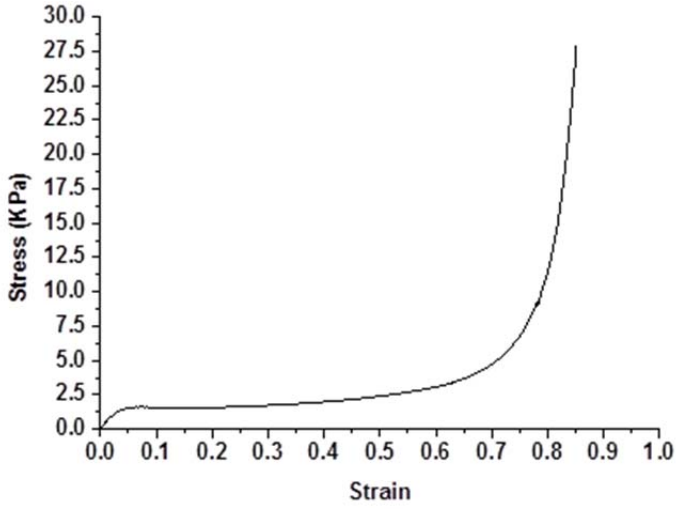

Figure 4-83 A typical stress-strain curve of the crushable foam used as the filler component of the NLC composite specimens.

4.1.4.2. Experimental set-up on designed NLC composites

The performance of the new specimens was tested under vacuum pressure. A camera was used to capture the in-plane deformation. Each specimen was put inside a sealed plastic bag connected with a

plastic tube. The sealed specimen was left on a smooth surface while the plastic tube was connected to the valve of the vacuum pressure pump. The internal pressure of sealable bag was gradually increased from 0 to 26.66 kPa with a fixed increment to monitor the variation of deformation pattern, top surface area reduction and out-of-plane deformation of specimens with respect to different levels of vacuum pressure. The pressure was held at 0, 5.33, 6.66, 7.99, 9.33, 10.66, 11.99, 13.33, 15.99, 18.66, 21.33, 23.99 and 26.66 kPa. Pictures taken with a camera (digital) involved variable distances from lens to top surfaces for different test specimens. Using Adobe® Photoshop®, the images for each test was calibrated. The calibration process started with counting the number of pixels from one known area on the scale and then counting the number of pixels from one unknown area on the image. In the next step, two numbers were compared together to find the nearest known area on to unknown area, thus determining the number of pixels per square mm for resolution. After calibration, the variation of in-plane area reduction were measured. The pressure resistance of NLC designs could be quantified from the area-pressure curves to assess the performance of different designs. For this purpose, the experimental values of in-plane area reduction for different designs were recorded from the calibrated photos at different levels of vacuum pressure. The relation between applied pressure and area reduction was presented as the Area-pressure curves for different composite designs.

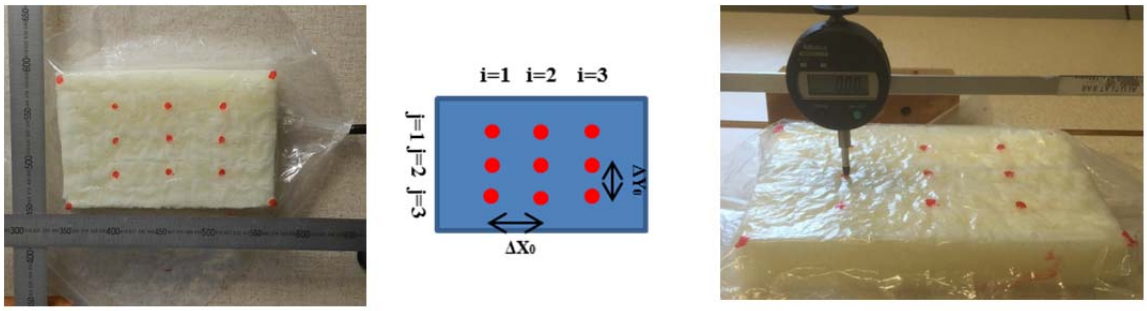

Figure 4-84 Experimental setup of the specimen under vacuum pressure; (a) sealed specimen; (b) schematic diagram of central region with nine marked red points ($\Delta x_0 = \Delta y_0 = 50\ mm$); (c) Dial gauge for measuring the out-of-plane deformation.

The experimental values of in-plane strains along X and Y directions were calculated through image processing from the nodes in the central parts of specimens. The central area consisted of 9 marked red points indicating $1 \leq i \leq 3$ and $1 \leq j \leq 3$ as shown in Figure 4-8. The point to point

distances along two main directions of X and Y were calculated by using coordinates $(x_{i,j}, y_{i,j})$, $\Delta x_{i,j} = x_{i+1,j} - x_{i,j}$ and $\Delta y_{i,j} = y_{i,j+1} - y_{i,j}$. The centre to centre distances between these points for undeformed specimen before compression were defined by $\Delta X(0) = \Delta Y(0) = 50\,mm$. Therefore, at each specific level of pressure, the coordinates of the centroid points were determined. Equation (4-1) was employed to calculate the local values of the in-plane strains along two main directions of X and Y. Eventually, six local values of in-plane strains along X and Y directions were calculated and the average of them was computed at each level of vacuum pressure. The out-of-plane deformation was measured using a dial gauge at 9 marked locations in Figure 4-8.

$$\epsilon_x = \frac{\Delta x_{i,j}}{\Delta x(0)} \quad \epsilon_y = \frac{\Delta y_{i,j}}{\Delta y(0)} \qquad (4\text{-}1)$$

4.1.4.3. Experimental results

The deformation patterns, the measured strain-pressure history along in-plane and out-of-plane directions and the pressure-area curves were presented in Figures 4-9, 4-10 and 4-11 respectively. Also, the deformation patterns of all experimental specimens at more level of pressures can be found in the appendix. Under vacuum pressure, no large scale out-of-plane bending and wrinkling were observed. From the Figure 4-9, it was found that the deformation process of all specimens was not similar and their shapes did not remain the same under different levels of vacuum pressure. The In-plane and out-of-plane deformations of samples were not uniform indicated by the difference of strains measued at nine points.

As can be seen from Figures 4-10 a and 4-10 b, the first and second specimens exhibited NLC property. However, the first specimen with the pure continuous network structure exhibited the larger in-plane and out-of-plane deformations than the second experimental specimen with the composite structure. Therefore, adding the crushable foam led to reducing the in-plane deformation and weakening the NLC property. The third specimen that consists of pure foam without any stiffeners and apertures did not exhibit NLC property as shown in Figure 4-10c. In contrast, the Figures 4-10 d and 4-10 e showed NLC property of the fourth and fifth specimens with 10 degrees angled stiffeners. Therefore it was concluded that reinforcing of the crushable foam with embedment of discrete truss

elements with specially ordered patterns and specific angle led to changing the crush pattern of pure foam and generating a new type of NLC composite structure. .

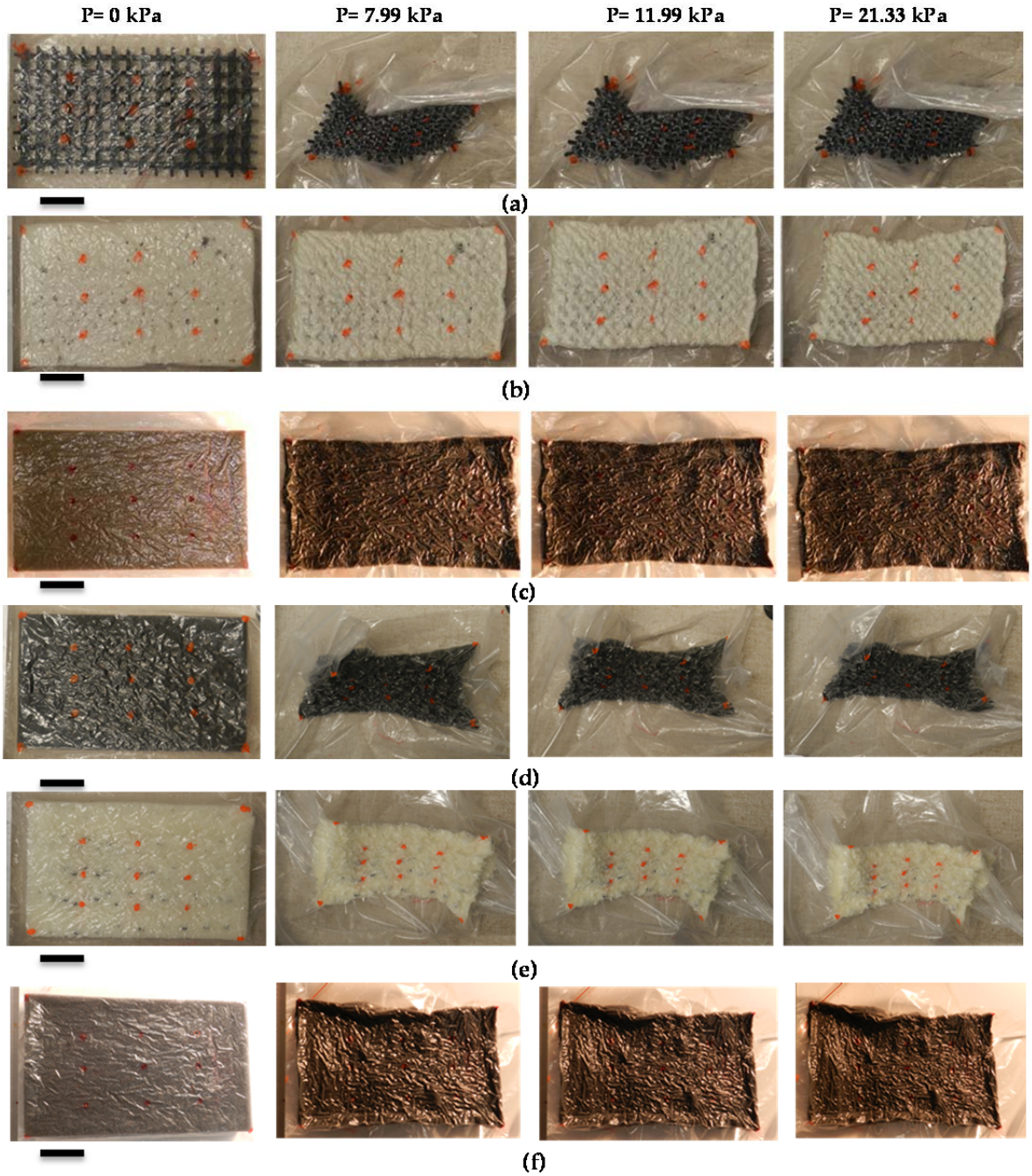

Figure 4-85 Deformed shapes of experimental specimens under vacuum pressure; (a) Specimen of 3D printed NLC continuous network; (b) composite specimen with the continuous hinged network; (c) specimen of pure foam without discrete truss elements and apertures; (d) composite specimen with discrete truss elements and the set of apertures with an angle of stiffeners of 10 degrees; (e) composite specimen with discrete truss elements without apertures with anangle of stiffeners of 10 degrees; (f) composite specimen with discrete truss elements without apertures with an angle of stiffeners of 80 degrees), (Scale bar:20 mm).

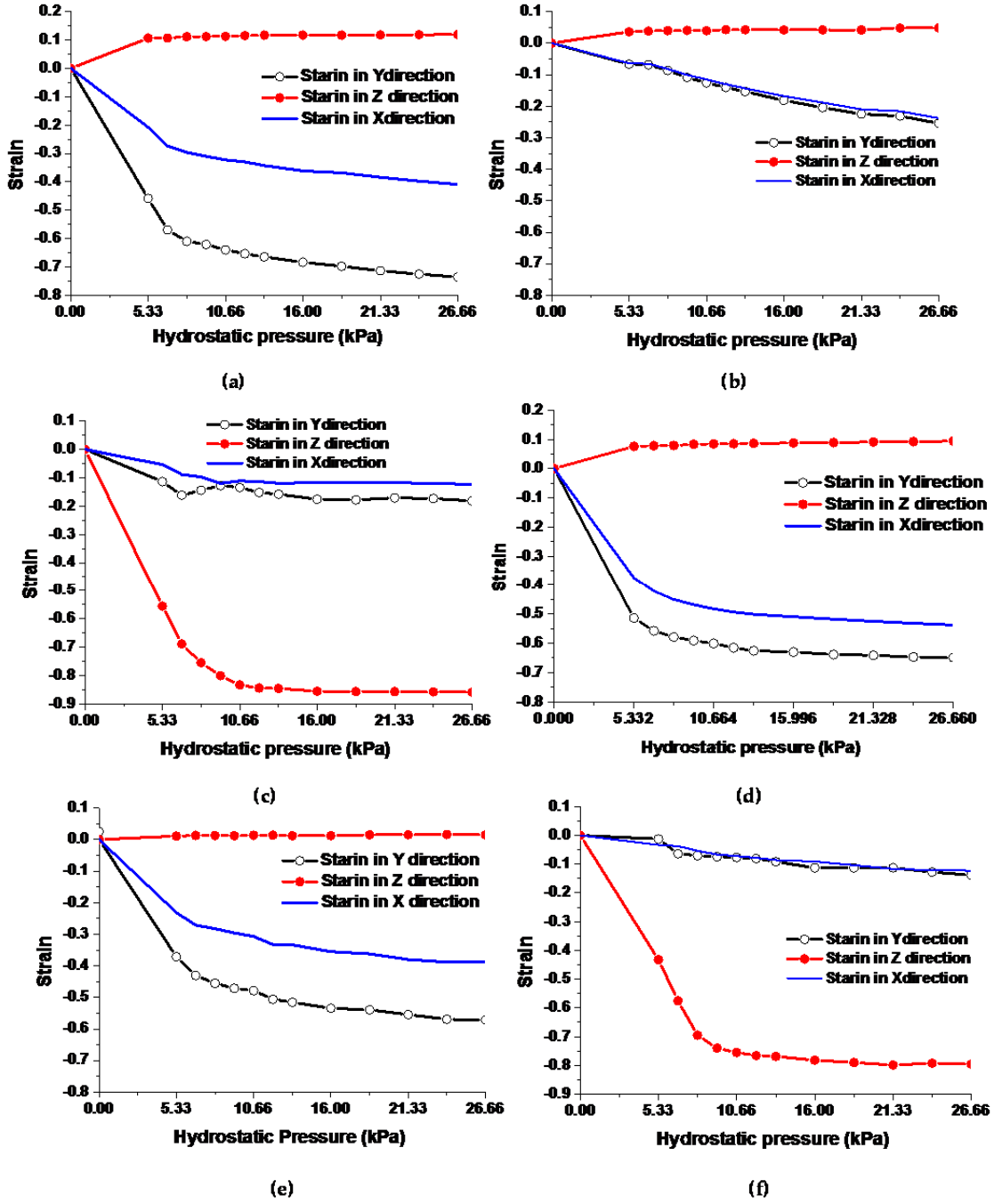

Figure 4-86 Strain–pressure history for experimental specimens under vacuum pressure; (a) specimen of 3D printed NLC continuous network; (b) composite specimen with the continuous hinged network; (c) specimen of pure foam without discrete truss elements and apertures; (d) composite specimen with discrete truss elements and the set of apertures with an angle of stiffeners of 10 degrees); (e) composite specimen with discrete truss elements without apertures with an angle of stiffeners of 10 degrees); (f) composite specimen with discrete truss elements without apertures with an angle of stiffeners of 80 degrees).

Also, comparison of strain–pressure history of fourth and fifth specimens in Figures 4-10 d and 4-10 e demonstrates that the fourth specimen with angled stiffeners and vertical apertures exhibited the larger in-plane and out-of-plane deformations compared with the fifth specimen. Thus,

modification of filler foam through several embodiment apertures led to a larger in-plane deformation and improved the NLC behaviour.

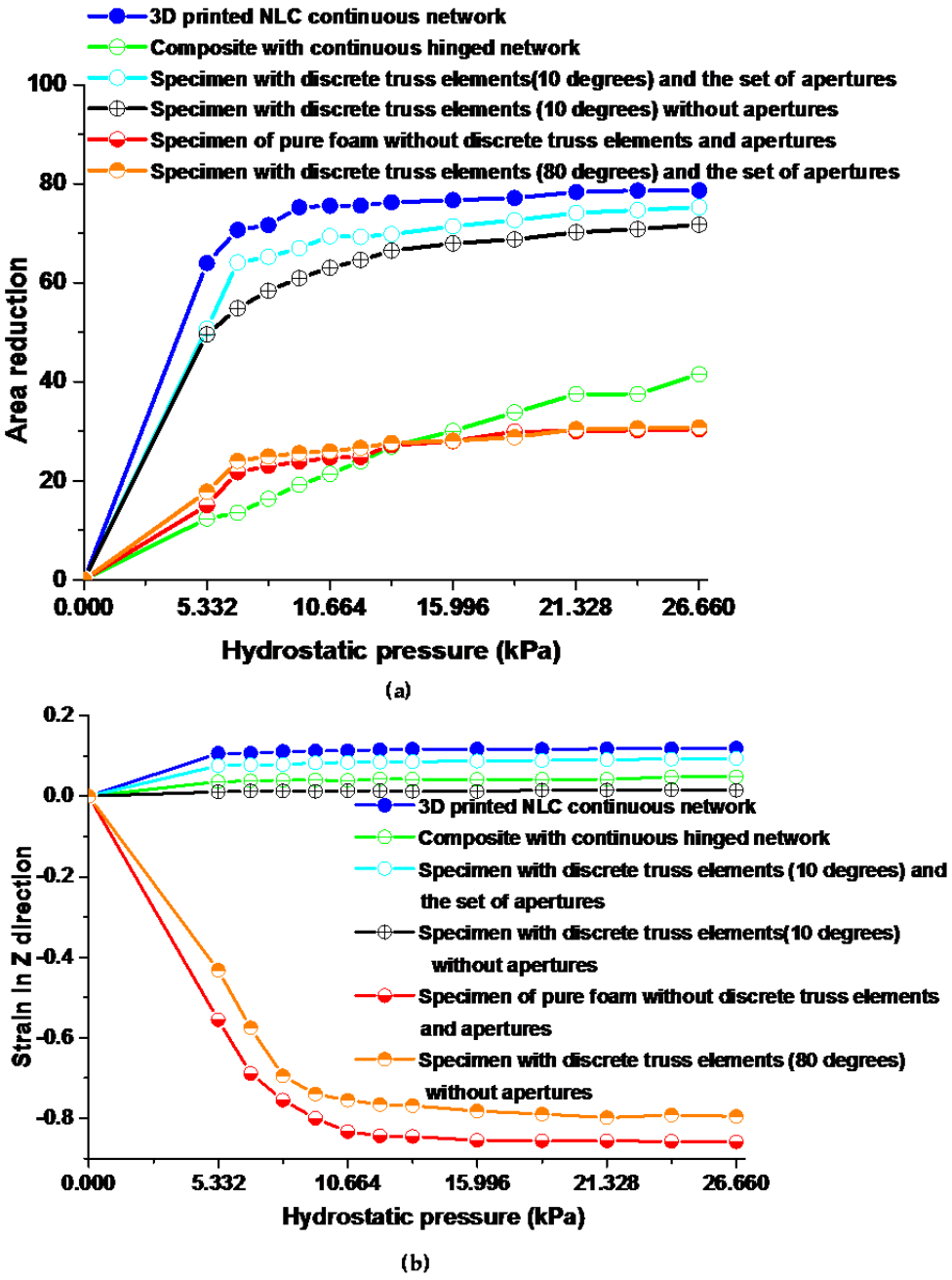

Figure 4-87 Comparison of the behaviour of experimental specimens under vacuum pressure; (a) area reduction–pressure history for experimental specimens under vacuum pressure; (b) strain along Z direction–pressure history for experimental specimens under vacuum pressure.

Experimental results in Figure 4-10 f revealed that the sixth specimens with 80 degrees angled stiffeners did not exhibit NLC property under vacuum pressure. Comparison of strain–pressure history of fifth and sixth specimens indicated that increasing the angle of stiffeners with vertical Z axis led to

changing the mechanism of rotation of stiffeners and losing the NLC propertyThe comparison of area reduction–pressure history of all experimental specimens was presented in Figure 4-11 a. In general, the deformation processes of all samples demonstrated area reduction as a result of in-plane deformation. Therefore, for all specimens except the second one, the majority of area reduction occurred before the vacuum pressure level reached 6.66 kPa. The results indicated that by increasing the vacuum pressure from 6.66 to 26.66 kPa, only minor reduction in width and length was observed as shown in Figure 4-11 a.

This sequence was repeated for the out-of-plane deformation which led to NLC behaviour. Therefore, for all specimens except the third and sixth ones, the majority of strain relating to NLC behaviour was observed in the loading range of 0 to 6.66 kPa and out of this pressure range, the change of nagative strain was minor. This finding was presented in Figure 4-11 b by the corresponding measured strains along Z direction for all specimens.

4.1.5 Estimation of the out-of-plane deformation of NLC composite structure with discrete truss elements based on the specially ordered patterns without apertures

The NLC property of the composite structure with the angled stiffeners was originated from a simple mechanism. The alignment of stiffeners under vacuum pressure caused the compaction of filler components and tensile stresses on the top and bottom surface of the foam. This stress forced each stiffener to undergo rotation to reduce its angle with out-of-plane direction. This rotation led to vertical or height increase of the whole specimen as shown in Figure 4-12.

It should be noted that the plastic cover bag on the top and bottom surface of the composite structure may also contribute to the NLC behaviour of the specimens. A Schematic view of the position of angled stiffeners and the mechanism of rotation was presented in Figure 4-12.

The initial acute angle between the individual stiffeners and the vertical axis of Z could be adjusted to design a composite structure with the expected strain along NLC axis ($\varepsilon_{\mathrm{Net}}$). For this purpose, a simple formula was derived based on simple assumptions. For the sake of simplicity, it was supposed that all stiffeners had the same size, section area, and stiffness. Also, the compressive stiffness of filler materials as compared to stiffeners was negligible. Consequently, the force due to the vacuum

pressure was mostly applied to the stiffeners in equal amounts where P was the applied pressure in Pascal.

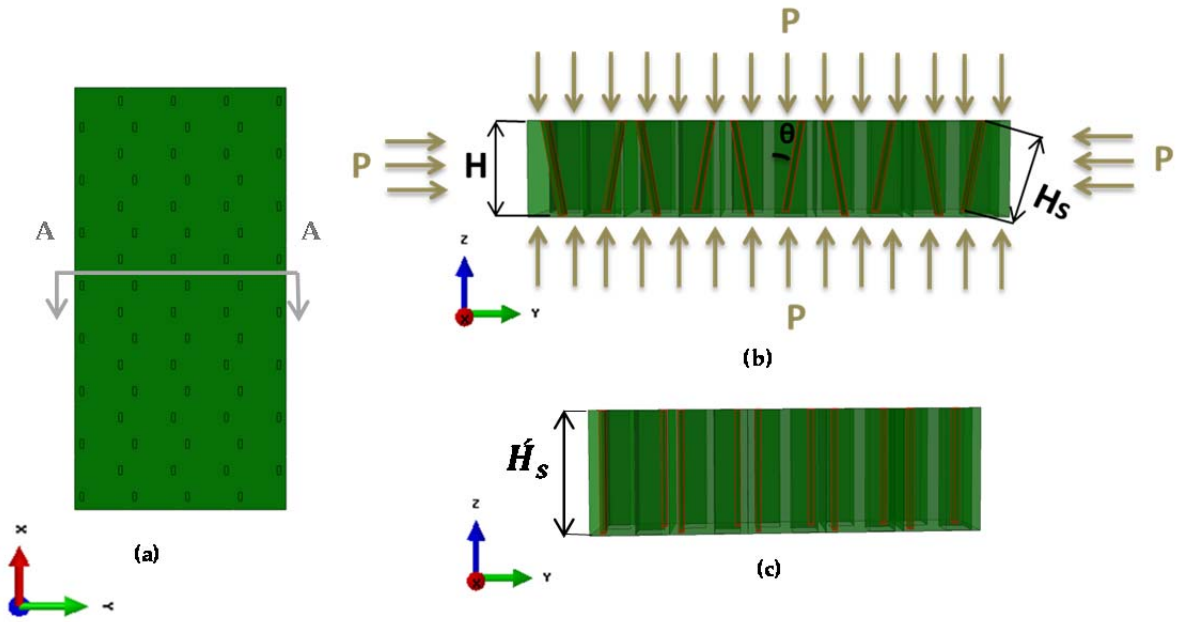

Figure 4-88 Schematic deformation mechanism of stiffener inside the foam under applied vacuum pressure; (a) initial geometric design of the experimental specimen with discrete truss elements without apertures; (b) section A-A from experimental specimen showing the positions of stiffeners and apertures under uniformly applied pressure (P); (c) idealized deformed pattern with stiffeners becoming vertical, resulting in NLC property.

The net strain of composite structure in out-of-plane direction, indicated by z in Figure 4-12, presented the limit of NLC property of new composite structure. This strain was expressed as:

$$\varepsilon_{Net} = \frac{\acute{H}_S - H}{H} \tag{4-2}$$

Where:

$$\acute{H}_S = H_S\,, \qquad cos(\Theta) = \frac{H}{H_S}, \qquad \varepsilon_{Net} = \frac{H_S - H_S\, cos(\Theta)}{H_S\, cos(\Theta)}$$

While in general, the resulting equation was given in Equation 4-3:

$$\Theta = \arccos\left(\frac{1}{\varepsilon_{Net}+1}\right) \tag{4-3}$$

By using this formula, the range of variation of θ for a magnitude of expected strain along NLC axis (ε_{Net}) could be adjusted.

The out-of-plane deformation of the fifth experimental specimen with discrete truss elements with an angle of 10 degrees without apertures was predicted by using Equation 4-3. When θ=10 °, the predicted net strain of specimen with angled stiffeners was about ε_{Net}= 0.015. This estimation represented a conservative estimate of maximum out-of-plane deformation. The average measured strain form Figure 4-10 e is about 0.02 for the fifth specimen that showed an acceptable agreement with the experimental result.

The out-of-plane deformation of the fourth experimental specimen with discrete truss elements and the set of apertures (angle of stiffeners is 10 degrees) was larger than predicted value of formula (ε_{Net}= 0.015) as shown in Figure 4-10 d. It was indicated that the plate specimen underwent a small amount of local wrinkling along the out-of-plane direction of the specimen. It resulted in large measuring errors of strain in the out-of-plane direction. It would be an inherent feature for the specimen with apertures. However, this measuring error would not influence our major conclusion. The sharp difference between the conventional black form and our designed composites confirmed the effectiveness of our design approach.

4.2. Wound filler for negative pressure wound therapy

At the end of most surgical incisions into the abdominal cavity, the abdominal fascia can be closed primarily. However, sometimes full fascial closure is not possible and the operating surgeon is forced to leave the abdomen open. The open abdomen caused mortality rates of 30%. Recently, a greater understanding of intra-abdominal hypertension and abdominal compartment syndrome caused to the development of a great range of surgical and non-surgical measures in an attempt to reduce the number of mortality. Three most commonly results in the commencement of an open abdomen are as follows: 1) Bowel edema which caused by infection, 2) expanded bowel during surgery and 3) increase intra-abdominal pressure in patients with abdominal compartment syndrome (ACS). In These cases, the intra-abdominal pressure persists after the laparotomy, and the surgeon must leave the abdomen open, and the open abdomen requires temporary closure.

Different techniques were employed for temporary abdominal closure. It should be noted that after temporary abdominal closure, the abdominal fascia must be closed primarily. However, many

surgeons instead of primary fascial closure they use mesh and granulation tissue with split-thickness skin grafting to close the abdominal wound. In case of persistent visceral edema, loss of domain, or lateral retraction, the only option is to close the wound with mesh or granulation tissue with split-thickness skin grafting .

As mentioned before for some specific medical applications such as wound management, a specific products with NLC behaviour was required as a wound filler structure. The desired closure deformation of a wound was lateral contraction, without changing the height of the wound. Therefore, a new specific product with NLC behaviour had the possibility to avoid vertical or height deformation of the wound closure arrangement. The NLC behaviour was achieved by using a specific matrix of stiffener elements with specific shapes embedded in crushable foam. In the absence of stiffener elements, the lack of enough stiffness causes that the top and bottom surfaces draw into cavity and height of cavity was greatly decreased. The stiffener elements support at least a middle portion of the cover member above a surface of the wound. When negative pressure was applied to a wound closure arrangement that included the wound filler, the wound filler contracted horizontally with the stiffener elements resisting vertical movement of the wound fill material. It was worth to note that, the other design requirement was providing a separate surface between wound and external region so as to suck out infective fluid from the wound when applying sufficient pressure. It also reduced the swelling size and removed exudates during curing. Therefore, the void size of the filler structure should be in a specific range, i.e. 200-500 micrometres. Due to the manufacturing capacity, it was very difficult to produce a large quantity of NLC materials in metres with such small dimension in its delicate microstructures. A combination of the foam-type material as the filler component and the reinforcement network with NLC behaviour provided a possible solution. In such case, the size of voids of new composite structures was determined by the cell size of the filler material. The reinforcement component played a dominant role in the NLC behaviour of the composite structure.

The final aim of this project was providing a wound closure arrangement which included the wound filler for use in treating a wound with negative pressure, known as negative pressure wound therapy (NPWT). With the development of the projects, seven requirements were identified and added to

maximize the output of this project. Those requirements should be satisfied for our prototype of smart foam for NPWT system. Those requirements are described following:

(1) Required deformation under negative pressure to assist temporary wound closure;

(2) Sufficient wound closure ratio: above 50%;

(3) It can be cut into the shape of the wound with existing medical scissors;

(4) Sufficient size of foam cells for liquid suction;

(5) No adverse effect on patients.

(6) Relatively inexpensive to produce comparing to other existing closure device;

4.2.1. Standard test method for performance testing of the composite wound filler and measurement of wound closure ratio NPWT systems for silicon wound model

In order to investigate the performance of the newly designed wound filler with the NLC property and measurement of wound closure ratio using negative pressure wound therapy (NPWT) systems**,** a standard test method was developed. This test method covered the performance test of new composite wound filler with the NLC property, which would be used to close the open abdomen (OA) with an existing negative pressure wound therapy system. Also, this testing standard covered the fabrication process of silicon wound model, consisted of mixing liquid silicon rubber, molding and de-moulding silicon model, cutting the cavity, Installation of the RENASYS drape, filling foam and installation of vacuum port.This standard did not aim to addressing all of the safety concerns, if any, associated with its use. It was the responsibility of the user of this standard to establish appropriate safety and health practices and determine the applicability of regulatory limitations before its implementation.

4.2.1.1. Terminology

The definitions of terms relating to performance testing of composite wound filler shall be considered as applying to the terms used in these test methods.

a) Millimeter of mercury (mmHg): it was a monomeric unit of pressure, formerly defined as the extra pressure generated by a column of mercury one millimeter high and now defined as precisely 133.322387415 Pascals. It was denoted by the symbol "mmHg."

b) Temporary Abdominal Closure (TAC): it was used to protect the Open Abdomen during the phase of open treatment.

c) Negative Pressure Wound Therapy (NPWT): This technique has the highest fascial closure, and lowest mortality rates compare to other technique. Because of its relative ease of application, and preservation of fascial tissue, NPWT is becoming a dominant choice for TAC in the open abdomen patient.

d) RENASYS◊ EZ Plus: Negative pressure device that provided a solution for high volume output wounds while still offering flexibility in treating a variety of acute and chronic wounds. This machine was made by Smith&Nephew Company and was perfectly straightforward controlled for easy operation. The range of pressure control was between 40 to 200mmHg, and the weight was around 7.4lbs/3.3kg

e) Negative Pressure: It was a relative pressure value below atmosphere pressure which was 760mmHg.

The composite wound filler test provided information on the performance of wound filler quantified by the closure ratio of wound model under negative pressure. This information may be useful in wound filler development, quality control, and design under certain circumstances. These test methods were considered satisfactory for acceptance testing of commercial shipments and have been used extensively in the trade for this purpose.

4.2.1.2. Apparatus

In order to assess the performance of existing composite (wound filler), and also for the purpose of designing and validating new cellular metamaterials with appropriate stiffness and deformation capability, a silicon wound models was fabricated. The suggested material was a “Polymould 10 A RTV2 Flexible” by a local company “Polymech”. The product consisted of two components. One was the silicon mold making rubber, and the other was a clear silicone catalyst as shown in Figure 4-13.

A plastic container with suitable size was used to make the wound model, which is approximately 240×300×45 mm^3 (length×width×depth) (see Figure 4-13). Before molding, the internal surfaces of the container were covered by cling film to provide a light, non-toxic layer, which was colourless,

odourless and tasteless. This non-toxic layer did not attract dust or dirt, making it suitable for lubrication and molding. The ratio of the mixture (silicon rubber to silicon catalyst) was 100:2 by weight. The accurate weights of both components were measured by a digital scale, and the mixture of the two components was casted in the container. The normal de-moulding time at room temperature (25 °C) was approximately 5 to 6 hours.

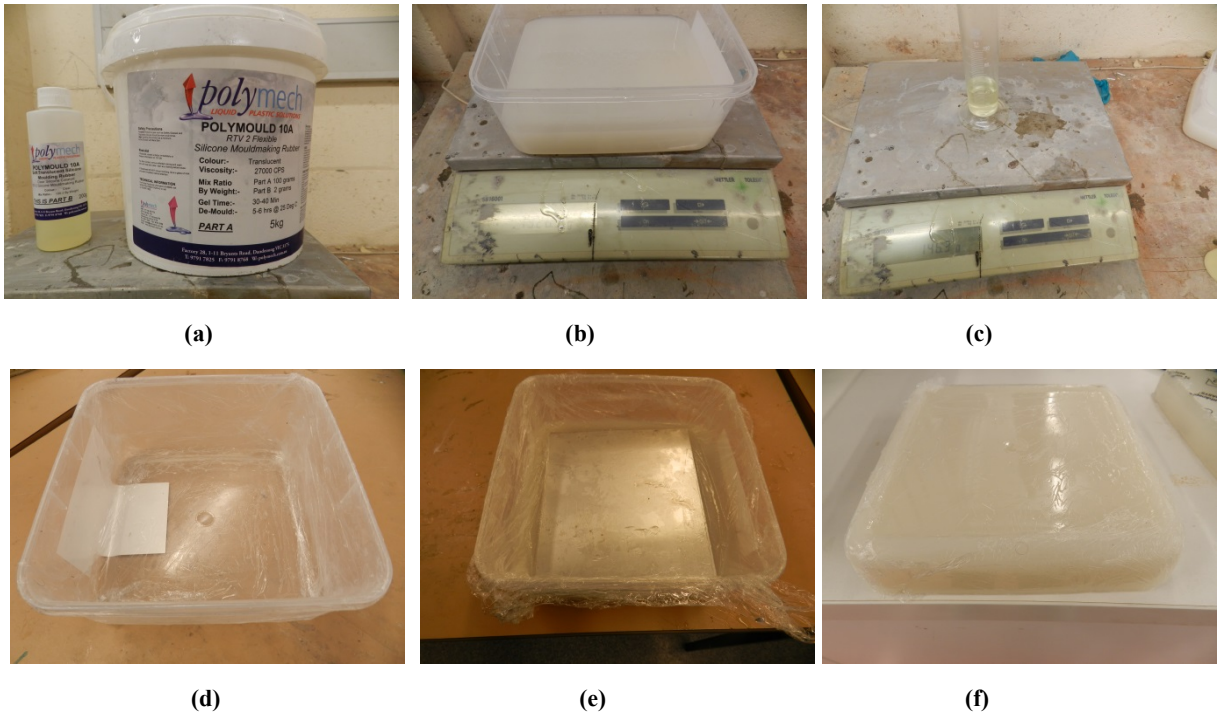

Figure 4-89 Fabrication process of silicon wound model; (a) the Liquid silicon rubber (Polymould 10A RTV2 Flexible) the ratio of mixture (silicon rubber to silicon catalyst) was 100:2 by weight; (b) weight measurement of silicon rubber; (c) weight measurement of silicon catalyst; (d) covering internal surfaces of the container with cling film; (e) laying a weight on the silicon block during de-moulding; (f) de-moulded silicon block.

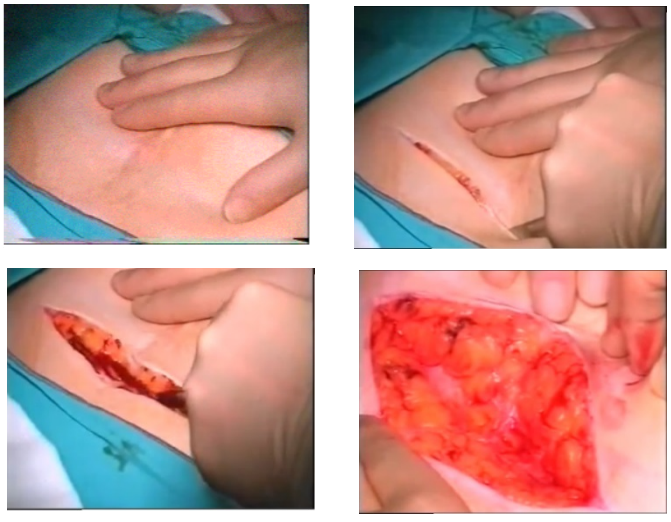

Figure 4-90 The real process of a surgical cut.

The real process of a surgical cut consists of the finding an appropriate location to cut, cutting across the abdomen, cutting across the abdomen, and opening the wound as shown in Figure 4-14.

Accordingly, to a real case of surgical practice, a method was proposed to cut the cavity from the silicon mimetic wound as illustrated in Figure 4-15. Firstly, a straight line was drawn, which was assumed to represent the mean length of the wound. Secondly, the silicon block was cut along the line as shown in Figure 4-15 b. In order to find an appropriate wound shape similar to real case, both the edges of the wound were pulled by hand which presents in Figure 4-15c.

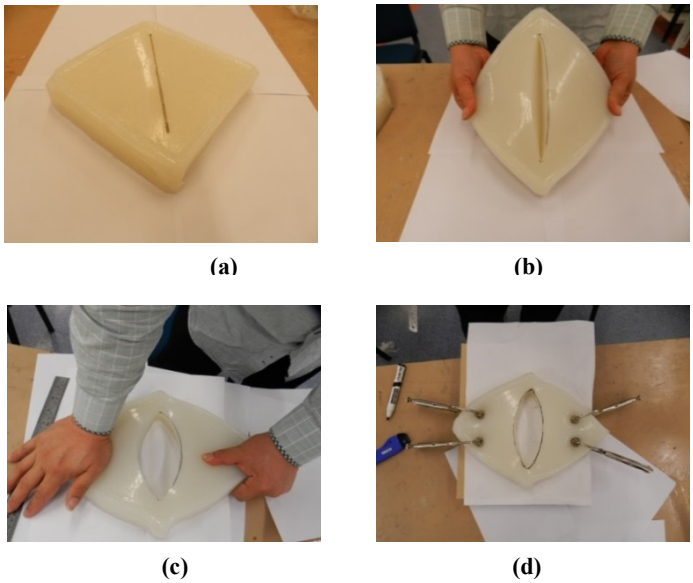

Figure 4-91 New method to cut the cavity with appropriate shape from the silicon block; (a) drawing a straight line which represents the length of the wound; (b) cutting along the straight line; (c) pull the edges of the wound apart to identify the appropriate shape and size of the mimetic wound; (d) finding a template for cavity.

Once the shape was found, four corners of the torn silicon mimetic wound were fixed using the clamps as shown in Figure 4-15 d. The appropriate wound shape was therefore identified and recorded n a template (see Figure 4-15d), which was used to cut the cavity in the silicon block.

It should be noted that the cavity shall be fully penetrated without leaving any silicon in the cavity region. Figure 4-15 represented a final shape of the mimetic wound. It was evident that the closure pattern of this wound was similar to the real surgical one. When applying pushing force, it can be closed perfectly as shown in Figure 4-15 b. The dimensions of this cavity were presented in Figure 4-16. It can be used as a template to cut the cavity inside silicon wound model and cutting smart foam in the appropriate size.

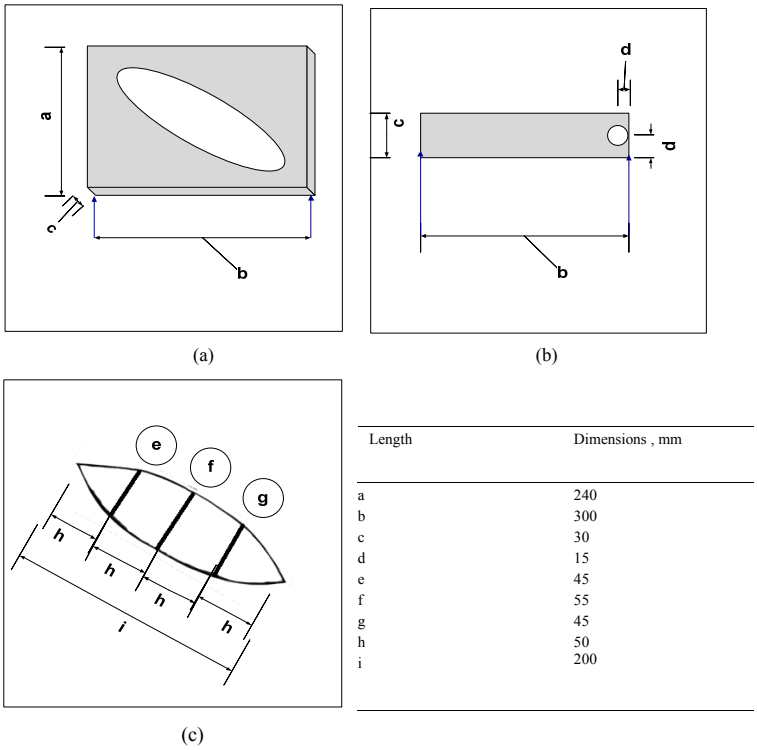

Length	Dimensions , mm
a	240
b	300
c	30
d	15
e	45
f	55
g	45
h	50
i	200

Figure 4-92. (a) Schematic view of silicon wound model and the position of the elliptical cavity inside it; (b) front view of silicon wound model the position of the hole to place plastic connector; (c) dimensioned template for making the cavity inside the wound model.

Figure 4-93 Orange plastic connector of RENASYS soft port.

In the next stage, an elliptic cavity was cut through into the cylinder silicon wound model as presented Figure 4-16. bA small hole with a diameter of 10mm was made at the position as shown in Figure 4-16. The size of this hole shall be slightly smaller than orange plastic connector which is shown in Figure 4-17. The orange plastic connector was removed from RENASYS soft port and was placed inside the mentioned hole. This plastic connector bridged the plastic wound model to RENASYS◊ EZ Plus machine.

Machines used for performance testing shall conform to the requirement of practices. The pressure used in the smart foam performance test shall be within the verified force application range of the testing machine as defined in Section 4.2.1.1.

Made of soft plastic tubing, cushioned channel RENASYS Soft Port allowed for the same application technique to a variety of wounds, including direct application to the most difficult-to-dress body areas without the need for bridging.

The dressing was applied to the top and bottom of wound model and covered with a transparent film. The therapy device then draws excess air from the wound into the canister. In realty the transparent film helps to prevent bacteria from entering the dressing. It may also improve blood flow to the wound via the vacuum which will help it to heal.

4.2.1.3. Procedure.

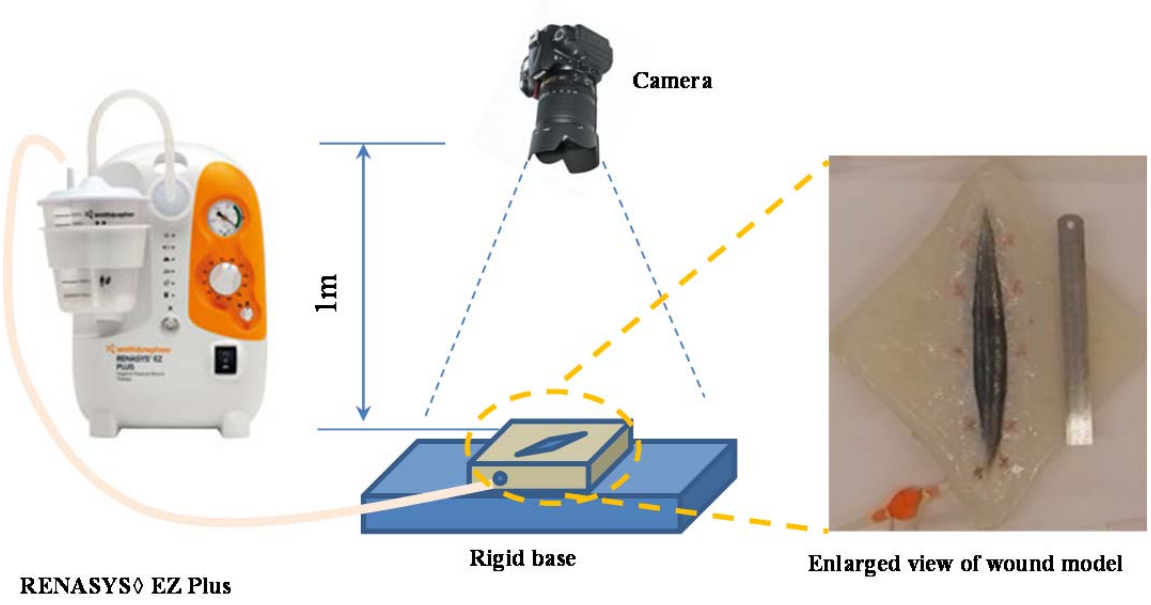

Figure 4-94 Experimental set-ups.

a) Experimental setup: The experimental set-up was illustrated in Figure 4-18. The deformation process of smart foam inside the wound model and under negative pressure was captured by using a digital camera. The position of the camera was a major constraint in the image capturing and projected output that directly affects the efficiency and accuracy. The camera was fixed above of the working table in a vertical position so that the silicon wound model was kept in the field of view of

the camera during the experiment. The orange plastic connector which was placed inside the wound model was connected to negative pressure machine to apply different pressure on smart foam.

b) Sample preparation and assembly (including the method we used to increase the contrast between the wound surface and the cut surface): In this step, the smart foam was cut to match cavity and placed inside it. As mentioned before, the dressing was applied to the top and bottom of wound filled with two layers of transparent adhesive film. The RENASYS transparent adhesive film consisted of two layers, i.e. the top protective layer, which was to be removed, and the adhesive bottom layer, which was attached to the top and bottom surfaces of wound model to cover the cavity. The bubbles of air must not be remained under the adhesive layer and should be removed perfectly. Eventually, the silicon wound model with a smart foam prototype filled in was connected to the RENASYS negative pressure pump. The deformation of the prototype under different negative pressures was presented in operation; the negative pressure device sucks out the air from the inside of the cavity. The experimental results of the silicon wound model were influenced by the effect of friction between the bottom surface of silicon model and contact patch. To reduce the effect of this external parameter, the silicon model must be left on the smooth surface to do the test.

c) Calibration of area measurement: One camera captured the deformation process. When images either were acquired from a digital camera, the images were not scaled for one-to-one (1:1), life-size output. Pictures were taken with a camera (film or digital) involve variable distances from lens to object. Using Adobe® Photoshop®, photos accurately any image can be calibrated. For this purpose, the first step was the counting of the number of pixels from one known area on the scale. In the next step, two numbers were compared together to find the nearest known area on to unknown area and then counting the number of pixels from one unknown area on the image thus determining the number of pixels per square mm for resolution.

The blue, white, black squares areas and red circle area in Figure 4-19 were used as the known areas or the calibration border of the image processing procedure. This calibration border was printed on paper then this border left on the top surface of silicon wound model. The first photo was taken

from above of silicon model, after that the calibration board was removed and another photo was taken without changing the position of the camera.

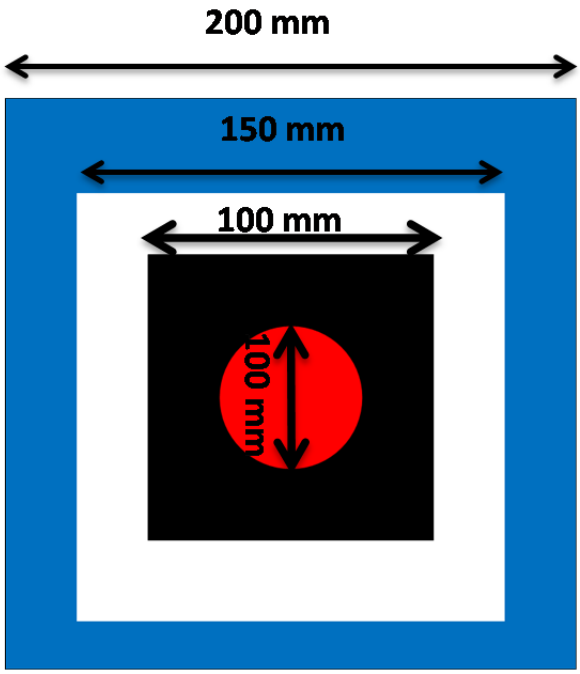

Figure 4-95 Schematic view of calibration board.

By using Adobe® Photoshop, the pixel numbers of the colour areas were counted separately from the first photo as the pixels numbers of known areas. Also, the number of pixels corresponding to cavity part was counted from the second photo as the pixels number of the unknown area as illustrated in Figure 4-19. The closest pixel number among known areas to the unknown area was chosen and divided by its area per square millimeter.This number represented the number of pixels per square mm for resolution. Thus all unknown areas can be estimated by using this new ratio and also counting the pixel number of unknown area.

d) Testing closure ratio at different pressure: The performance of smart foam was considered in the range effective pressure from 40 mmHg to 200 mmHg. In this range, the pressure increased step by step and was fixed at 50 mmHg, 60 mmHg, 70 mmHg, 80 mmHg, 90 mmHg, 100 mmHg, 120 mmHg, 140 mmHg, 160 mmHg, 180 mmHg and 200 mmHg. A photo was taken from above of test specimen 30 seconds after the pressure was applied. The experimental values of closure' ratio were calculated through image processing by using the Photoshop software. In the calibration process, a

measurement scale was set at a specified number of pixels in the image, which was equal to a known area per square millimeteras shown in Equation 4.14. Once a scale was created, the wound area of each photo corresponding to different pressures was tracked to find the exact number of pixels. After this step, the unknown wound areas was calculated by using the Equation 4-15,

$$\text{Number of pixels per mm}^2 = \frac{\text{The closest pixel number among known areas to the unknown area}}{\text{known area (mm}^2\text{)}} \quad (4\text{-}14)$$

$$\text{Unknown area} = \frac{\text{Number of pixels of unknown area}}{\text{Number of pixels per mm}^2} \quad (4\text{-}15)$$

The most important aim of this test was to find the closure ratio corresponding to different pressures. The wound closure ratio at each pressure was calculated by using Equation 4-16.

$$\text{wound closure ratio} = \frac{(\text{Initial area of wound} - \text{area of wound under specific pressure})}{\text{Initial area of wound}} \quad (4\text{-}16)$$

4.2.2. Design and fabrication of smart composite as the wound filler

4.2.2.1 Inspiration of design approach

A set of experimental tests were conducted to confirm that increasing the vertical stiffness of the wound closure arrangement led to desired wound deformation which was similar to lateral contraction without changing the height of the wound.

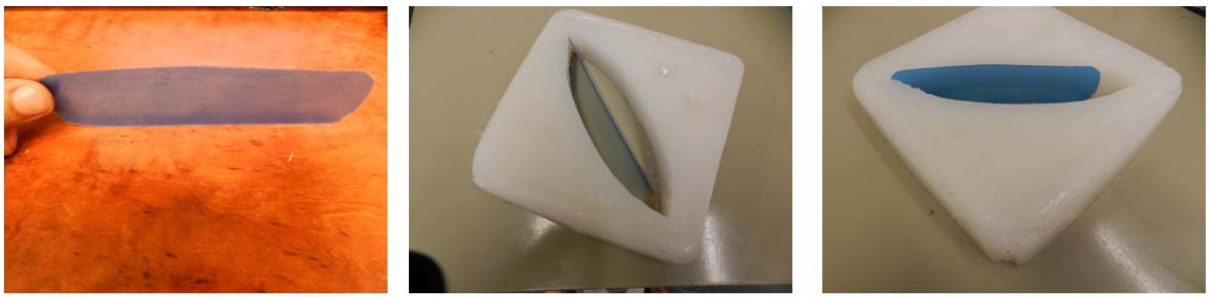

(a) (b) (c)

Figure 4-96 using a stiff plate to avoid uncertain deformation into the cavity; (a) stiff plate; (b) stiff plate placed in the cavity of wound model; (c) stiff plate placed in the cavity of wound model from top view.

For the newly fabricated mimetic silicon wound, installation of the cling film, prototype, cover drape, and vacuum port were exactly based on the proposed standard. Figures 4-20 and 21 show a wrapped silicon wound with a stiff plastic plate sitting vertically inside the cavity of mimetic wound

prior and after to the application of negative pressure. The stiff plate was placed inside the wound to mimic the stiffness of wound filler of the present invention parallel to the walls of the wound. The negative pressure pump was set to produce a vacuum level of 100 mmHg on this test. According to test results, closure of wound model was completed and the height of wound maintained constant under negative pressure. In the next step, the newly fabricated silicon wound was used to test the performance of a pure black foam under negative pressure. The prototype material (pure black foam) was cut to match the cavity and was filled into the wound cavity. The installation methods of cling film, prototype, cover drape and vacuum port were the same as previous test. The deformation pattern of silicon wound filled with black foam was shown in Figure 4-22 in NPWT process.

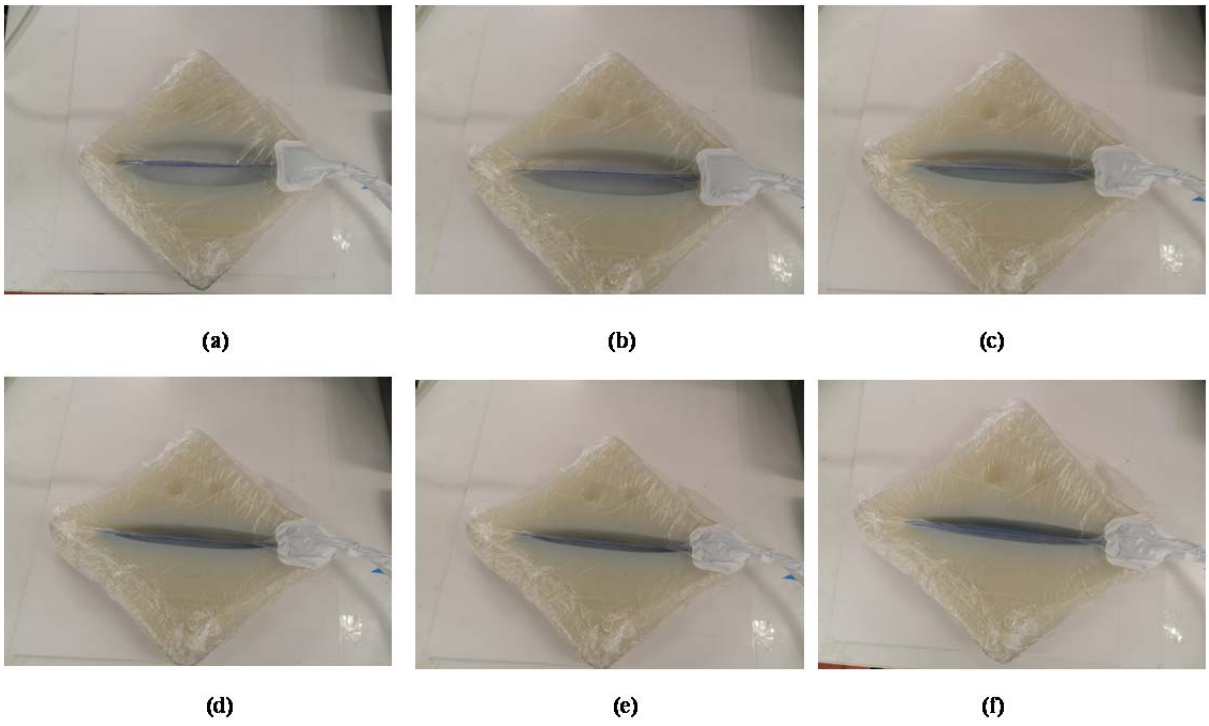

Figure 4-97 Closure mechanism of newly designed mimetic silicon wound with stiff plate placed inside the cavity under the negative pressure; (a) applied pressure 0 mmHg; (b) applied pressure = 40 mmHg; (a) applied pressure =50 mmHg; (a) applied pressure =60 mmHg; (a) applied pressure =80 mmHg; (a) applied pressure = 100 mmHg.

In contrast to the previous test, the closure mechanism of silicon wound model was not complete under NPWT, and thus the wound could not be closed. The observed closure pattern in this test reveals that the pure foam under NPWT system did not have desired performance to close the wound. The top and bottom sides of silicon wound model drawn inside the cavity and height of wound were changed under negative pressure.The comparison of the test results evident that the most important

desired and required property of new smart wound filler shall be equivalent stiffness to avoid deformation in an uncertain direction. Regarding the black foam, the lack of enough stiffness caused that the top and bottom surfaces draw into the cavity and the height of wound was changed, and therefore the wound was not closed.

Inspired by this finding, it was concluded that a specific product with NLC behaviour as the wound filler led to the desired closure deformation of a wound which is lateral contraction, without changing the height of the wound.

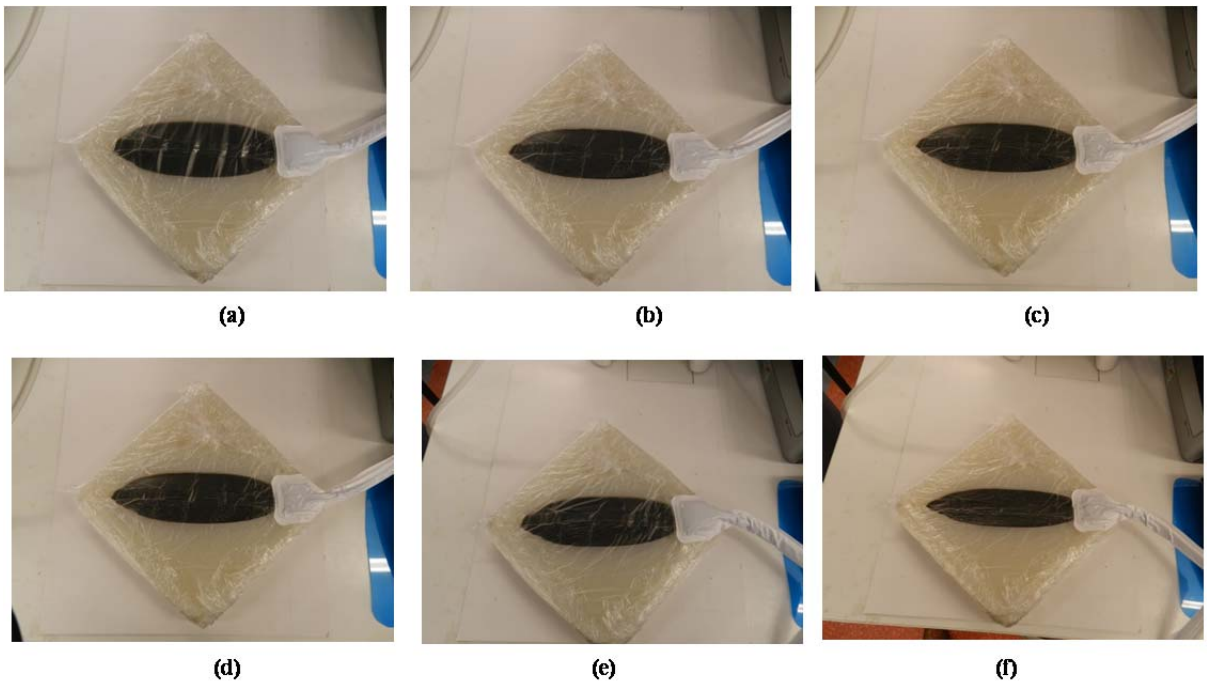

Figure 4-98 Lack of closure of the wound model when the black foam was placed inside the cavity under the negative pressure; (a) applied pressure 0 mmHg; (b) applied pressure = 40 mmHg; (a) applied pressure =50 mmHg; (a) applied pressure =60 mmHg; (a) applied pressure =80 mmHg; (a) applied pressure = 100 mmHg.

4.2.2.2 Fabrication of composite wound filler with NLC behaviour

The initial design of the newly fabricated wound filler was originated from the new design approach for designing the NLC composite structure with discrete truss elements (which was presented in Section 4.2.????). It was fabricated through adding several stiffeners to black foam to maintain the vertical height of the wound filler. Moreover, a specific matrix of vertical voids was added to the black foam to counteract the negative effect of stiffeners on closure ratio. The innovative feature of this improvement was the addressing of arrangement of matrix stiffeners and a specific matrix of

voids to improve the function of the new design of wound filler as compare to previous products and enhancing the closure ratio.

In this configuration, the newly fabricated wound filler for use in treating a wound with negative pressure comprises:

• A block of original black foam;

• A specific matrix of stiffeners with specific shapes;

• A specific matrix vertically voids configured to counteract the negative effect of stiffeners on closure ratio.

The newly wound filler for NPWT system was designed to satisfy the following requirements:

(1) Desirable deformation under negative pressure of lateral contraction, without contraction in the height of the wound filler;

(2) Sufficient wound closure ratio of preferably above 50%. Ideally, the closure ratio should be the larger, the better and the closure ratio can be linearly controlled by the applied pressure. The minimum requirement is preferably 50% under the pressure of 120 mmHg;

(3) Inexpensive to produce; and

(4) Easy to cut, shape and end user-friendly.

Foam was one of the best dressings which has been used in wound management and became for lightly, moderately or heavily exuding wounds. Foams offered advantages over traditional gauze dressings as they did not shed particles and could be left in place for several days without causing maceration.

The foam had the properties of such a dressing as the ability to: (1) Remove excess exudate and toxic components; (2)Maintain high humidity at the wound/dressing interface; (3) Permit gaseous exchange; (4) Provide thermal insulation; (5)Protect from secondary infection (6) Protect from particulate or toxic contamination (7) Allow removal without trauma at dressing changes. Today, foam dressings were available in various forms. Topical wound dressings came in a range of sizes and as sheets, with or without adhesive borders. Foam dressings were available for cavity wounds and

were used as a dressing medium in negative pressure wound therapy (V.A.C.® Therapy, KCI; RenasysEZ, Smith & Nephew).

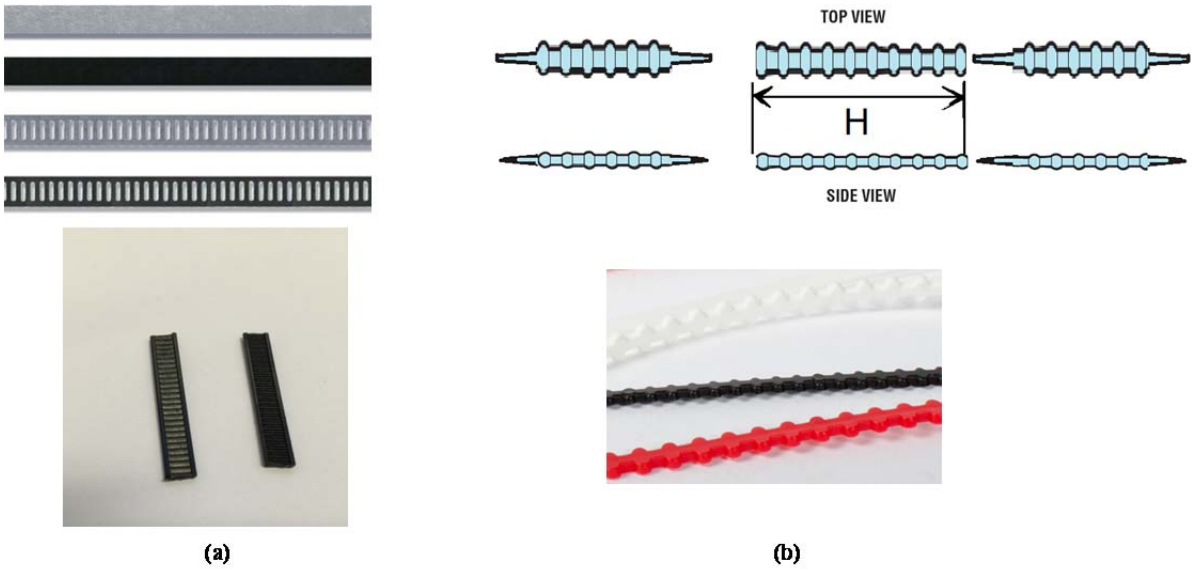

Figure 4-99 Different designs for the shape of stiffeners.

About stiffeners, it should be mentioned that the, the shape of stiffeners was specially designed to increase the bond between the stiffeners and the black foam. Two different designs were invented as illustrated in Figure 4-23. The material of the stiffeners was plastic in the current design and could be other materials with medical grade and enough stiffness (>80 kPa). The designed shape in Figure 4-22 could be simply inserted into the black foam. Also it should be further bonded with the black foam using special glue which was identical to the glue used in the cling film provided by Smith & Nephew. The friction between the stiffeners and the black foam provided enough force to prevent relative sliding between them. The material of the stiffeners was plastic in the current design and can be other materials with medical grade and enough stiffness (>80 kPa).

Stiffener elements could be positioned in any suitable two-dimensional pattern across the width and length of the wound fill material. It was noted that the stiffener elements are positions in a two-dimensional array or across the width and length of the wound filler. Some different arrays were possible, including (but not limited to) honeycomb pattern, a triangular pattern, a Kagome pattern, or rhombi trihexagonal pattern.

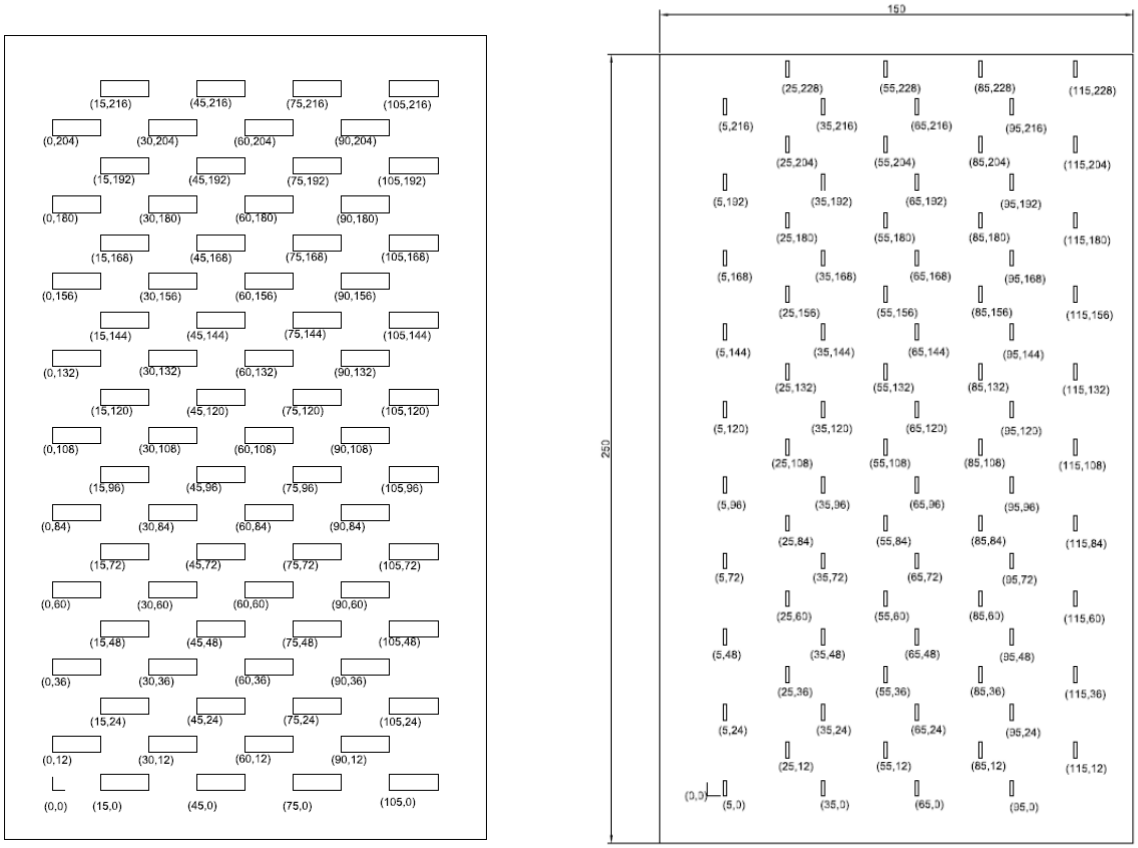

(a) **(b)**

Figure 4-100 Example complementary arrays of apertures and stiffener elements; (a) top view of the matrix of stiffener elements; (b) top of view of the matrix of apertures.

Regarding the filler materials (foam) it was worth to note that to improve wound closure ratio, a softer and more compressible porous wound fill material could be selected or the construction/ configuration of the wound filler could be modified. Accordingly, the wound filler further included a plurality of apertures extending through the wound fill material between the inner side and outer side of the wound fill material, the apertures arranged about the stiffener elements across the width and length of the wound fill material in a complementary pattern to the two-dimensional pattern of stiffener elements. The apertures assist in horizontally contraction/ compression of the filler material. The apertures were preferably positioned in the wound fill material between the stiffener elements to facilitate lateral movement of the stiffener elements towards each other upon lateral compression of the wound fill material. Thus, lateral compression of the wound filler was enhanced when the wound filler was positioned within a wound bed under negative pressure.

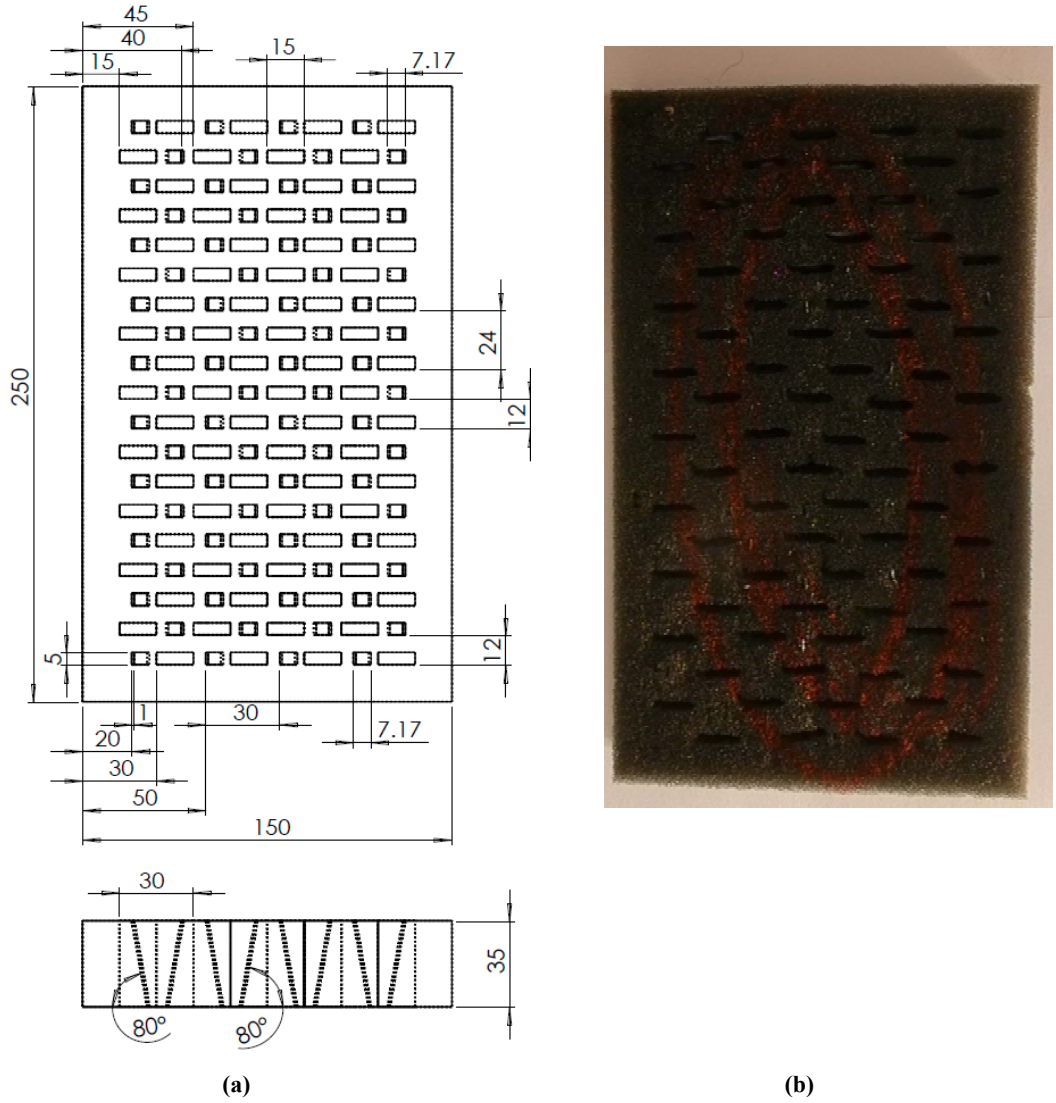

Figure 4-101 (a) The combined matrix of the complementary array of apertures and stiffener; (b) the wound filler prototype.

Figure 4-24 illustrates one example complementary array of apertures and stiffener elements which achieves the required deformation pattern and to achieve prescribed closure ratio described above. Figures 4-24 a and 4-24 b show the respective top view of the matrix of stiffener elements and a top of view of the matrix of apertures. The positions of apertures and stiffener elements were defined by guideline coordinates.

The combined matrix was shown as a top view in Figure 4-25 a and cross-sectional front view (across the width of the wound filler) in Figure 4-24 b. The cross-sectional view illustrated the angled placement of the stiffener elements (80 degrees from the horizontal or 10 degrees from the vertical) within the wound filler when using the matrix shown in Figure 4-25 a.

A new wound filler specimen was fabricated based on the complementary array of apertures and stiffener as shown in Figure 4-25 b. The dimensions of the specimens were selected according to the availability of existing conventional foam. As discussed in the Section 4.1.3, the hot wire cutting technique was employed to make some slits for housing the stiffeners inside the foam. The apertures were cut in a similar manner.

4.2.3 Testing the performance of new wound filler under negative pressure

For testing the performance of newly fabricated wound filler, the prototype of composite wound filler was cut to match the cavity as shown in Figure 4-26 and was filled in the cavity of the plastic wound model. The installation methods of cling film, prototype, cover drape and vacuum port were the same as previous tests as illustrated in the test protocols in Section 4.2.1.4.

(a) **(b)**

Figure4 -102 Cutting process of specimen.

The position of wound filler into the cavity of the silicon wound model was similar the real case when the newly fabricated wound filler was positioned within a wound bed as shown in Figure 4-27. The abdomen wound had a longitudinal direction which followed the length of the wound, a horizontal direction which was generally perpendicular to the longitudinal axis whichdefined the direction of desired closure of the wound and the vertical axis which defined the depth of the wound

within a patient. A wound filler was placed within a wound such that the edges of the wound surround and contact the edges of a wound closure arrangement which include the wound filler.

The wound filler was used in a layered structure in a wound (for example abdominal wound) where the wound filler was placed between a wound bed layer which contacted the wound and a wound cover layer which extended over the top of the wound filler.

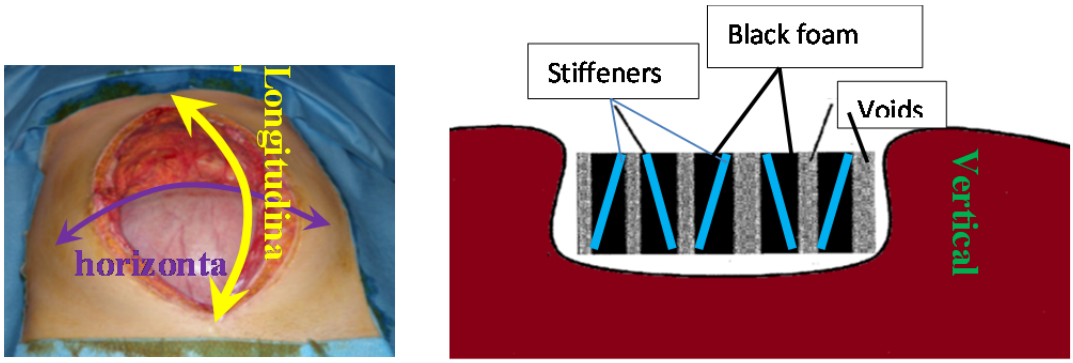

Figure 4-103 Illustration the position of a wound filler for temporary wound closure using NPWT and the definition of directions used.

Figures 4-28 shows a wrapped silicon wound with a newly fabricated wound filler sitting vertically inside the cavity of mimetic wound prior and after to the application of negative pressure. The negative pressure pump was set to produce a vacuum level of 200 mmHg on this test. According to test results, closure of wound model was completed and the height of wound maintained constant under negative pressure. It can be seen clearly that the pattern of the reinforcement stiffeners had the significant effect on the closure performance of wound under negative pressure.

The application of negative pressure caused that the wound filler contracted horizontally with the stiffener elements which avoided the vertical movement of the wound fill and the apertures assisting contraction/ compression of the wound filler horizontally. The net pressure on the wound filler was the combination of the pressures induced by negative pressure and the forces from the wound bed and wound cover surrounding the wound filler. As shown in Figure 4-28 b when negative pressure was applied to normal (or expanded state), loading of the wound filler was from the wound bed below, the wound cover above and the wound edges from the side. Figure 4-28 c shows the configuration of the wound filler in a compressed state, i.e. when compressed by the forces.

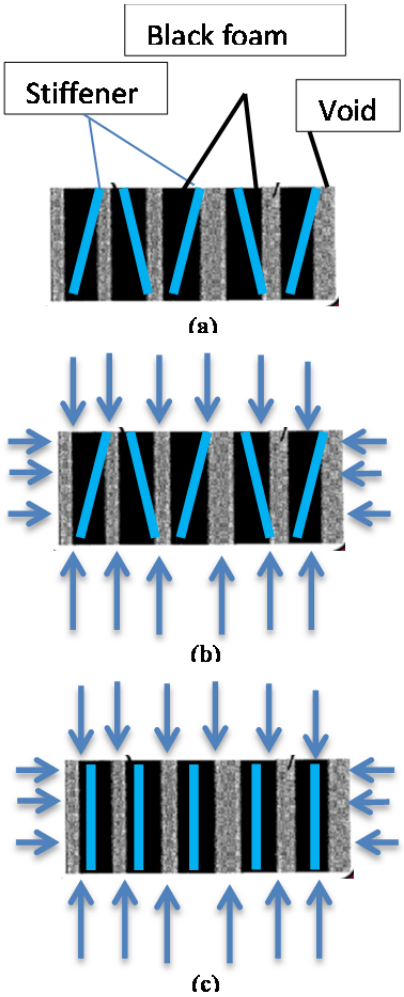

Figure 4-104 Illustration of the position o

The closure ratio of the silicon wound filled with the pure foam, supporting stiff plate, and the newly composite wound filler were compared together in Figure 4-29. It should be noted that the closure ratio of the newly designed wound filler satisfied the requirement for wound closure using NPWT system though it was lower than only one supporting plate inserted in the middle of the wound. It is also worth noting that the variation of closure ratio between 50 mmHg and 200mmHg was larger than 40%.

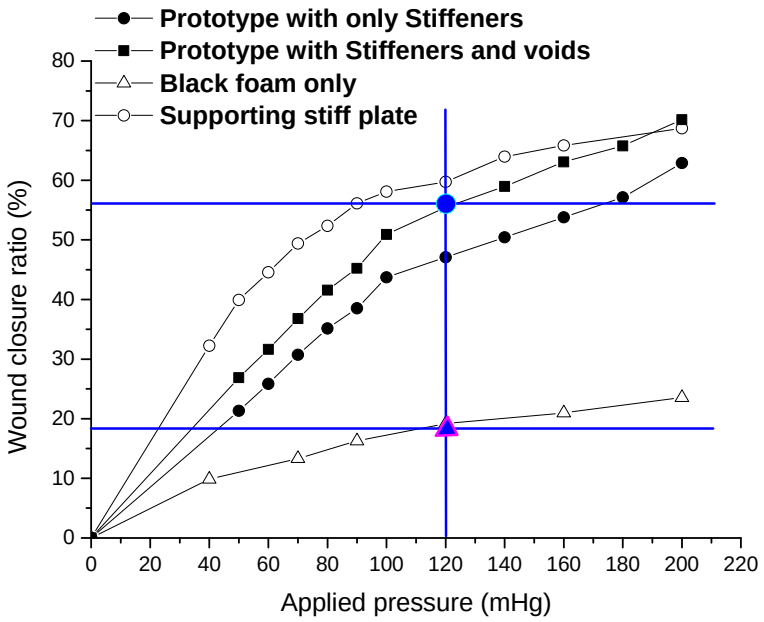

Figure 4-105 The variation of closure ratio of wound with this smart foam under different negative pressure.

4.3 brief conclusions and discussions on designing composites with negative linear compressibility

This section of study demonstrated the effectiveness of two proposed approaches to designing new composite structures with negative linear compressibility (NLC). The first approach was to simplify the topology optimization results from previous research [20] to generate a continuous framework for a new NLC composite structure. The second approach was to use discrete truss elements of a special pattern to reinforce the crushable foam for generating a new type of NLC composite structure. Those two design approaches have been validated by experiments. The key performance of designed NLC composite structures was captured under the application of different levels of vacuum pressure. From the obtained results, the following conclusions can be drawn:

- The new designed composite specimens exhibited NLC behaviour in the out-of-plane direction and had a significant area reduction in the in-plane directions. Those results proved the effectiveness of our design approaches.
- The results of experiments confirmed that the NLC behaviour of the designed composite structures depended on three main factors: the compressibility of the filler foam, the pattern of

the network element, and the stiffness ratio between the two constituent materials of the composites.

- The modification of filler foam through embedding some vertical apertures led to larger in-plane deformation and enhanced NLC property. The in-plane deformation of the NLC composite structures could be tuned by the shape and the pattern of the apertures to meet specific compressibility requirements.
- A simple formula was derived to guide the adjustment of the angle of the stiffeners so that the strain along the NLC axis would reach a desired magnitude.

It should be noted that the aim of our experiments is to qualitatively confirm the effectiveness of our design approaches to achieve NLC rather than precisely measure the material properties for the designed and manufactured composite materials. The shape of the specimens was selected as a rectangular plate due to their intended applications in which the in-plane area contraction ratio and out-of-plane deformation are the major factors. It is also worth noting the limitations of the present study. Firstly, the in-plane and out-of-plane deformations of NLC composite specimens were not uniform. Secondly, much of the area reduction occurred at the lower levels of vacuum pressure except for the second specimen with continuous network and filler foam, and the in-plane deformation was minor at the higher levels of negative pressure. Thirdly, the increase of stiffness of the crushable foam led to a reduction of the in-plane deformation and weakening of the NLC effect. These issues will be addressed in the subsequent research.

Chapter 5

Conclusions

Previous studies on engineering system desings at the macrostructural level have clearly indicated the advantages of optimisation or applying creativity to manipulation of materials and apply mathematical and scientific ideas to achieve desired products and satisfy the design performance objectives. Moreover, in the design of materials through applying creativity, it has been shown that the best topology for an engineering system can be achieved to exhibit tuneable exceptional uncommon properties when the system is subjected to disturbances of external factors such as changes in temperature or applied strain. The primary objective of this study was to open a pathway toward applying the creativity for the topological design of materials microstructures with two uncommon properties of negative linear compressibility (NLC) and negative Poisson's ratio (NPR). Upon the successful accomplishment of the primary objective, the methodology was extended into various material design scenarios.

The literature on several structural topology design methodology that have already been used for the design of materials microstructures has been critically reviewed. Moreover, as the process of material design usually involves the application of material modeling techniques, some of these

techniques are briefly surveyed. Applications of materials with NLC in the design of wound fillers for negative wound therapy system have been addressed.

In the first stage, development of auxetic metamaterial based on functionalization of base materials and topologies were described. The geometric limits for buckling-induced auxetic metamaterials have been identified at both infinitesimal and finite strain. The previous investigation on buckling-induced auxetic metamaterial revealed that there is a geometric limit for its microstructure to exhibit auxetic behaviour in infinitesimal deformation. However, the limit for auxetic metamaterials undergoing large deformation is different from that under small deformation and has not been reported yet. Thus the geometric limit was investigated in an elastic and infinitesimal deformation range using linear buckling analysis. At finite deformation range, experimentally validated finite element models were used to identify the geometric limits for auxetic metamaterials. Depending on the controlling parameters of the topology, the bounds were represented by a line strip for one control parameter, an area for two control parameters and spatial domain surrounded by a 3D surface for three parameters. It was found that there was a significant difference in the geometric bounds at different deformation level. This difference was critical to design auxetic metamaterials for different applications and to control their auxetic performance.

Next, the special features of metallic auxetic metamaterials were identified and investigated as the new class of auxetics. A fundamental way was proposed to design a new class of 2D metallic auxetic metamaterials. The new design approach consisted of two important improvements compared with the previous approach for elastomer. The first improvement was the inclusion of a geometric modification of the conventional structure to generate a new buckling-induced metamaterial. The second improvement was altering the initial geometry of a non-metallic auxetic metamaterial at the RVE level. The FE models were validated by experiments. A systematic parametric study was carried out using validated FE models on the effects of the plastic properties of the base material and the pattern scale factor.

Thereafter, two new methodologies were developed to designing new NLC composite structures. This section of study demonstrated the effectiveness of two proposed approaches to designing new

composite structures with NLC. The first approach was to simplify the topology optimization results from previous research [20] to generate a continuous framework for a new NLC composite structure. The second approach was to use discrete truss elements of a special pattern to reinforce the crushable foam for generating a new type of NLC composite structure. Those two design approaches have been validated by experiments. The key performance of designed NLC composite structures was captured under the application of different levels of vacuum pressure. These investigations have clearly demonstrated the feasibility and effectiveness of designing and manufacturing of mechanical metamaterials using the presented approaches and laid the foundation for the expansion of their potential applications

Finally, the results of this research work were applied in filling materials for negative pressure wound therapy system. For some specific medical applications in wound management, the pore size of filling material was required to in the range of 200-500 micrometers. This pore size will facilitate the transmission liquids. By using our approach, the size of voids of new designed composite structures was determined by the cell size of the base material which was available and easy to manufacture such as conventional black foams in this study, while the NLC behaviour was dominated by the reinforcement component. The developed composite structures are under further assessment aiming to deploy the next generation of superior negative pressure wound therapy system for open abdomen wound closure.

References:

1. Singh, G., Rajni, and A. Marwaha, *A Review of Metamaterials and its Applications.* International Journal of Engineering Trends and Technology, 2015. **19**(6): p. 305-310.
2. Weiglhofer, W.S. and A. Lakhtakia, *Introduction to Complex Mediums for Optics and Electromagnetics*. Vol. PM123. 2003, Bellingham, WA, USA: SPIE Press. 776.
3. Babaee, S., Shim, J., Weaver, J.C., Chen, E.R., Pate, N. and Bertoldi, K, *3D Soft Metamaterials with Negative Poisson's Ratio.* Advanced Materials, 2013. **25**(36): p. 5044-5049.
4. Bertoldi, K., Boyce, M.C., Deschanel, S., Prange, S.M. and Mullin, T., *Mechanics of deformation-triggered pattern transformations and superelastic behavior in periodic elastomeric structures.* Journal of the Mechanics and Physics of Solids, 2008. **56**(8): p. 2642-2668.
5. Bertoldi, K., Reis, P.M., Willshaw, S. and Mullin, T., *Negative Poisson's Ratio Behavior Induced by an Elastic Instability.* Advanced Materials, 2010. **22**(3): p. 361-366.
6. Critchley, R., Corni, I., Wharton, J.A., Walsh, F.C.,; Wood, R.J.K and Stokes, K.R., *A review of the manufacture, mechanical properties and potential applications of auxetic foams.* physica status solidi (b), 2013. **250**(10): p. 1963-1982.
7. Shen, J., Zhou, S., Huang, X. and Xie, Y.M., *Simple cubic three-dimensional auxetic metamaterials.* physica status solidi (b), 2014. **251**(8): p. 1515-1522.
8. Cui, T.J., D. Smith, and R. Liu, *Metamaterials: Theory, Design, and Applications*. 2009: Springer Publishing Company, Incorporated. 368.
9. Veselago, V.G., *The electrodynamics of substances with simultaneously negative values of ε and μ.* {Phys. Usp., 1968. **10**(4): p. 504-514.
10. Wu, Y., Y. Lai, and Z.-Q. Zhang, *Elastic Metamaterials with Simultaneously Negative Effective Shear Modulus and Mass Density.* Physical Review Letters, 2011. **107**(10): p. 105506.
11. Pendry, J.B., *Negative Refraction Makes a Perfect Lens.* Physical Review Letters, 2000. **85**(18): p. 3966-3969.
12. Aguado, A., *Nanoparticles: Neither solid nor liquid.* Nat Mater, 2016. **15**(9): p. 931-933.
13. Attard, D., E. Manicaro, and J.N. Grima, *On rotating rigid parallelograms and their potential for exhibiting auxetic behaviour.* physica status solidi (b), 2009. **246**(9): p. 2033-2044.
14. Baughman R.H., Stafström S., Cui C. and Dantas S.O, *Materials with Negative Compressibilities in One or More Dimensions.* Science, 1998. **279**(5356): p. 1522-1524.
15. Cairns A.B.; Catafesta J.; Levelut C.; Rouquette J.; van der Lee A.; Peters L.; Thompson A.L.; Dmitriev V.; Haines J. and Goodwin A.L., *Giant negative linear compressibility in zinc dicyanoaurate.* Nat Mater, 2013. **12**(3): p. 212-216.
16. Critchley, R., Corni, I., Wharton, J.A., Walsh, F.C., Wood, R.J.K. and Stokes, K.R., *The Preparation of Auxetic Foams by Three-Dimensional Printing and Their Characteristics.* Advanced Engineering Materials, 2013. **15**(10): p. 980-985.
17. Evans, J.S.O., W.I.F. David, and A.W. Sleight, *Structural investigation of the negative-thermal-expansion material ZrW2O8.* Acta Crystallographica Section B, 1999. **55**(3): p. 333-340.
18. Friis, E.A., R.S. Lakes, and J.B. Park, *Negative Poisson' ratio polymeric and mettalic foams.* Journal of Materials Science, 1988. **23**(12): p. 4406-4414.
19. Goodwin, A.L., D.A. Keen, and M.G. Tucker, *Large negative linear compressibility of Ag3[Co(CN)6].* Proceedings of the National Academy of Sciences, 2008. **105**(48): p. 18708-18713.
20. Grima, J. and K. Evans, *Auxetic behavior from rotating triangles.* Journal of Materials Science, 2006. **41**(10): p. 3193-3196.
21. Grima, J.N., A. Alderson, and K.E. Evans, *Auxetic behaviour from rotating rigid units.* physica status solidi (b), 2005. **242**(3): p. 561-575.

22. Grima J.N., Attard D., Caruana-Gauci R. and Gatt R. *Negative linear compressibility of hexagonal honeycombs and related systems.* Scripta Materialia, 2011. **65**(7): p. 565-568.
23. Grima J.N.; Caruana-Gauci R.; Attard D. and Gatt R., *Three-dimensional cellular structures with negative Poisson's ratio and negative compressibility properties.* Proceedings of the Royal Society A: Mathematical, Physical and Engineering Science, 2012. **468**(2146): p. 3121-3138.
24. Grima, J.N. and K.E. Evans, *Auxetic behavior from rotating squares.* Journal of Materials Science Letters, 2000. **19**(17): p. 1563-1565.
25. Grima, J.N., Farrugia, P., Gat, R., Attard, D., *On the auxetic properties of rotating rhombi and parallelograms: A preliminary investigation.* physica status solidi (b), 2008. **245**(3): p. 521-529.
26. Grima, J.N., Gat, R. and Alderson, A., *On the potential of connected stars as auxetic systems.* Molecular Simulation, 2005. **31**(13): p. 925-935.
27. Grima, J.N., Gat, R., Raviralab, N., Aldersonb, A., Evansc, K.E., *Negative Poisson's ratios in cellular foam materials.* Materials Science and Engineering: A, 2006. **423**(1–2): p. 214-218.
28. Hodgson, S.A., Adamson, J., Hunt, S., Cliffe, M., Cairns, A., Thompson, A., Tucker, M. and Funnell, N., Goodwin, A., *Negative area compressibility in silver(i) tricyanomethanide.* Chemical Communications, 2014. **50**(40): p. 5264-5266.
29. LAKES, R., *Foam Structures with a Negative Poisson's Ratio.* Science, 1987. **235**(4792): p. 1038-1040.
30. Lakes, R., *Cellular solids with tunable positive or negative thermal expansion of unbounded magnitude.* Applied Physics Letters, 2007. **90**(22): p. 221905.
31. Lakes, R.S., Lee, T., Bersie, A. and Wang, Y.C., *Extreme damping in composite materials with negative-stiffness inclusionsa.* Nature, 2001. **410**(6828): p. 565-567.
32. Nicolaou, Z.G. and A.E. Motter, *Mechanical metamaterials with negative compressibility transitions.* Nat Mater, 2012. **11**(7): p. 608-613.
33. Ren, X., Shen, J., Ghaedizadeh, A., Tian, H. and Xie, Y., *A simple auxetic tubular structure with tuneable mechanical properties.* Smart Materials and Structures, 2016. **25**(6): p. 065012.
34. Schwerdtfeger, J., Heinl,P., Singer, R.F and Körner, C. , *Auxetic cellular structures through selective electron-beam melting.* physica status solidi (b), 2010. **247**(2): p. 269-272.
35. Steffens, F., S. Rana, and R. Fangueiro, *Development of novel auxetic textile structures using high performance fibres.* Materials & Design.
36. Theocaris, P.S., G.E. Stavroulakis, and P.D. Panagiotopoulos, *Negative Poisson's ratios in composites with star-shaped inclusions: a numerical homogenization approach.* Archive of Applied Mechanics, 1997. **67**(4): p. 274-286.
37. Ren, X., Shen, J., Ghaedizadeh, A., Tian, H. and Xie, Y., *Experiments and parametric studies on 3D metallic auxetic metamaterials with tuneable mechanical properties.* Smart Materials and Structures, 2015. **24**(9): p. 095016.
38. Florijn, B., C. Coulais, and M. van Hecke, *Programmable Mechanical Metamaterials.* Physical Review Letters, 2014. **113**(17): p. 175503.
39. Waitukaitis, S., Menaut, R., Chen, B.G. and Hecke, M., *Origami Multistability: From Single Vertices to Metasheets.* Physical Review Letters, 2015. **114**(5): p. 055503.
40. Silverberg, J.L., Evans, A., McLeod, L., Hayward, R., Hull, T., Santangelo, C.D., and Cochen, I., *Using origami design principles to fold reprogrammable mechanical metamaterials.* Science, 2014. **345**(6197): p. 647-650.
41. Jaglinski, T.M. and R.S. Lakes, *Negative Stiffness and Negative Poisson's Ratio in Materials which Undergo a Phase Transformation*, in *Adaptive Structures*. 2007, John Wiley & Sons, Ltd. p. 231-246.

42. Xie Y.M., Yang X., Shen J., Yan X., Ghaedizadeh A., Rong J., Huang X. and Zhou S. *Designing orthotropic materials for negative or zero compressibility.* International Journal of Solids and Structures, 2014. **51**(23–24): p. 4038-4051.
43. Gatt, R. and J.N. Grima, *Negative compressibility.* physica status solidi (RRL) – Rapid Research Letters, 2008. **2**(5): p. 236-238.
44. Kelly, A., R.J. Stearn, and L.N. McCartney, *Composite materials of controlled thermal expansion.* Composites Science and Technology, 2006. **66**(2): p. 154-159.
45. Grima, J.N., Ellula, B., Attarda, D., Gatta, R., Attard, M., *Composites with needle-like inclusions exhibiting negative thermal expansion: A preliminary investigation.* Composites Science and Technology, 2010. **70**(16): p. 2248-2252.
46. Evans, K.E. , *Molecular network design.* Nature, 1991. **353**(6340): p. 124-124.
47. Choi, J.B. and R.S. Lakes, *DESIGN OF A FASTENER BASED ON NEGATIVE POISSONS RATIO FOAM.* Cellular Polymers, 1991. **10**(3): p. 205-212.
48. Scarpa, F., *Auxetic materials for bioprostheses [In the Spotlight].* IEEE Signal Processing Magazine, 2008. **25**(5): p. 128-126.
49. Chen, C.P. and R.S. Lakes, *Micromechanical Analysis of Dynamic Behavior of Conventional and Negative Poisson's Ratio Foams.* Journal of Engineering Materials and Technology, 1996. **118**(3): p. 285-288.
50. Scarpa, F., L.G. Ciffo, and J.R. Yates, *Dynamic properties of high structural integrity auxetic open cell foam.* Smart Materials and Structures, 2004. **13**(1): p. 49.
51. Alderson, A., Rasburn, J., Ameer-Beg, S., Mullarkey, P.G., Perrie, W., and Evans, K., *An Auxetic Filter: A Tuneable Filter Displaying Enhanced Size Selectivity or Defouling Properties.* Industrial & Engineering Chemistry Research, 2000. **39**(3): p. 654-665.
52. Sun, Y. and N. Pugno, *Hierarchical Fibers with a Negative Poisson's Ratio for Tougher Composites.* Materials, 2013. **6**(2): p. 699.
53. Lakes, R. and K.W. Wojciechowski, *Negative compressibility, negative Poisson's ratio, and stability.* physica status solidi (b), 2008. **245**(3): p. 545-551.
54. Aliev A.E., Oh J., Kozlov M.E., Kuznetsov A.A., Fang S., Fonseca A.F., Ovalle R., and Lima M.D., Haque M.H.; Gartstein Y.N.; Zhang M.; Zakhidov A.A.; Baughman R.H. Giant-Stroke*, Superelastic Carbon Nanotube Aerogel Muscles.* Science, 2009. **323**(5921): p. 1575-1578.
55. Spinks G.M., Wallace G.G., Fifield L.S., Dalton L.R., Mazzoldi A., De Rossi D., Khayrullin II, and Baughman R.H., *Pneumatic Carbon Nanotube Actuators.* Advanced Materials, 2002. **14**(23): p. 1728-1732.
56. Schwerdtfeger, J., Wein, F., Leugering, G., Singer, R.F., Körner, C., Stingl, M. and Schury, F. *Design of Auxetic Structures via Mathematical Optimization.* Advanced Materials, 2011. **23**(22-23): p. 2650-2654.
57. Gibson, L.J., Ashby, M.F., Schajer, G.S. and Robertson, C.I., *The Mechanics of Two-Dimensional Cellular Materials.* Proceedings of the Royal Society of London. A. Mathematical and Physical Sciences, 1982. **382**(1782): p. 25-42.
58. Mullin, T., S. Willshaw, and F. Box, *Pattern switching in soft cellular solids under compression.* Soft Matter, 2013. **9**(20): p. 4951-4955.
59. Overvelde, J.T.B. and K. Bertoldi, *Relating pore shape to the non-linear response of periodic elastomeric structures.* Journal of the Mechanics and Physics of Solids, 2014. **64**: p. 351-366.
60. Friis, E.A., R.S. Lakes, and J.B. Park, *Negative Poisson's ratio polymeric and metallic foams.* Journal of Materials Science, 1988. **23**(12): p. 4406-4414.
61. Taylor, M., Francesconi, L., Gerendás, M., Shanian, A., Carson, C., and Bertoldi, K., *Low Porosity Metallic Periodic Structures with Negative Poisson's Ratio.* Advanced Materials, 2014. **26**(15): p. 2365-2370.

62. Dirrenberger, J., S. Forest, and D. Jeulin, *Elastoplasticity of auxetic materials.* Computational Materials Science, 2012. **64**: p. 57-61.

63. Andersson, A., Lundmark, S., Magnusson, A., Maurer, F.H., *Shear Behavior of Flexible Polyurethane Foams Under Uniaxial Compression.* Journal of Applied Polymer Science, 2009. **111**(5): p. 2290-2298.
64. Lakes, R., *Deformation mechanisms in negative Poisson's ratio materials: structural aspects.* Journal of Materials Science, 1991. **26**(9): p. 2287-2292.
65. Evans, K.E., M.A. Nkansah, and I.J. Hutchinson, *Auxetic foams: Modelling negative Poisson's ratios.* Acta Metallurgica et Materialia, 1994. **42**(4): p. 1289-1294.
66. N. Grima, J., A. Alderson, and K. E. Evans, *An Alternative Explanation for the Negative Poisson's Ratios in Auxetic Foams.* Journal of the Physical Society of Japan, 2005. **74**(4): p. 1341-1342.
67. Grima, J.N. and K.E. Evans, *Self expanding molecular networks.* Chemical Communications, 2000(16): p. 1531-1532.
68. Grima, J.N., Jackson, R., Alderson and A., Evans, K.E, *Do Zeolites Have Negative Poisson's Ratios?* Advanced Materials, 2000. **12**(24): p. 1912-1918.
69. Grima, J.N., Gat, R., Alserson, A. and Evans, K.E., *On the origin of auxetic behaviour in the silicate [small alpha]-cristobalite.* Journal of Materials Chemistry, 2005. **15**(37): p. 4003-4005.
70. Grima, J.N., Chetcuti, E., Manicaro, E., Attard, D., Camilleri, M., Gat, R. and Evans, K.E., *On the auxetic properties of generic rotating rigid triangles.* Proceedings of the Royal Society A: Mathematical, Physical and Engineering Science, 2012. **468**(2139): p. 810-830.
71. Prall, D. and R.S. Lakes, *Properties of a chiral honeycomb with a poisson's ratio of — 1.* International Journal of Mechanical Sciences, 1997. **39**(3): p. 305-314.
72. Vasiliev, A.A., et al., *Elastic properties of a two-dimensional model of crystals containing particles with rotational degrees of freedom.* Physical Review B, 2002. **65**(9): p. 094101.
73. Grima, J.N., et al., *Auxetic behaviour from rotating semi-rigid units.* physica status solidi (b), 2007. **244**(3): p. 866-882.
74. Attard, D., et al., *On the properties of auxetic rotating stretching squares.* physica status solidi (b), 2009. **246**(9): p. 2045-2054.
75. Grima, J.N., et al., *Auxetic behaviour from stretching connected squares.* Journal of Materials Science, 2008. **43**(17): p. 5962.
76. Bridgman, P.W., *The Compressibility of Metals at High Pressures.* Proceedings of the National Academy of Sciences of the United States of America, 1922. **8**(12): p. 361-365.
77. Mariathasan, J.W.E., L.W. Finger, and R.M. Hazen, *High-pressure behavior of LaNbO4.* Acta Crystallographica Section B, 1985. **41**(3): p. 179-184.
78. Cairns, A.B., et al., *Rational Design of Materials with Extreme Negative Compressibility: Selective Soft-Mode Frustration in KMn[Ag(CN)2]3.* Journal of the American Chemical Society, 2012. **134**(10): p. 4454-4456.
79. Wei, G. and S.F. Edwards, *Poisson ratio in composites of auxetics.* Physical Review E, 1998. **58**(5): p. 6173-6181.
80. Wei, G. and S.F. Edwards, *Auxeticity windows for composites.* Physica A: Statistical Mechanics and its Applications, 1998. **258**(1–2): p. 5-10.
81. Wei, G. and S.F. Edwards, *Effective elastic properties of composites of ellipsoids (I). Nearly spherical inclusions.* Physica A: Statistical Mechanics and its Applications, 1999. **264**(3–4): p. 388-403.
82. Christensen, R.M., *Effective properties for single size, rigid spherical inclusions in an elastic matrix.* Composites Part B: Engineering, 2004. **35**(6–8): p. 475-482.

83. Assidi, M. and J.-F. Ganghoffer, *Composites with auxetic inclusions showing both an auxetic behavior and enhancement of their mechanical properties.* Composite Structures, 2012. **94**(8): p. 2373-2382.
84. Strek, T. and H. Jopek, *Effective mechanical properties of concentric cylindrical composites with auxetic phase.* physica status solidi (b), 2012. **249**(7): p. 1359-1365.
85. Dyskin, A.V. and E. Pasternak, *Elastic composite with negative stiffness inclusions in antiplane strain.* International Journal of Engineering Science, 2012. **58**: p. 45-56.
86. *Index*, in *Structural Materials and Processes in Transportation*. 2013, Wiley-VCH Verlag GmbH & Co. KGaA. p. 567-578.
87. Gibson, L.J. and M.F. Ashby, *Cellular Solids: Structure and Properties*. 2 ed. 1997, Cambridge: Cambridge University Press.
88. Borchardt, L., et al., *Preparation and application of cellular and nanoporous carbides.* Chemical Society Reviews, 2012. **41**(15): p. 5053-5067.
89. Christensen, J., et al., *Vibrant times for mechanical metamaterials.* MRS Communications, 2015. **5**(3): p. 453-462.
90. Saxena, K.K., R. Das, and E.P. Calius, *Three Decades of Auxetics Research − Materials with Negative Poisson's Ratio: A Review.* Advanced Engineering Materials, 2016. **18**(11): p. 1847-1870.
91. Masters, I.G. and K.E. Evans, *Models for the elastic deformation of honeycombs.* Composite Structures, 1996. **35**(4): p. 403-422.
92. Evans, K.E., *The design of doubly curved sandwich panels with honeycomb cores.* Composite Structures, 1991. **17**(2): p. 95-111.
93. Smith, C.W., J.N. Grima, and K.E. Evans, *A novel mechanism for generating auxetic behaviour in reticulated foams: missing rib foam model.* Acta Materialia, 2000. **48**(17): p. 4349-4356.
94. Larsen, U.D., O. Signund, and S. Bouwsta, *Design and fabrication of compliant micromechanisms and structures with negative Poisson's ratio.* Journal of Microelectromechanical Systems, 1997. **6**(2): p. 99-106.
95. Larsen, U.D., O. Sigmund, and S. Bouwstra. *Design and fabrication of compliant micromechanisms and structures with negative Poisson's ratio*. in *Proceedings of Ninth International Workshop on Micro Electromechanical Systems*. 1996.
96. Ma, Z.D., *Three-dimensional auxetic structures and applications thereof*. 2011, Google Patents.
97. Stefan, H. and L. Andrés Díaz, *Direct laser writing of auxetic structures: present capabilities and challenges.* Smart Materials and Structures, 2014. **23**(8): p. 085033.
98. Shokri Rad, M., Y. Prawoto, and Z. Ahmad, *Analytical solution and finite element approach to the 3D re-entrant structures of auxetic materials.* Mechanics of Materials, 2014. **74**: p. 76-87.
99. Spadoni, A. and M. Ruzzene, *Elasto-static micropolar behavior of a chiral auxetic lattice.* Journal of the Mechanics and Physics of Solids, 2012. **60**(1): p. 156-171.
100. Dirrenberger, J., S. Forest, and D. Jeulin, *Effective elastic properties of auxetic microstructures: anisotropy and structural applications.* International Journal of Mechanics and Materials in Design, 2013. **9**(1): p. 21-33.
101. Ha, C.S., M.E. Plesha, and R.S. Lakes, *Chiral three-dimensional isotropic lattices with negative Poisson's ratio.* physica status solidi (b), 2016. **253**(7): p. 1243-1251.
102. N., G.J., *Negative Poisson's Ratios from Rotating Rectangles.* COMPUTATIONAL METHODS IN SCIENCE AND TECHNOLOGY 2004. **10**(2): p. 137-145.
103. Mullin, T., et al., *Pattern Transformation Triggered by Deformation.* Physical Review Letters, 2007. **99**(8): p. 084301.
104. Grima, J.N., et al., *Auxetic behaviour in non-crystalline materials having star or triangular shaped perforations.* Journal of Non-Crystalline Solids, 2010. **356**(37–40): p. 1980-1987.

105. Mizzi, L., et al., *Auxetic metamaterials exhibiting giant negative Poisson's ratios.* physica status solidi (RRL) – Rapid Research Letters, 2015. **9**(7): p. 425-430.
106. Grima, J.N., et al., *Auxetic Perforated Mechanical Metamaterials with Randomly Oriented Cuts.* Advanced Materials, 2016. **28**(2): p. 385-389.
107. Carta, G., M. Brun, and A. Baldi, *Design of a porous material with isotropic negative Poisson's ratio.* Mechanics of Materials, 2016. **97**: p. 67-75.
108. Ghaedizadeh, A., et al., *Tuning the Performance of Metallic Auxetic Metamaterials by Using Buckling and Plasticity.* Materials, 2016. **9**(1): p. 54.
109. Barnes, D.L., et al., *Modelling negative linear compressibility in tetragonal beam structures.* Mechanics of Materials, 2012. **46**: p. 123-128.
110. C.N. Weng, K.T. Wang, and T. Chen, *Design of Microstructures and Structures with Negative Linear Compressibility in Certain Directions.* Advanced Materials Research, 2008. **33-37**: p. 807-814.
111. Miller, W., K.E. Evans, and A. Marmier, *Negative linear compressibility in common materials.* Applied Physics Letters, 2015. **106**(23): p. 231903.
112. Fernandez, L., et al., *Temporary intravenous bag silo closure in severe abdominal trauma.* J Trauma, 1996. **40**(2): p. 258-60.
113. Keramati, M., et al., *The Wittmann Patch™ as a temporary abdominal closure device after decompressive celiotomy for abdominal compartment syndrome following burn.* Burns, 2008. **34**(4): p. 493-497.
114. Kushimoto, S., et al., *Usefulness of the bilateral anterior rectus abdominis sheath turnover flap method for early fascial closure in patients requiring open abdominal management.* World J Surg, 2007. **31**(1): p. 2-8; discussion 9-10.
115. Perez, D., et al., *Prospective evaluation of vacuum-assisted closure in abdominal compartment syndrome and severe abdominal sepsis.* J Am Coll Surg, 2007. **205**(4): p. 586-92.
116. Cheatham, M.L., et al., *Results from the International Conference of Experts on Intra-abdominal Hypertension and Abdominal Compartment Syndrome. II. Recommendations.* Intensive Care Med, 2007. **33**(6): p. 951-62.
117. Malbrain, M.L., et al., *Results from the International Conference of Experts on Intra-abdominal Hypertension and Abdominal Compartment Syndrome. I. Definitions.* Intensive Care Med, 2006. **32**(11): p. 1722-32.
118. Fitzgerald, J.E., et al., *Laparostomy management using the ABThera open abdomen negative pressure therapy system in a grade IV open abdomen secondary to acute pancreatitis.* Int Wound J, 2013. **10**(2): p. 138-44.
119. Barker, D.E., et al., *Vacuum pack technique of temporary abdominal closure: a 7-year experience with 112 patients.* J Trauma, 2000. **48**(2): p. 201-6; discussion 206-7.
120. Cuesta, M.A., et al., *Sequential abdominal reexploration with the zipper technique.* World J Surg, 1991. **15**(1): p. 74-80.
121. Doyon, A., et al., *A simple, inexpensive, life-saving way to perform iterative laparotomy in patients with severe intra-abdominal sepsis.* Colorectal Dis, 2001. **3**(2): p. 115-21.
122. Smith, P.C., J.S. Tweddell, and P.Q. Bessey, *Alternative approaches to abdominal wound closure in severely injured patients with massive visceral edema.* J Trauma, 1992. **32**(1): p. 16-20.
123. Suliburk, J.W., et al., *Vacuum-assisted wound closure achieves early fascial closure of open abdomens after severe trauma.* J Trauma, 2003. **55**(6): p. 1155-60; discussion 1160-1.
124. Tremblay, L.N., et al., *Skin only or silo closure in the critically ill patient with an open abdomen.* Am J Surg, 2001. **182**(6): p. 670-5.

125. Boele van Hensbroek, P., et al., *Temporary Closure of the Open Abdomen: A Systematic Review on Delayed Primary Fascial Closure in Patients with an Open Abdomen.* World Journal of Surgery, 2009. **33**(2): p. 199-207.

126. DAGGER, A., C.; FRY, Nicholas, Charlton; HICKS, John, Kenneth; HUDDLESTON, Elizabeth, Mary; PHILLIPS, Marcus, Damian; SAXBY, Carl; DUNN, Raymond M.;, *DEVICES AND METHODS FOR TREATING AND CLOSING WOUNDS WITH NEGATIVE PRESSURE*, W.I.P.O.-I. Bureau, Editor. 2013, SMITH & NEPHEW PLC: United Kingdom. p. 51.

127. DODD, J., Roderick;HAMMOND, Victoria, Jody;HARTWELL, Edward, Yerbury ; HICKS, John, Kenneth; HUDDLESTON, Elizabeth, Mary; SAXBY, Carl;, *APPARATUSES AND METHODS FOR WOUND THERAPY*

128. DUNN, R., M.;HARTWELL, Edward, Yerbury;HAMMOND, Victoria, Jody;HICKS, John, Kenneth;HUDDLESTON, Elizabeth, Mary;KELLY, Andrew;LINTON, Andrew;RICHARDSON, Mark;SAXBY, Carl;STERN, Tim;, *NEGATIVE PRESSURE WOUND CLOSURE DEVICE CROSS-REFERENCE TO RELATED APPLICATIONS*, W.I.P.O.-I. Bureau, Editor. 2014, SMITH & NEPHEW PLC: United Kingdom. p. 160.

129. DUNN, R., M.; HAMMOND, Victoria, Jody;HARTWELL, Edward, Yerbury; HICKS, John, Kenneth; HUDDLESTON, Elizabeth, Mary; KELLY, Andrew; LINTON, and M.S. Andrew;RICHARDSON, Carl; STERN, Tim;, *NEGATIVE PRESSURE WOUND CLOSURE DEVICE CROSS-REFERENCE TO RELATED APPLICATIONS*, W.I.P.O.-I. Bureau, Editor. 2014, SMITH & NEPHEW PLC: United Kingdom. p. 130.

130. HAMMOND, V., Jody; HARTWELL, Edward, Yerbury; HICKS, John, Kenneth; SAXBY, Carl, *WOUND CLOSURE DEVICE BACKGROUND OF THE DISCLOSURE*, W.I.P.O.-I. Bureau, Editor. 2014, SMITH & NEPHEW PLC: United Kingdom. p. 93.

131. Hanssen, A.G., Hopperstad, O.S., Langseth, M., and Ilstad, H., *Validation of constitutive models applicable to aluminium foams*. International journal of mechanic science, 2002. **44** (2): p. 359–406.

132. Shen, J., Xie, Y.M., Huang, X.D., Zhou, S.W. and Ruan, D., *Mechanical properties of luffa sponge*. Journal of the Mechanical Behavior of Biomedical Materials, 2012. **15**: p.141–152.

133. B. Florijn, C. Coulais, and M.V. Hecke, *Programmable Mechanical Metamaterials*. Physical Review Letters, 2014. **113**: p.175503.

134. Ishibashi, Y., and Iwata, M.A. Microscopic model of a negative Poisson's ratio in some crystals. *Journal of the Physical Society of Japan,* 2000. **69(8)**,p:2702–2703.

135. Lu, G. and T. Yu, *2 - Methodology of analysing energy-absorption capacities*, in *Energy Absorption of Structures and Materials*. 2003, Woodhead Publishing. p. 25-67.